

Magnetised Neutron Stars

Dissertation

der Mathematisch-Naturwissenschaftlichen Fakultät
der Eberhard Karls Universität Tübingen
zur Erlangung des Grades eines
Doktors der Naturwissenschaften
(Dr. rer. nat.)

vorgelegt von

Antonella Colaiuda

aus Rom

Tübingen

2010

Tag der mündlichen Prüfung: 08.02.2011

Dekan: Prof. Dr. Wolfgang Rosenstiel

1. Berichterstatter: Prof. Dr. Kostas Kokkotas

2. Berichterstatter: Prof. Dr. Valeria Ferrari

Abstract

In the last decades, great attention was devoted to the study of highly magnetised neutron stars. These compact objects are usually divided in Anomalous X-ray Pulsars (AXPs) and Soft Gamma Repeaters (SGRs). AXPs are characterised by a narrow spin period ($P \simeq 5 - 12$ secs) and high X-ray emission ($L \simeq 10^{36} - 10^{44}$ erg/s) while the SGRs, among other features, show huge peaks in their luminosity spectra, that could reach also $L \simeq 10^{46}$ erg/s. Such luminosity is associated with a huge release of energy that cannot be supported by rotational energy. It was then proposed that a huge magnetic field ($B > 10^{14}$ Gauss) could provide the appropriate reservoir of energy for these events. In fact, such a strong magnetic field could apply an intense magnetic pressure to the crust and eventually could break it. The breaking of the crust, followed by a readjustment of the magnetic field, could release the energy observed during the giant peaks of SGRs. In addition, such mechanism could also explain the soft tail observed some seconds after the giant flare. In this tail, a carefully analysis shows the presence of quasi periodical oscillations (QPOs), with frequencies going from few Hz to kHz. Here we proposed that the QPOs are Alfvén torsional oscillations, a type of oscillations generated and associate with the presence of a magnetic field.

In this thesis, we construct models of relativistic axisymmetric, non-rotating, magnetised neutron stars constituted of a fluid core and a thin solid crust. We derived the perturbation equations for these magnetar models and by using a linear evolution code, we study the various patterns of oscillations for different configurations and strengths of the magnetic field. We compare the frequencies found with the ones observed in the tail of the SGRs and we demonstrate that a magnetar model with specific solid crust and specific equation of state for the fluid core can explain all the observed frequencies. In this way we are able to constrain the parameters of the observed magnetars, such as the mass, the radius, the equation of state and the strength of the magnetic field.

Contents

1	Introduction	1
1.1	Neutron star structure	5
1.2	Magnetic field in neutron stars and magnetar progenitors	7
1.2.1	Association of magnetars with clusters and supernova remnants	9
1.3	Magnetar emission	10
1.3.1	The emission mechanism	11
1.4	Magnetic oscillations	14
1.5	Plan of this thesis and convention	16
2	Static magnetic equilibria	17
2.1	Equilibrium model of a non-magnetised star	17
2.2	Equilibrium model of a magnetised star	20
2.2.1	Fundamental equations in relativistic magnetohydrodynamics (MHD)	21
2.2.2	Structure of the potential vector and of the magnetic field	22
2.3	The source of the magnetic field	25
2.4	The Grad-Shavranov equation	28
2.4.1	Equation of state used	32
3	Magnetic oscillations equation	35
3.1	Perturbation equations	37
3.1.1	Crustal fields vs global fields	43
3.2	A new transformation of coordinates	45
3.2.1	Open and close magnetic field lines	48
4	Global torsional oscillations	51
4.1	Equation for the fluid star	52
4.1.1	Crank-Nicholson scheme	52
4.2	Numerical implementation	54
4.3	The effect of the toroidal field on the spectrum	58
4.4	Identification of the QPOs frequencies	60

5	Coupled crust-core magneto-oscillations	65
5.1	Model	67
5.2	Results	69
5.2.1	The continua	72
5.2.2	The crust frequencies	75
5.2.3	Discrete Alfvén modes	75
5.3	From discrete crustal modes to a continuum spectrum	76
5.4	Identification of the QPOs observed	81
5.4.1	Time intervals of the detected QPOs	82
6	Summary	85
	Acknowledgements	88
	Bibliography	89

1

Introduction

The hypothesis of the existence of very compact objects, with small radii and very high densities, was formulated first by Baade and Zwicky in 1934 [1]. The first pulsar was only observed accidentally many years later, in 1968 [2]. After a more consistent sample of observations, it was discovered that the rotational period of pulsars decreases very slowly but in a regular manner. The causes of this were unknown until Pacini [3], and later Gold [4] and Ostriker and Gunn [5], built a model where the pulsars are magnetized rotating neutron stars: the magnetic field on the surface (estimated $B_{\text{surf}} = 10^{11} - 10^{13}$ Gauss) is responsible for the observed spin-down. This model was successfully used to explain the observed spin-down of the Crab pulsar. The same model but with a lower magnetic field, $B_{\text{surf}} = 10^{11}$ Gauss, can explain the spin down of the millisecond pulsars.

In 1980, a neutron star with a really narrow period, $P \simeq 5 - 11$ seconds was discovered. Not long afterwards other stars with the same narrow period were detected. First, it was proposed that those stars could be accreting neutron stars, but the lack of observed companions made this hypothesis inconsistent. Then, it was argued that a very high surface magnetic field, $B_{\text{surf}} = 10^{14} - 10^{15}$ Gauss, could explain the observed period. The decay of such a strong magnetic field could also explain the detected X-ray luminosity of those objects. This new class of objects was called Anomalous X-ray Pulsars (AXPs).

It was only the discovery of the soft gamma repeaters (SGRs), that really validates the hypothesis of the existence of such high magnetic fields inside neutron

stars. The SGRs emit short bursts ($P < 1$ sec) with a luminosity $L \simeq 10^{41}$ erg/s in the X-ray/soft gamma ray range. For this reason, they were initially considered a subclass of the gamma ray bursts. However, the detection of giant peaks with a luminosity $L \simeq 10^{47}$ erg/s implied that SGRs could not be a sub class of gamma ray bursts, because no emission mechanism in gamma ray bursts can produce such high luminosity: new sources of energy would need to be found in order to explain the giant peak. Thompson and Duncan [6] proposed that a huge magnetic field, $B \simeq 10^{15}$ Gauss, could be the sources not only of the burst emission but also of the persistent one, observed during the quiescent period. It is also responsible for the fast spin down of those neutron stars.

How can the magnetic field be responsible of such emission? The mechanism could be really similar to the one present in magnetically active main sequence stars, where convective motion is the trigger of the magnetic field instability: such motion inside the convective zone can move the footpoints of the magnetic field on the stellar surface, creating tangential discontinuities. The created discontinuities imply that the magnetic field undergoes catastrophic reconnection, trying to achieve a new equilibrium configuration: the catastrophic magnetic reconnection could easily break the crust and trigger the flare. It must be noticed that in magnetars, the displacement of the footpoints is not caused by connective motions but instead by diffusive processes. In [6], Thompson and Duncan developed a toy model, where a circular displacement of the crust, caused by a readjustment of the magnetic field configuration, facilitates the breaking of the crust by the magnetic field. In addition, the interior magnetic field could twist with the exterior magnetic field, and raise the currents inside the magnetosphere or even drive new ones. This mechanism could be responsible for the quiescent X-ray emission observed in magnetars.

Thompson & Duncan also assumed that the huge magnetic field could not break the crust but instead just deform it plastically. High plasticity may be efficient at high temperatures, $T = 10^9$ K. This temperature can be reached in magnetar's crust due to magnetic heating. However, the magnetic stress overcomes the elastic stress for a magnetic field $B > B_{\text{cri}} = (4\pi\mu)^{1/2} = 4 \times 10^{15} \rho_{14}^{0.4}$ Gauss, where μ is the shear modulus and ρ_{14} is the mass-density expressed in terms of 10^{14} g/cm^3 (see [7]). This strength of magnetic field is usually reached, and sometimes also overtaken, in magnetars. When this happens, the magnetic pressure is so strong that it can eventually break the crust.

Another possible explanation of giant flares was formulated by Thompson, Lyutikov and Kulkarni (see [8]), who considered an instability of the magnetic field, and its consequent readjustment in the magnetosphere as the only trigger for the giant flare. In this case, energy from the interior is not required and,

consequently, the magnetic field inside the star does not play any role. However, in the same paper, the authors compare the observed outburst data with the data given by such a model and they found that the magnetosphere-instability model does not fit consistently the observed data, while a crust fracture is more efficient in fitting them.

Until now eight confirmed SGRs have been detected: among these, only three of them (SGR 0526-66 in 1978, SGR 1806-20 in 2004 and SGR 1900+14 in 1998) emitted a giant flare and only two, SGR 1806-20 and SGR 1900+14, show a periodicity in the soft tail that follows the giant flare.

The SGR 0526-66 was the first to be seen emitting a giant flare on the 5th of March 1979. At that time, no satellite was designed to measure such huge fluxes of photons, and nearly all of them saturated. However, by comparing the signals from the different satellites and by performing simulations of the emission and of its travel pattern in the Galaxy, it was shown that the emission constituted a hard impulse, lasting 0.2 sec, which was responsible of the saturation of the instruments, and by a modulation in soft X-rays that lasted several seconds. Furthermore, the SGR was found to be located near a supernova remnant in the Large Magellan Cloud. In addition, an 8 seconds modulation of the signal was measured by many detectors on Earth. This modulation seemed to suggest that the star was rotating with a period of about 8 seconds. Such period indicates that the stars rotates slowly compared to the other know neutron stars; which was the first hint in understanding the complete new nature of those objects.

The SGR 1806-20 was detected for the first time in January 1979, emitting moderate bursts. In the middle-1980's it was very active, frequently emitting large amount of bursts (more than 100). Since this time it was sporadically active and for many years was thought that, in the absence of bursts (i.e. in the so called quiescent period), the SGR did not emit any signal in any electromagnetic band. However, in the 1990's, many satellites observed quiescent X-ray activity from this source, showing clearly that, even in absence of bursts, the source is still a bright X-ray neutron star. The position of the star in the sky is contained in its name: 18 hours, 06 minutes ascension and -20 degrees declination. These coordinates correspond to the centre of the Galaxy, in a region quite populated by stars. For this reason for many years, it was thought that the SGR 1806-20 could have a companion, contradicting the hypothesis that stars with such high magnetic fields could not live in a binary system. This hypothesis, first confirmed from optical observations, was then discharged by more precise X-ray observations that made clear how no companions were present in the neighbour of the SGR. For this SGR, no sure association with supernovae remnants was found.

CHAPTER 1. INTRODUCTION

The SGR 1900+14 was located in the constellation Aquila: some recent observations show that the SGR is located near a young supernovae. The SGR 1900+14 was discovered in March 1979, however, it emitted a considerably smaller number of bursts than SGR 1806-20 (just three) and it was not active for a long period. On 27th August 1998, the SGR 1900+14 emitted a giant burst that was observed by three satellites: the Italian-German satellite Beppo-sax, the Russian experiment Konus, on board of a spacecraft orbiting around the Earth, and the Ulysse spacecraft, a joint experiment by ESA and NASA. Other satellites that did not point at the source during that time registered some traces of the event, because of the emission of a huge amount of energy. In fact, it was so strong that the outer layer of the Earth's atmosphere was ionized, causing some problems in the radio communications on Earth. The giant flare peak did not last long: after 10s its intensity was already an order of magnitude less than at the beginning. However, in the seconds after the giant peak, a tail was observed, lasting several seconds. After 380s, the activity of the SGR dropped again to normal. The analysis of the tail showed some quasi periodic oscillations (QPOs). The cause and explanation of these type of QPOs is the aim of this thesis .

All these characteristics make the magnetars really peculiar objects among the neutron stars. In particular, the huge magnetic field strength and the young age of these objects are quite different from those of normal neutron stars. This difference could be better understood looking at the $P - \dot{P}$ diagram, see Figure 1.1. In this diagram the period P and its derivative \dot{P} are used as axis coordinates, since for many neutron stars (included magnetars), it is possible to measure them quite accurately. In addition, the period and its derivative play an important role in estimating the magnetic field of a neutron star as well as its age. In fact, the magnetic field can be estimated, using the dipole radiation formula:

$$B = 3.2 \times 10^{19} (P\dot{P})^{1/2} Gauss \quad (1.1)$$

The value of the magnetic field is represented by continuous green lines in Figure 1.1 The dashed green line represents the characteristic age of neutron stars, as it is calculated from the formula:

$$\tau = \frac{P}{2\dot{P}} \quad (1.2)$$

Old neutron stars that are already slowed down by electromagnetic radiation are located manly in the bottom part of Figure 1.1, while the AXPs and the SGRs, indicated as red points, are located in the upper right corner of Figure 1.1. Their estimated age is about 10^4 yr and their magnetic field is stronger than 10^{14} G. A lower limit for the magnetic field of magnetars was estimated by Harley et al. [10] and by Kouvelitou et al. [11], who set this limit around $B = 4 \times 10^{14}$ G for

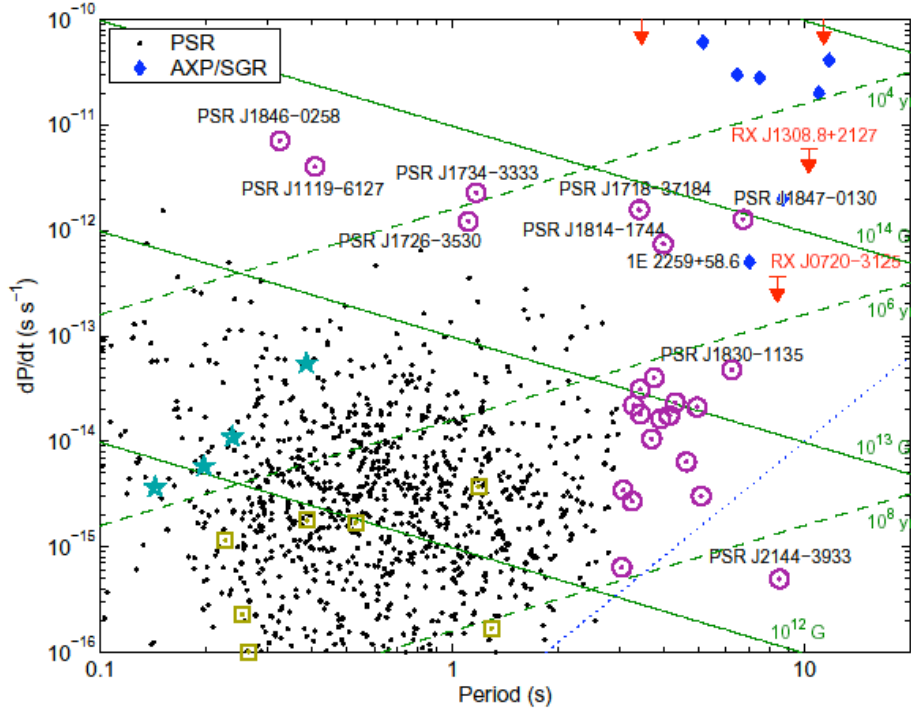


Figure 1.1: The $P - \dot{P}$ plot for neutron stars (Figure by McLaughlin et al. [9]).

SGR 1900+14 and $B = 8 \times 10^{14} \text{G}$ for SGR 1806-20. In a paper by Nagakawa et al [12], this limit was also higher. To be consistent with these estimates, we chose a magnetic field on the surface $B = 4 \times 10^{15} \text{G}$. In fact for higher values of the magnetic field, the crust is plastically deformed but not broken [13]. Without a breaking of the crust, is not possible to explain coherently all the observed features of the magnetars.

1.1 Neutron star structure

Although magnetars possess an extraordinary magnetic field, their interior structure is similar to other neutron stars. As is schematically drawn in Figure 1.2, a neutron star can be divided, with the following components:

core: the core constitutes up to 99% of the neutron star mass. The density is around $\rho \geq 2.6 \times 10^{14} \text{gcm}^{-3}$ and the matter is composed of neutron,

CHAPTER 1. INTRODUCTION

protons and electrons in β -equilibrium. The protons are just a 10% of the total mass, and the main contribution to the pressure comes from the neutrons, since they are more massive than electrons. Also, at such high densities, neutrons cannot be treated as a non-interactive particle gas: they can form a superfluid and the protons can form a superconductor. Exotic particles can also appear in the inner part of the core.

crust: the crust extends for about 1-2 km and is usually subdivided in outer and inner crust. The density goes from $\rho = 2 \times 10^{14} \text{ gcm}^{-3}$ (in the inner crust) to $\rho = 10^7 \text{ gcm}^{-3}$ (in the outer crust). In the inner crust the matter is composed of a mixture of two phases: one is rich in protons and one is a neutron gas. An electron gas is also present in order to preserve the charge neutrality. The dominant contribution to pressure is due to the neutron gas. At very high densities, at the interface between the crust and the core, the matter in the crust can form the so called ‘pasta’ phase, a status where nuclei display in different configurations (spheres, bar-type structures and slab-type structures). In the outer crust, a heavy nuclei lattice is immersed in an electron gas. In fact, the β -decay process is very effective at such densities, and, as a consequence, a large amount of neutrons are generated. As the pressure decreases, the β -decay process is not longer efficient and the neutrons are trapped in the nuclei. It is worth pointing out that while in ordinary neutron stars the crust is stable, in magnetars it is stressed by the huge magnetic pressure generated by the extraordinary high magnetic field.

envelope and atmosphere: they form a tiny layer, situated on the outer crust. They contain a negligible amount of mass, but they are really important for the radiative and transport properties of the star, influencing the thermal energy at the surface.

magnetosphere: the magnetosphere is created by charged particles, transported by electric currents. In fact, the strong electric field, generated by the magnetic field, is parallel to the stellar surface and rips off charged particle from the star, creating a dense magnetosphere. In magnetars, the magnetic field is strong enough to create long living currents in the magnetosphere, so that the latter is continuously filled with particles from the surface of the star. The magnetosphere could explain the non thermal persistent emission present in magnetar’s spectrum.

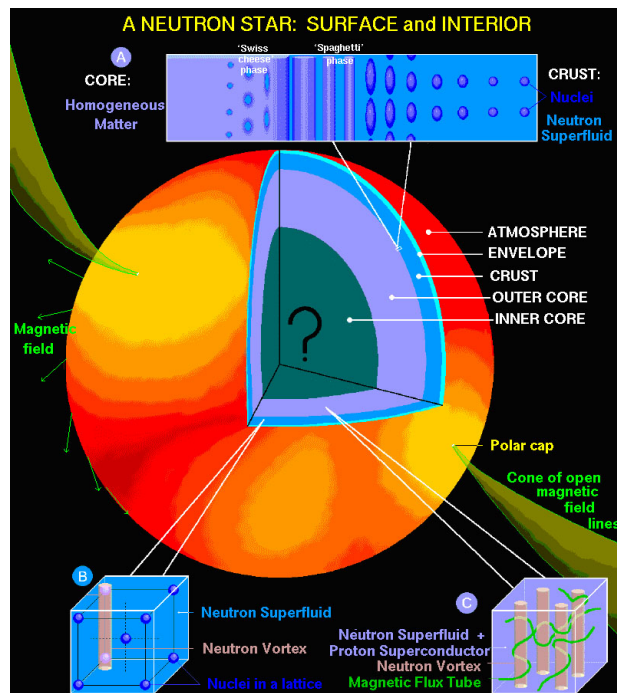


Figure 1.2: A schematic representation of neutron stars interior (Figure from Page & Reddy [14]).

1.2 Magnetic field in neutron stars and magnetar progenitors

The presence of a magnetic field in a neutron star is always an important issue, because its presence affects the internal and microscopic properties of the star: its period, its emission, its spin down, etc. However, it is not in neutron stars that the presence of magnetic field was first discovered, but instead on Earth.

The discovery that the Earth possesses magnetic fields goes back to the sixteenth century and it is attributed to William Gilbert. Not long after, Edmund Halley pictured the first world magnetic chart, although he was thinking of the Earth as permanently magnetized matter. When the variability of Earth's magnetic field was discovered, together with its dipole structure, it was inferred that the Earth's interior must be partially fluid in order to yield the observed magnetic variations. In 1909, the geophysicist Mohorovic noted that some characteristics of the seismometer's trace could be understood only if the Earth has a stratified structure. This was the first time seismic waves were used to study the internal

structure of an extended body. The first global shear modes in Earth were discovered after the earthquake in Chile in 1960. These modes were twisting the two hemispheres in opposite directions, involving no radial displacement.

The first study of extraterrestrial magnetism was made on the Sun by Hale, who proposed that the sunspots possess a magnetic field. The study was then continued, including the photosphere, solar prominences and filaments, and it was discovered that the magnetic field on the Sun changes every 11 years. Starting from 1940, the Zeeman effect was used to study the magnetic field on other stars. The magnetic field on a normal star is estimated to be around $B \simeq 10^3 - 10^4$ Gauss.

It is then natural to ask how such a weak magnetic field could generate the magnetic field that we actually measure on pulsars and magnetars. There are two competitive physical scenarios: the fossil-field scenario and the dynamo-scenario. The dynamo mechanism was investigated by Thompson and Duncan in [15]: in this scenario, in the first seconds of the magnetar's life, a rapid rotation, together with an effective convection, can create a favourable magnetic dynamo site, where an amplification of the magnetic field is not suppressed by turbulent diffusion. A magnetic field up to $B \simeq 10^{16}$ Gauss can be created, if the nascent neutron star is rotating very fast. The major objection to this theory is the present period measured in magnetars, between $P \simeq 2 - 12$ sec: that means that the magnetars are actually rotating too slowly to support this hypothesis. However, in the very first few moments of their life, magnetars are thought to be fast rotating, although no measurement can support this hypothesis. In the fossil field scenario, proposed in [16] and [17], the large magnetic field is a remnant of the one owned from the progenitor star, amplified during the collapse of this latter, that leads to the neutron star formation.

The progenitor of magnetars are thought to be O stars and early type B stars with surface magnetic field around $B = 10^3$ Gauss and mass $20M_{\odot} < M < 45M_{\odot}$. Ferrario and Wickramasinghe in [17] pointed out how a progenitor with a too low mass ($M < 18M_{\odot}$) would be in conflict with the birth rate of radio pulsars, that usually descend from star with $M < 18M_{\odot}$. On the other hand, a too large progenitor mass would produce a number of magnetars strongly below the present number of magnetars observed. Assuming a progenitor mass $M \simeq 20M_{\odot}$, the number of magnetars in our Galaxy is estimated to about 26. However, the observed number of magnetars in our Galaxy is 14. For this reason, the authors supposed that not all magnetars are actually active and so detectable from the satellites: some magnetars could also be in the quiescent state where no bursts or giant flare are present, making their detection extremely difficult. It is worth stressing that the study by Ferrario and Wickramasinghe in [17] assumes that all

the stars with mass $20M_{\odot} < M < 45M_{\odot}$ would produce a magnetar. With this assumption, the birth rate of magnetars in our Galaxy would be $3 \times 10^{-3} \text{ yr}^{-1}$. However, the number of magnetars in our Galaxy is about 14, so if no additional magnetar exists, this means that 50% of the stars with $20M_{\odot} < M < 45M_{\odot}$ could instead produce a black hole and the birth rate of magnetars is lowered to $1.5 \times 10^{-3} \text{ yr}^{-1}$.

The progenitors play an important role also in determining how the magnetic field distributes in the new born star as well as in the magnetic field strength. Heger et al. [18] proposed that the mass of the progenitor could somehow influence the spin of the nascent highly magnetised star. As we said before, if a star is fast rotating, then a dynamo process can occur leading to an amplification of the magnetic field. In addition, the shearing of a poloidal field of fossil origin together with a dynamo scenario may lead to the birth of a neutron star with both poloidal and toroidal strong magnetic field components. In fact the toroidal field could be produced by the twisting of the magnetic field line of a poloidal field. This twisting could be generated by the dynamo mechanism, due to the fast rotation of young and hot magnetars.

1.2.1 Association of magnetars with clusters and supernova remnants

As we discussed in the previous section, the origin of magnetars and of their strong magnetic field is still unclear. In particular, it is not well known how and where the progenitors of magnetars are formed. The most popular scenario involves the core-collapse of a massive star that generates a supernova. The supernova gives then birth to a neutron star. This scenario is supported by the observed association of supernova remnants to magnetars.

Sometimes, magnetars are associated with stellar clusters, in which case, it is possible to estimate the mass of the progenitor empirically using the cluster's lifetime. In fact, a measure of the age of the stellar cluster could help us to put some constraints not only on the time when the progenitor became supernovae but also on their mass. It is indeed known that the initial mass of a star is a strong function of the star's lifetime, so the initial mass can be estimated by knowing the stellar lifetime. For example, the SGR 1860-20, that was associated with stellar cluster C1 is estimated to have a progenitor with $M \gtrsim 40 M_{\odot}$, confirming the hypothesis that magnetars are born from massive stars. Such a hypothesis was confirmed by the observation of a supermassive star with $M \simeq 40 M_{\odot}$ that ended its life as a magnetar [19]. Also the SGR 1900+14 belongs to a cluster,

a hypothesis that was first made when the presence of an infrared ring around it was discovered. Spectroscopic observations confirmed that SGR 1900+14 is part of this cluster, estimated to be at a distance $D \simeq 12.5$ Kpc. The progenitor mass is estimated to be $M = 17 M_{\odot}$, sensitive lower than the progenitor's mass estimated for the other magnetars. Since it is almost impossible that a single star of such a mass could develop a rich-hydrogen envelope without involving a strong spin down of the star, it is not clear how a strong magnetic field can be created in lack of fast rotation. It was then supposed that in this case the magnetar was born by a binary system, so that the magnetar could be the product of a merger and the magnetic field could increase during the inspiral and the merger phase. This scenario could also explain the lack of counterpart optical/IR detection in the spectrum of SGR 1900-14.

1.3 Magnetar emission

To obtain a proper understanding of the magnetars emission, it is necessary to monitor the source for extensive periods of times and in different spectral electromagnetic bands. The SGR 1806-20 was monitored by the satellite *XMM-Newton* in the 1-10 KeV range in 2003-2004. It was then possible to study the long term evolution of this object, with particular attention to the persistent emission in X-ray at energies $10^{36} - 10^{39}$ erg/s. A model was suggested by Perna et al. [20] in order to explain the SGR spectrum. It consists of two components, a blackbody part and a power law one. The black body could explain the thermal emission of SGR, while the power law could explain the non-thermal emission. The power law could be produced by the cyclotron scattering of the X-rays in the magnetosphere with high-energy photons: such an effect was computed both analytically and by simulations. In this case, the thermal emission from the surface of the star is processed in the hot-plasma of the magnetosphere by multiple cyclotron scattering. Actually, this model could also explain the gamma rays observed during the quiescent emission of magnetars. A quiescent period is defined as a period where neither giant nor intermediate bursts are emitted from the source (see below). However, the detection of optical and infrared counterparts has emphasized that the multi-wavelength spectra is much more complex than a simple superposition of a black body and a power law.

Further monitoring of SGR 1806-20 and SGR 1900+14 were performed by the satellite *INTEGRAL* in the range 15keV-200keV, for hard gamma. Both sources show quiescent period in their life. It is also important to stress that the size of burst varies in SGRs, apart from the giant flares, also intermediate bursts

have been observed. Those latter last more than 500 seconds and release lower energy than the giant flares. They can also last from a few days up to a month. Some intermediate bursts were detected within a month from the giant flares: for this reason they are considered hints of the aftershocking, following the giant flares. On the other hand, they are also observed not in correlation with giant flares, suggesting that a continuum emission is coming from the SGRs.

Four observations of the SGR 1806-20 from the *XMM-Newton* satellite have been taken before the giant flare and show an increase of the activity of the source, in particularly of the flux, and a change in the spectrum shape, that shows a different structure after the giant flares. This increase and the change of the burst activity was attributed to a change in the magnetic field. As we explain in the next section, a magnetic field instability and its subsequent readjustment could explain these features and also the giant flare burst and the following soft tail. In this tail that lasts 200 sec quasi periodic oscillations have been found.

1.3.1 The emission mechanism

The paper by Thompson and Duncan [6] was the first attempt to explain coherently the emission of the SGRs as a consequence of the presence of a strong magnetic field $B > 10^{14}$ Gauss. They looked for a mechanism that could take into account the age of the magnetars, the lack of radio emission, the duration of the giant flare and the presence of the soft tail that follows the giant flare. They found that the presence of a strong magnetic field could successfully explain the SGRs emission mechanism. In addition, by developing a consistent model, they suggested an alternative strategy for searching for magnetars. Let's see in some more detail this model.

Magnetars are not detectable in the radio band due to the presence of a strong magnetic field. A star with a strong magnetic field spins down so effectively that it crosses the dead line of the pulsars quite early compared on the normal pulsars. This rapid evolution together with a relative small beaming radio makes detections in the radio band very difficult. However, the presence of a strong magnetic field offers new possible ways for detection. In fact, there is a characteristic age for which the energy of the magnetic field exceeds the rotational energy, which is estimated to be:

$$t_{\text{mag}} \simeq 400 \left(\frac{B_{\text{dipole}}}{B_{\text{QED}}} \right)^{-4} \text{ yr} \quad (1.3)$$

where $B_{\text{QED}} = m_e^2 c^3 / e \hbar = 4.4 \times 10^{13}$ Gauss is the magnetic field strength at which the non-relativistic Landau energy $\hbar e B / m_e c$ becomes equal to the electron

CHAPTER 1. INTRODUCTION

rest energy $m_e c^2$. The external magnetic dipole field is estimated to be around $B_{\text{dipole}} = 6 \times 10^{14}$ Gauss: the internal magnetic field could be also one order of magnitude greater. After this time, the rotational energy can not support the high luminosity observed in the giant flare. In fact, at the estimated magnetar age of 10^4 years, the maximum luminosity available from rotation is:

$$L_X \simeq \frac{1}{2t} I \left(\frac{2\pi}{P} \right)^2 \simeq 2 \times 10^{33} \text{ erg s}^{-1} \quad (1.4)$$

where I is the inertia moment of the star. Also, the X-ray emission that is detected is quiescent and is supported only by the decay of the magnetic field that lasts 10^4 years.

The most powerful phenomena in neutron stars are the giant flares, during which a luminosity $L > 10^{51}$ erg/s is reached. The giant flares could be explained by a catastrophic instability of the magnetic field due to hydromagnetic motions in the core. The consequent reconnection of the magnetic field at the base of the crust could break this latter and lead to the observed giant flare. The breaking of the crust also has an effect on the magnetic field lines. In fact, their footpoints are subjected to a torque, because of the displacement of the crust at which they are anchored. This torque produces a twist in the magnetic field lines that is schematically represented in Figure 1.3. The magnetic field reconnection takes place on a time scale of about $\simeq 0.1$ sec, that is comparable with the observed raise time of the giant flare. As consequence of the breaking of the crust, protons and electrons are ripped away from the surface and are injected in the magnetosphere. Here this plasma is trapped because of the optical thickness of the magnetosphere. In fact, the cross section of a photon is strongly suppressed in the presence of the strong magnetic field

$$\sigma = \frac{1}{\sin^2 \theta_{kB}} \left(\frac{\omega m_e}{eB} \right)^2 \sigma_T \quad (1.5)$$

where ω is the cyclotron frequency, σ_T is the Thompson cross section and θ_{kB} is the angle between the photon's wave vector and the magnetic field. Because of the suppressed cross section, the photons and the electrons pairs cannot leave the magnetosphere and trapped plasma is formed.

This trapped plasma (also called 'trapped fireball') is left behind when the outflow from the surface of the star ceases. This optically thick photon-pair plasma is trapped by the closed magnetic lines within a distance of 10km from the star. Then, the fireball starts to cool down: the velocity of the cooling down is limited by the transparency of its external layers. In fact, a sharp temperature gradient is created on the external layer of the fireball, generating cooling waves

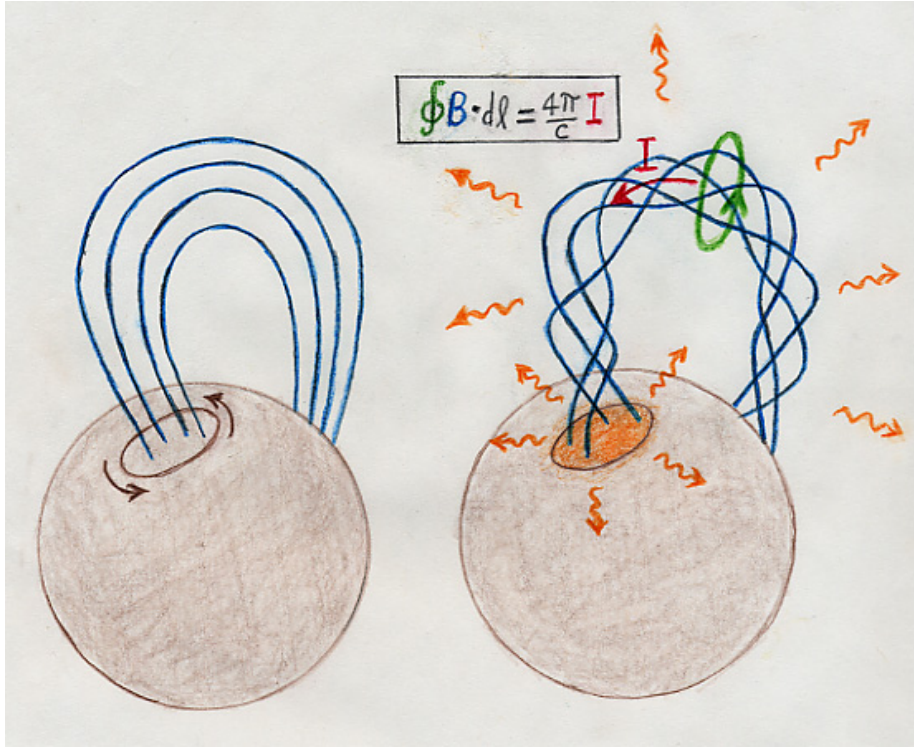


Figure 1.3: A schematic view of the crust displacement and of the magnetic field twisting (courtesy of Robert Duncan)

that propagate from the exterior of the fireball till to the internal hot region, cooling it effectively down. The luminosity of the fireball (about $L \simeq 10^{41}$ erg/s) and the cooling time of the fireball (around few hundreds seconds) are compatible with the ones of the soft tail detected in SGRs. In addition, the fireball contracts and expands during its cooling because of the scattering processes that take place inside the fireball between electron pairs and photons. These oscillations could be identified with QPOs in the soft tail of SGRs. However, this model doesn't fit the present observed QPOs: at the contrary in this thesis we will show that torsional oscillations modes in a star composed of a fluid core and a solid crust can explain the observed QPOs.

Apart from the giant flares, small bursts have been detected in all three SGRs. They are thought to be caused by small fractures of the crust that follow the major one. In this case no reconnection is present. The small fracture of the

crust could happen only when the magnetic energy is stronger than the tensile energy, caused from the plastic deformation of the crust. This happens for $B < 6 \times 10^{15}$ Gauss.

1.4 Magnetic oscillations

Two of the three giant flares that have been detected until now (SGR 1900+14 in 1998, and SGR 1806-20 in 2004) show a decay tail that accompanies the giant flare. The timing analysis of the latter two events revealed several QPOs in the decaying tail, whose frequencies are approximately 18, 26, 30, 92, 150, 625, and 1840 Hz for SGR 1806-20 (see Figure 1.4), and 28, 53, 84, and 155 Hz for SGR 1900+14, see [21]. It is believed, that during an SGR event, torsional oscillations in the solid crust of the star could be excited [22], leading to the observed frequencies in the X-ray tail. Actually, the frequency of many of these oscillations fits to the values of the torsional mode oscillations of the solid crust of a compact star, see [23], [24]. However, since not all of the observed frequencies could be explained by pure crust oscillations ([24] and [23]) alternative scenarios have also been suggested. For example, Glampedakis et al. [25] claimed that the observed spectra may explained via global magneto-elatic oscillations (see also [26] for more recent discussion) while Levin in [27] pointed out that the Alfvén oscillations of magnetars could be a continua. Recently, a toy model calculation by Levin [28] indicated that the edges or turning point of the continua could correspond to long-lived QPOs. Following Levin's suggestion, Sotani et al. [29] construct a numerical code for more realistic magnetar configurations and confirmed the Alfvén oscillations of magnetars could be a continua which could explain the lower observed frequencies. In a more recent paper by Sotani & Kokkotas [30] it was shown that the spectrum of the polar Alfvén oscillations is actually discrete. Their results are confirmed by recent work by Lander & Jones [31], where the authors study polar oscillations in the presence of a poloidal field.

Sotani et al. [29] performed two-dimensional numerical simulations of linearized Alfvén oscillations in magnetars. Their model improves the previously considered toy models in various ways. General relativity is assumed, various realistic equations of state (EOS) were considered and a consistent dipolar magnetic field is constructed. However, it does not take into account the presence of a solid crust and only examines the response of the ideal magnetofluid to a chosen initial perturbation. The two-dimensional partial differential equation (PDE) that they used to study the Alfvén oscillations has a mathematical pathological behavior,

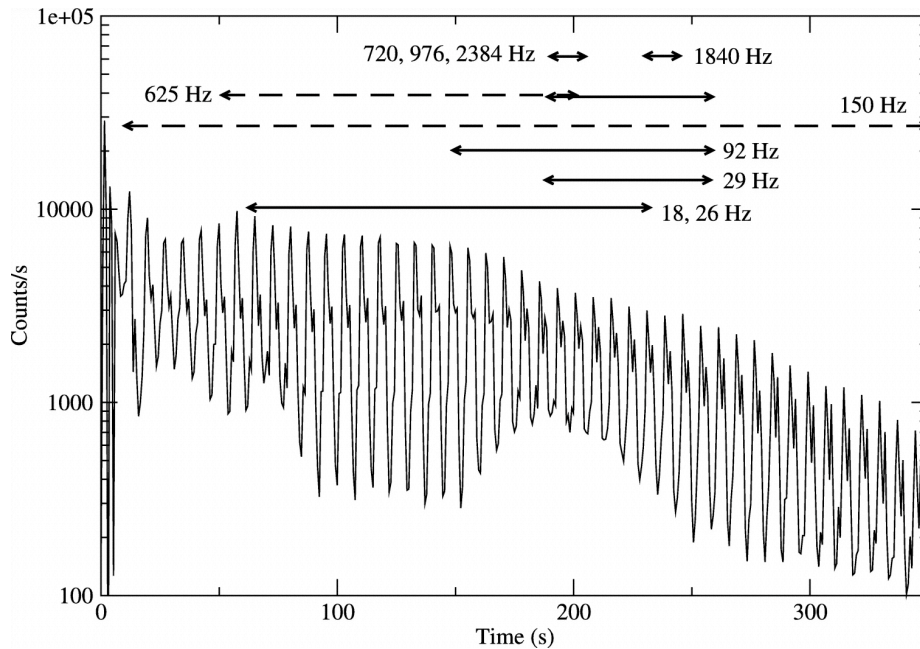


Figure 1.4: The observed QPOs tail in SGR 1806-20 (from Strohmayer and Watts [21])

as will be explained in chapter 3, and forced them to introduce artificial numerical viscosity in an attempt to stabilize the numerical evolution. The numerical results presented in [29] are compatible with the observations, as for example, they found two families of QPOs corresponding to the edges or turning points of a continua with harmonics at near integer multiples. With this identification, they could set an upper limit to the dipole magnetic field of ~ 3 to 7×10^{15} G and they could limit the models to very stiff EOSs for values of the magnetic field strength near to its upper limit, or moderately stiff for lower values of the magnetic field.

In an extension of that paper [32], we have studied the axisymmetric crust torsional modes of magnetars with poloidal and toroidal magnetic fields, where both components are confined in the crust. We present these results in Chapter 4. The numerical results showed that this magnetic configuration cannot explain the actual observational data of SGRs and it is in agreement with a more recent result by Van Hoven & Levin [33].

Some recent works by Gabler et al. [34] and by Van Hoven & Levin [35] take into account the presence of an elastic crust, using different techniques.

While Gabler et al. develop a non-linear code, Van Hoven & Levin use a toy-model. The two works find different results: Van Hoven & Levin find Alfvén continua accompanied by some discrete modes near the edges of the continua, while Gabler et al. find no discrete modes for magnetic field $B > 10^{14}$ Gauss. In both the papers, no identification of observed QPOs was made.

In this thesis, we will present the results of our study of the QPOs oscillations for two types of magnetars configurations: a star composed only of a fluid and a star with fluid core and solid crust. In our study we have used a new transformation of coordinates that simplifies the numerical study and allows us to give a phenomenological interpretation of our results. We will show that our model could consistently explain all the observed data.

1.5 Plan of this thesis and convention

In chapter two we will shortly review the equilibrium configuration of a neutron star in the absence of a magnetic field. We will then add a magnetic field and derive the Grad-Shafranov equation, i.e. the equation that describes the equilibrium configuration of the magnetic field in the star, including both a poloidal and a toroidal component. In chapter three we will perturb the equilibrium configuration in order to derive the equation that describe the torsional oscillations in a neutron stars. In chapter four, we study the torsional oscillations for a star composed exclusively from a perfect fluid. In chapter five, we add a solid crust to the previous configuration and show how a stellar model with fluid core and solid crust could explain all the observed frequencies in SGRs. In the last chapter, we will present and discuss the results obtained in this thesis.

In this thesis, we will use the following conventions:

- the signature of the metric is $-, +, +, +$, i.e. the time like vectors have negative norm,
- we use units where $G = c = 1$,
- we use the summation convention of Einstein. Latin indices indicate spatial components and run from 1 to 3 (unless otherwise states) and the Greek indices indicate spacetime components and run from 0 to 3 (the 0-th component is the temporal component),
- the covariant derivative of an arbitrary quantity, u , with respect to the coordinate, x^μ , are written as $D_\mu u$ or $u_{;\mu}$, while partial derivatives are denoted with $\partial_\mu u$ or $u_{,\mu}$.

2

Static magnetic equilibria

In this chapter, we derive the equations describing a spherically, symmetric, non-rotating, magnetised neutron star. The derivation consists of two steps:

- firstly, we derive the equilibrium model that is spherically, symmetric, non rotating neutron star, by solving the Tolmann Oppenheimer-Volkoff equations (TOV equations),
- then, we review the Maxwell equations in general relativity and derive the Grad-Shafranov equation for a mixed poloidal-toroidal field. This equation describes the distribution of the magnetic field inside the star.

We will use this type of equilibrium models as the background on which small perturbations are evolving. In this way, in the following chapters, we will address the problem of quasi periodic oscillations in magnetars.

2.1 Equilibrium model of a non-magnetised star

In this section we will derive the Tolmann Oppenheimer-Volkoff equations (TOV equations, see [36]). The solutions of these equations for a given central density and a given equation of state describe uniquely the internal structure of a spherically symmetric, non-rotating relativistic star without magnetic field. In the exterior, this solution describe a spherically symmetric spacetime.

The line element that describes a static and spherically symmetric spacetime without the presence of a magnetic field has the form:

$$ds^2 = -e^{-2\Phi} dt^2 + e^{2\Lambda} dr^2 + r^2(d\theta^2 + \sin^2 \theta d\phi^2) = g_{\mu\nu} dx^\mu dx^\nu. \quad (2.1)$$

CHAPTER 2. STATIC MAGNETIC EQUILIBRIA

The TOV equations can be derived by using the metric (2.1) and the Einstein equations:

$$G_{\mu\nu} = 8\pi T_{\mu\nu} \quad (2.2)$$

together with the conservation law of the energy tensor:

$$T^{\mu\nu}_{;\nu} = \frac{1}{\sqrt{g}} \frac{\partial}{\partial x^\nu} (-\sqrt{-g} T^{\mu\nu}) + \Gamma_{\alpha\nu}^{\mu} T^{\alpha\nu} = 0 \quad (2.3)$$

where g is the determinant of the metric $g_{\mu\nu}$ and $T^{\mu\nu}$ is the energy-momentum tensor, that, with the assumption that the star is composed by a perfect fluid, has the form:

$$T^{\mu\nu} = (P + \rho)u^\mu u^\nu + P g^{\mu\nu}. \quad (2.4)$$

In the equation (2.4) P, ρ and u^μ are, respectively, the pressure, the density and the four-velocity of the star. Because the fluid is at rest in the background metric, the four velocity has only one non-zero component. The u^t component can be derived from:

$$g_{\mu\nu} u^\mu u^\nu = -1 \rightarrow u^t = e^{-\Phi} \text{ or } u_t = -e^{\Phi}. \quad (2.5)$$

We consider first the equation (2.3). The only not trivial component is the one with $\mu = r$:

$$\frac{1}{\sqrt{-g}} \frac{\partial}{\partial x^\nu} (\sqrt{-g} T^{r\nu}) + \Gamma_{\nu\lambda}^r T^{\nu\lambda} = 0 \quad (2.6)$$

where $\Gamma_{\nu\mu}^\alpha$ are the Christoffel symbols given by:

$$\Gamma_{\mu\nu}^\alpha = \frac{1}{2} g^{\alpha\sigma} (g_{\mu\sigma,\nu} + g_{\nu\sigma,\mu} - g_{\mu\nu,\sigma}). \quad (2.7)$$

Substituting equation (2.4) and (2.7) in equation (2.6), we get the relativistic version of the equation for hydrostatic equilibrium:

$$\frac{\partial\Phi}{\partial r} = -\frac{1}{\rho + P} \frac{\partial P}{\partial r}. \quad (2.8)$$

Now we can examine the Einstein equations (2.2). Because of the form of the metric (2.1) and the energy-momentum tensor $T^{\mu\nu}$ (see equation (2.4)), the only non-zero Einstein equation are:

$$\begin{aligned} a) \quad G_{tt} &= 8\pi T_{tt} \\ b) \quad G_{rr} &= 8\pi T_{rr} \\ c) \quad G_{\theta\theta} &= 8\pi T_{\theta\theta}. \end{aligned} \quad (2.9)$$

The first member of the equations (2.9) is given by:

$$G_{\mu\nu} = R_{\mu\nu} - \frac{1}{2}g_{\mu\nu}R \quad (2.10)$$

where $R_{\mu\nu}$ and R are respectively the Ricci tensor and the Ricci scalar given by:

$$R_{\mu\nu} = R_{\mu\gamma\nu}^{\gamma} = \Gamma_{\mu\nu,\gamma}^{\gamma} - \Gamma_{\mu\gamma,\nu}^{\gamma} + \Gamma_{\mu\nu}^{\gamma}\Gamma_{\alpha\gamma}^{\alpha} - \Gamma_{\alpha\mu}^{\gamma}\Gamma_{\nu\gamma}^{\alpha} \quad (2.11)$$

$$R = R_{\mu}^{\mu} = g^{\mu\alpha}R_{\alpha\mu}. \quad (2.12)$$

After some calculations, the equations (2.9) become:

$$\frac{d}{dr}[r(1 - e^{-2\Lambda})] = 8\pi\rho r^2 \quad (2.13)$$

$$-(1 - e^{-2\Lambda}) + r\Phi_{,r}e^{-2\Lambda} = 8\pi Pr^2 \quad (2.14)$$

$$r^2(2\Phi_{,rr} + \Phi_{,r}^2 + 2\frac{\Phi_{,r}}{r} - \Phi_{,r}\Lambda_{,r} - 2\Lambda_{,r}) = 16\pi r^2 P e^{2\Lambda}. \quad (2.15)$$

Setting:

$$m(r) = \frac{1}{2}r(1 - e^{-2\Lambda}) \rightarrow e^{-2\Lambda} = 1 - \frac{2m(r)}{r} \quad (2.16)$$

the equation (2.13a) becomes:

$$\frac{dm(r)}{dr} = 4\pi r^2 \rho \quad (2.17)$$

that is the first TOV equation: it describes the mass distribution in the star. Using equation (2.16) and (2.13b) we get:

$$\frac{d\Phi(r)}{dr} = \frac{m(r) + 4\pi r^3 P(r)}{r(r - 2m(r))}. \quad (2.18)$$

Finally, by substituting t equation (2.8) into equation (2.18), we get the second TOV equation:

$$\frac{dP(r)}{dr} = -\frac{[\rho(r) + P(r)][m(r) + 4\pi r^3 P(r)]}{r[r - 2m(r)]}. \quad (2.19)$$

Outside the star, for $r > R$, the metric reduced to the Schwarzschild metric: the solutions for the functions Φ and Λ are then:

$$e^{2\Phi} = e^{-2\Lambda} = 1 - \frac{2M}{r} \quad (r \geq R) \quad (2.20)$$

where M is the total mass of the star in geometrical units (M is a constant).

In order to integrate the two TOV equations (2.17) and (2.19), we need:

- an equation of state (EOS) that links density and pressure so that:

$$P = P(\rho) \quad (2.21)$$

- to assign the initial conditions (i.e. the central density),
- and to demand that, on the stellar surface ($r = R$) the metric (2.1) must be smoothly with the Schwarzschild metric.

With those requests, we can solve the TOV equations and obtain the radius and the mass of the background stars, as well as its profiles of pressure and density.

2.2 Equilibrium model of a magnetised star

In this section we will review the Maxwell equations following the formalism used in [37]. We will then derive the form of the magnetic field, including both a poloidal and a toroidal component, and we will explain what is the source of both its poloidal and toroidal part.

In the following, we assume that the magnetic field of the star is:

- axisymmetric,
- created by a stationary current J_μ
- owns both a poloidal and a toroidal component.

A magnetic field B^μ is defined:

poloidal if its spatial components B^i (with $i = 1, 2, 3$) are in the meridional plane defined by the coordinate x^a (with $a = r, \theta$), i.e. if the magnetic field has components along the r and θ coordinate :

$$B^i = (B^r, B^\theta, 0); \quad (2.22)$$

toroidal if its spatial components are parallel to the vector $\xi = \partial/\partial\phi$, i.e. if the magnetic field has a component along ϕ

$$B^i = (0, 0, B^\phi). \quad (2.23)$$

As a consequence a magnetic field, with both a poloidal and a toroidal component, has the following form:

$$B^i = (B^a, B^\phi) \quad (x^a = r, \theta). \quad (2.24)$$

2.2.1 Fundamental equations in relativistic magnetohydrodynamics (MHD)

In a stationary and axisymmetric space time, it is always possible to define two Killing vectors $\eta = \partial/\partial t$ and $\xi = \partial/\partial\phi$. As a consequence, all the stationary and axisymmetric quantities will not depend on the time and on the azimuthal coordinate ϕ but only on the radial and angular coordinate $x^a = r, \theta$ with $a = 1, 2$ (hereafter with the index a we will refer to the radial and angular coordinate) .

The magnetic field is governed by the Maxwell equations:

$$F_{[\mu\nu; \alpha]} = 0 \quad (2.25)$$

$$F^{\mu\nu}_{; \nu} = 4\pi J^\mu \quad (2.26)$$

where $F_{\mu\nu}$ and J^μ are respectively the electromagnetic tensor and the four-current. The equation (2.25) implies the existence of a potential vector A_μ so that :

$$F_{\mu\nu} = \partial_\mu A_\nu - \partial_\nu A_\mu. \quad (2.27)$$

It is obvious that by construction the tensor $F_{\mu\nu}$ is antisymmetric. Because of the antisymmetry, equation (2.25) can be reduced to:

$$F_{[\mu\nu, \alpha]} = 0 \quad (2.28)$$

since the Christoffel's symbols $\Gamma_{\mu\nu}^\alpha$ are symmetric in the indices μ, ν and so they cancel out in the expression for the covariant derivative. Moreover, due to the existence of the Killing vectors, the potential vector A_μ is a function only of the x^a coordinate:

$$A_\mu = A_\mu(x^a), \quad x^a = r, \theta. \quad (2.29)$$

From the equation (2.27) and the dependence of A_μ only on r and θ , we get:

$$F_{t\phi} = \partial_\phi A_t - \partial_t A_\phi = -F_{\phi t} = 0. \quad (2.30)$$

In the reference system moving with the fluid, the electric and the magnetic field are given, as functions of the electromagnetic tensor by:

$$E_\mu = F_{\mu\nu} u^\nu \quad (2.31)$$

$$B_\mu = -\frac{1}{2} \epsilon_{\mu\nu\alpha\beta} u^\nu F^{\alpha\beta} \quad (2.32)$$

where $\epsilon_{\mu\nu\alpha\beta} = (-g)^{1/2} \epsilon_{[\mu\nu\alpha\beta]}$ (with $\epsilon_{[0123]} = 1$) is the Levi-Civita antisymmetric tensor. Inverting the equations (2.31) and (2.32), we can rewrite $F_{\mu\nu}$ as:

$$F_{\mu\nu} = u_\mu E_\nu - u_\nu E_\mu + \epsilon_{\mu\nu\alpha\beta} u^\alpha B^\beta. \quad (2.33)$$

We can further simplify the equation (2.33), by making the assumption, that the star has infinity conductivity, i.e. the electric field E^μ is null:

$$E_\mu = F_{\mu\nu}u^\nu = 0 \quad (2.34)$$

and as consequence:

$$E_\mu u^\mu = 0 \quad (2.35)$$

$$B_\mu u^\mu = 0 \quad (2.36)$$

as we can see from the equations (2.31) and (2.32) because of the antisymmetry of $F_{\mu\nu}$.

2.2.2 Structure of the potential vector and of the magnetic field

The temporal component of the potential vector A_μ is null because the star is not rotating, while the spatial components are all functions of the coordinates x^a :

$$A_\mu(x^a) = (0, A_r, A_\theta, \psi) \quad (2.37)$$

where $\psi = \mathbf{A}_\phi$ and, in literature, is called **magnetic flux**.

It is possible to find an explicit expression of the potential vector A_μ , considering an auxiliary function Λ such that:

$$\Lambda_{,\theta} = A_\theta. \quad (2.38)$$

Performing a gauge transformation, we get:

$$A_\mu \rightarrow A_\mu - \partial_\mu \Lambda = (0, A_r - \Lambda_{,r}, 0, \psi). \quad (2.39)$$

In such a way, we eliminate the component along θ of A_μ . We can further compact the expression (2.39) for A_μ , by defining a function $\Sigma(r, \theta)$ such as:

$$\Sigma(r, \theta) = e^{\Phi - \Lambda}(A_r - \Lambda_{,r}). \quad (2.40)$$

Substituting the expression for Σ in the equation (2.39), this latter gives :

$$A_\mu = (0, e^{\Phi - \Lambda}\Sigma, 0, \psi). \quad (2.41)$$

In order to simplify the expression (2.41), we need to use the Lorentz force, defined as:

$$f_\nu \equiv F_{\mu\nu}J^\mu \quad (2.42)$$

where J^μ is the four-current, defined as:

$$J_\mu = \frac{1}{4\pi\sqrt{-g}}(\sqrt{-g}F_\mu^\nu)_{,\nu}. \quad (2.43)$$

The Lorentz force is present also in the Euler equation that describes the motion of the fluid in the star. In fact, the Euler equation is given by:

$$(P + \rho)a_\mu + P_{,\mu} + u_\mu u^\nu P_{,\nu} - f_\mu = 0 \quad (2.44)$$

where a_μ is the acceleration of the fluid, defined as:

$$a_\mu = u^\nu u_{\mu;\nu} \quad (2.45)$$

where u_μ is the four-velocity of the fluid. If we calculate the ϕ component of the Lorentz force from the equation (2.44), we find that f_ϕ is equal to zero, because u_ϕ is equal to zero, this leads to the conclusion that the pressure P is function inly of the radius. Then we can set:

$$f_\phi = F_{\phi\nu} J^\nu = (A_{\nu,\phi} - A_{\phi,\nu}) J^\nu = -A_{\phi,\nu} J^\nu = -A_{\phi,r} J^r - A_{\phi,\theta} J^\theta = 0. \quad (2.46)$$

From the equation (2.43), we obtain the componets J^a of the four-current:

$$\begin{aligned} J^r &= \frac{1}{4\pi\sqrt{-g}}(\sqrt{-g}F^{rb})_{,b} = \frac{1}{4\pi\sqrt{-g}}(\sqrt{-g}F^{r\theta})_{,\theta} = \\ &= -\frac{1}{4\pi\sqrt{-g}}(\sqrt{-g}g^{rr}g^{\theta\theta}A_{r,\theta})_{,\theta} \end{aligned} \quad (2.47)$$

$$\begin{aligned} J^\theta &= \frac{1}{4\pi\sqrt{-g}}(\sqrt{-g}F^{\theta b})_{,b} = \frac{1}{4\pi\sqrt{-g}}(\sqrt{-g}F^{\theta r})_{,r} = \\ &= \frac{1}{4\pi\sqrt{-g}}(\sqrt{-g}g^{rr}g^{\theta\theta}A_{r,\theta})_{,r} \end{aligned} \quad (2.48)$$

where we have considered that $A_\theta = 0$ and $A_\mu = A_\mu(x^a)$. Using the expression for the potential vector A_μ given in (2.41), we get:

$$\begin{aligned} J^r &= -\frac{1}{4\pi\sqrt{-g}}(\sqrt{-g}g^{rr}g^{\theta\theta}A_{r,\theta})_{,\theta} = \\ &= -\frac{1}{4\pi\sqrt{-g}}(e^{\Phi-\Lambda}\sin\theta A_{r,\theta})_{,\theta} = -\frac{1}{4\pi\sqrt{-g}}(e^{\Phi-\Lambda}\sin\theta e^{\Lambda-\Phi}\Sigma_{,\theta})_{,\theta} = \\ &= -\frac{1}{4\pi\sqrt{-g}}(\cos\theta\Sigma_{,\theta} + \sin\theta\Sigma_{,\theta\theta}) = -\frac{1}{4\pi r^2}(\cot\theta\Sigma_{,\theta} + \Sigma_{,\theta\theta})e^{\Phi-\Lambda} \end{aligned} \quad (2.49)$$

$$\begin{aligned} J^\theta &= \frac{1}{4\pi\sqrt{-g}}(\sqrt{-g}g^{rr}g^{\theta\theta}A_{r,\theta})_{,r} = \\ &= \frac{1}{4\pi\sqrt{-g}}(e^{\Phi-\Lambda}\sin\theta A_{r,\theta})_{,r} = \frac{1}{4\pi\sqrt{-g}}(e^{\Phi-\Lambda}\sin\theta e^{\Lambda-\Phi}\Sigma_{,\theta})_{,r} = \\ &= \frac{\sin\theta\Sigma_{,\theta r}}{4\pi\sqrt{-g}} = \frac{e^{\Phi-\Lambda}(\Sigma_{,\theta})_{,r}}{4\pi r^2}. \end{aligned} \quad (2.50)$$

CHAPTER 2. STATIC MAGNETIC EQUILIBRIA

Substituting J^r , J^θ and $A_\phi = \psi$ in equation (2.46) we obtain:

$$f_\phi = \frac{e^{\Phi-\Lambda}}{4\pi r^2} (\cot \theta \Sigma_{,\theta} + \Sigma_{,\theta\theta}) \psi_{,r} - \frac{e^{\Phi-\Lambda} \Sigma_{,\theta r}}{4\pi r^2} \psi_{,\theta} = 0 \quad (2.51)$$

i.e.:

$$(\Sigma_{,\theta\theta} + \cot \theta \Sigma_{,\theta}) \psi_{,r} - \Sigma_{,\theta r} \psi_{,\theta} = 0. \quad (2.52)$$

By defining:

$$\tilde{\psi} \equiv \sin \theta \Sigma_{,\theta} \quad (2.53)$$

equation (2.52) becomes:

$$\tilde{\psi}_{,\theta} \psi_{,r} - \tilde{\psi}_{,r} \psi_{,\theta} = 0 \quad (2.54)$$

that means that $\tilde{\psi}$ is function of ψ :

$$\tilde{\psi} = \tilde{\psi}(\psi). \quad (2.55)$$

Because ψ and $\tilde{\psi}$ are of the same order the dependence of $\tilde{\psi}$ on ψ must be linear. A possible solution is given by:

$$\tilde{\psi} = \zeta \psi \quad (2.56)$$

with ζ constant coefficient. Using (2.53), the equation (2.56) becomes:

$$\sin \theta \Sigma_{,\theta} = \zeta \psi \quad (2.57)$$

that is satisfied only if:

$$\Sigma = \zeta a \quad (2.58)$$

$$\psi = \sin \theta a_{,\theta} \quad (2.59)$$

where a is a function of r and θ : $a = a(x^a)$. Considering (2.58) and (2.59), the potential vector defined in (2.41) becomes:

$$A_\mu = (0, \zeta e^{\Lambda-\Phi} a, 0, \sin \theta a_{,\theta}) \quad (2.60)$$

i.e. A_μ depends only on the $x^a = r, \theta$ coordinates because a is a function of r, θ ($a = a(x^a)$) and ζ is a constant.

The relation between the magnetic field and the potential vector is given by:

$$B^\mu = -\epsilon^{\mu\nu\alpha\beta} u_\nu \partial_\beta A_\alpha. \quad (2.61)$$

From equation (2.61) we can find the form of the magnetic field and, in particular, we will show that the toroidal component of the magnetic field (B^ϕ) is linked to the A_r component while the poloidal component of the magnetic field

(B^r, B^θ) is linked to the A_ϕ component of the potential vector. If we substitute in the equation (2.61) the components A_r and A_ϕ (the only non-zero two components of the potential vector A_μ), we get

$$B^\mu = -\epsilon^{\mu\nu r\beta} u_\nu \partial_\beta A_r \quad (2.62)$$

$$B^\mu = -\epsilon^{\mu\nu\phi\beta} u_\nu \partial_\beta A_\phi. \quad (2.63)$$

The Levi Civita tensor $\epsilon^{\mu\nu\alpha\beta}$ for the metric (2.1) is $\epsilon^{tr\theta\phi} = (\sqrt{-g})^{-1} = (e^{\Phi+\Lambda} r^2 \sin \theta)^{-1}$ and it is zero if two of its indices are equal. Because of the antisymmetry of the Levi-Civita tensor and because of the dependence of A_μ just on the $x^a = r, \theta$ coordinates, the equations (2.62) and (2.63) become:

$$B^r = -\rho^{r\nu\phi\theta} u_\nu \partial_\theta A_\phi = -\epsilon^{rt\phi\theta} u_t \partial_\theta A_\phi = \frac{e^{-\Lambda}}{r^2 \sin \theta} (\sin \theta a, \theta), \theta \quad (2.64)$$

and

$$B^\theta = -\epsilon^{\theta\nu\phi r} u_\nu \partial_r A_\phi = -\rho^{\theta t\phi r} u_t \partial_r A_\phi = -\frac{e^{-\Lambda}}{r^2 \sin \theta} (\sin \theta a, \theta), r. \quad (2.65)$$

From those two equations it is clear that the poloidal component of the magnetic field is function only of A_ϕ . For the toroidal component B^ϕ of the magnetic field, it follows from equation (2.62) that the only non trivial contribution is the one for the index $\Phi = t$ and so we get:

$$B^\phi = -\epsilon^{\phi t\theta r} u_t \partial_\theta A_r = -\frac{e^{-\Lambda}}{r^2 \sin \theta} (\zeta e^{\Lambda-\Phi} a, \theta) \quad (2.66)$$

that shows the dependence only on A_r of the toroidal magnetic field. At the end, we can write the magnetic field as:

$$B_\mu = \frac{e^{-\Lambda}}{\sin \theta} \left(0, \frac{e^\Lambda}{r^2} (\sin \theta a, \theta), \theta, -(\sin \theta a, \theta), r, -\zeta \sin^2 \theta e^{\Lambda-\Phi} a, \theta \right). \quad (2.67)$$

Note that for $\zeta = 0$ the toroidal field is null.

2.3 The source of the magnetic field

The magnetic field given in (2.67) is created by a four-current J^μ : we will show that the toroidal and the poloidal magnetic fields are generated by different components of the four-current. The component of the four-current J^μ can be calculated by the equations (2.49) and (2.50), by substituting $\Sigma = \zeta a(r, \theta)$ (as it

follows from equations (2.58)):

$$\begin{aligned} J^r &= -\frac{e^{\Phi+\Lambda}}{4\pi r^2}(\cot\theta\Sigma_{,\theta} + \Sigma_{,\theta\theta}) \\ &= -\frac{\zeta e^{\Phi+\Lambda}}{4\pi r^2}(\cot\theta a_{,\theta} + a_{,\theta\theta}) = -\frac{\zeta e^{\Phi+\Lambda}}{4\pi r^2 \sin\theta}(\sin\theta a_{,\theta})_{,\theta} \end{aligned} \quad (2.68)$$

$$J^\theta = \frac{e^{\Phi+\Lambda}}{4\pi r^2}(\Sigma_{,\theta})_{,r} = \frac{\zeta e^{\Phi+\Lambda}}{4\pi r^2}(a_{,\theta})_{,r} = \frac{\zeta e^{\Phi+\Lambda}}{4\pi r^2 \sin\theta}(\sin\theta a_{,\theta})_{,r}. \quad (2.69)$$

The calculation for the J^ϕ component is more complicated and it is more convenient to calculate it, starting from the Lorentz force f_a , defined in equation (2.42)), and using the expression for the tensor $F_{\mu\nu}$ defined in equation (2.27). In this way we get:

$$f_a = F_{a\alpha}J^\alpha \quad \rightarrow \quad f_a = (\sin\theta a_{,\theta})_{,a} \frac{\tilde{J}_\phi}{r^2 \sin^2\theta} \quad (2.70)$$

where we defined:

$$\tilde{J}_\phi = J_\phi - \frac{\zeta^2 e^{-\Phi}}{4\pi} \sin\theta a_{,\theta}. \quad (2.71)$$

The first member of equation (2.70) can be written using the Euler equation (2.44):

$$f_a = (P + \rho)u^\mu u_{a;\nu} + P_{,a} + u_a u^\mu P_{,\mu} \quad (2.72)$$

so that we get:

$$(P + \rho)u^\mu u_{a;\nu} + P_{,a} + u_a u^\mu P_{,\mu} = F_{a\mu}J^\mu. \quad (2.73)$$

From the definitions for J^r and J^θ given in equations (2.68) and (2.69), equation (2.73) for $\mu \equiv r, \theta$ can be written as:

$$\chi_{,r} = A_{\phi,r} \tilde{J}^\phi \quad \text{and} \quad \chi_{,\theta} = A_{\phi,\theta} \tilde{J}^\phi \quad (2.74)$$

where χ is a function of r and θ , given by:

$$\chi_{,a} = [\Phi + C_s^2(\ln n)]_{,a} \quad (2.75)$$

where C_s is the sound speed and n is the number density of the particles. In the equation (2.75) we have use the first law of thermodynamics:

$$d\rho = (\rho + P) \frac{dn}{n} \quad (2.76)$$

where ρ is the energy density of the fluid. Using the integrability condition $\chi_{,r\theta} - \chi_{,\theta r} = 0$ together with the equations (2.75), we get:

$$\begin{aligned} \chi_{,r\theta} - \chi_{,\theta r} = 0 &= \\ &= (\sin \theta a_{,\theta})_{,r} \left(\frac{\tilde{J}_\phi}{r^2 \sin^2 \theta (P + \rho)} \right)_{,\theta} - (\sin \theta a_{,\theta})_{,\theta} \left(\frac{\tilde{J}_\phi}{r^2 \sin^2 \theta (P + \rho)} \right)_{,r} \end{aligned} \quad (2.77)$$

From this equation we can deduce that $\tilde{J}_\phi / (r^2 \sin^2 \theta)$ is a function of $(\sin \theta a_{,\theta})$ and, because $\tilde{J}_\phi / (r^2 \sin^2 \theta (P + \rho))$ and $(\sin \theta a_{,\theta})$ are of the same order of magnitude then the dependence of $\tilde{J}_\phi / (r^2 \sin^2 \theta (P + \rho))$ on $(\sin \theta a_{,\theta})$ must be:

$$\frac{\tilde{J}_\phi}{(r^2 \sin^2 \theta (P + \rho))} = c_0 + c_1 \sin \theta a_{,\theta} \quad (2.78)$$

where c_0 and c_1 are constants. From the definition of \tilde{J}^ϕ given in (2.71), we obtain the J_ϕ component of the four current:

$$\begin{aligned} J_\phi &= \zeta^2 \frac{e^{-\Phi}}{4\pi} \sin \theta a_{,\theta} + \tilde{J}_\phi \\ &= \zeta^2 \frac{e^{-\Phi}}{4\pi} \sin \theta a_{,\theta} + [c_0 + c_1 \sin \theta a_{,\theta}] (P + \rho) r^2 \sin^2 \theta \end{aligned} \quad (2.79)$$

To summarize the components of the four-current are given by:

$$\begin{aligned} J_t &= 0 \\ J_r &= -\frac{\zeta e^{\Lambda - \Phi}}{4\pi r^2 \sin \theta} (\sin \theta a_{,\theta})_{,\theta} \\ J_\theta &= \frac{\zeta e^{-(\Phi + \Lambda)}}{4\pi \sin \theta} (\sin \theta a_{,\theta})_{,r} \\ J_\phi &= \zeta^2 \frac{e^{-2\Phi}}{4\pi} \sin \theta a_{,\theta} + [c_0 + c_1 \sin \theta a_{,\theta}] (P + \rho) r^2 \sin^2 \theta \end{aligned} \quad (2.80)$$

We can divide the four-current J^μ in two parts:

$$J_\mu = J_\mu^{\text{pol}} + J_\mu^{\text{force free}} \quad (2.81)$$

where

$$J_\mu^{\text{pol}} = (0, 0, 0, [c_0 + c_1 \sin \theta a_{,\theta}] (P + \rho) r^2 \sin^2 \theta) \quad (2.82)$$

$$J_\mu^{\text{force free}} = -\frac{\zeta e^{-2\Phi}}{4\pi} B_\mu \quad (2.83)$$

as we can find, substituting in (2.80) the expression for B_μ given in (2.67). The J_μ^{pol} current is the source of the poloidal magnetic field, while $J_\mu^{\text{force free}}$ is the source of a mixed magnetic field, with both poloidal and toroidal components. The $J_\mu^{\text{force free}}$ is parallel to the magnetic field and it is called force-free current, because the Lorentz force associated with it is null. In fact, if we consider the Lorentz force given in (2.42)

$$f_\mu = F_{\mu\alpha} J^\alpha \quad (2.84)$$

we can see that $F_{\mu\alpha} B^\alpha = 0$, and so there is no Lorentz force associated with $J_\mu^{\text{force free}}$.

We observe that if $c_0 = c_1 = 0$, then $J_\mu^{\text{pol}} = 0$: $J_\mu^{\text{force free}}$ is the only current present, and the total Lorentz force is equal to zero. On the other hand, if $\zeta = 0$, then $J_\mu^{\text{force free}} = 0$, and the magnetic field is just poloidal.

2.4 The Grad-Shavranov equation

Now, we know the expression for the magnetic field, as well as the expression for the source of this latter. We will use those information to derive the equation that describes the magnetic field inside the star as well as outside the star, in the vacuum. This equation is known in literature as the Grad-Shafranov equation [38], [39].

We start expanding in Legendre Polynomials P_ℓ the function $a(x^a)$, present in the potential vector (2.60):

$$a(r, \theta) = \sum_{\ell=1}^{\infty} a_\ell(r) P_\ell(\theta). \quad (2.85)$$

In this way A_μ defined in (2.60) becomes:

$$A_\mu = \left(0, \zeta e^{2\Lambda - 2\Phi} \sum_{\ell} a_\ell P_\ell, 0, \sum_{\ell} a_\ell \sin \theta \partial_\theta P_\ell \right) \quad (2.86)$$

while the magnetic field B^μ given in (2.67) becomes:

$$B_\mu = \left(0, -\frac{\ell(\ell+1)P_\ell a_\ell}{r^2} e^\Lambda, -a'_\ell \partial_\theta P_\ell e^{-\Lambda}, -\sin \theta \zeta \partial_\theta P_\ell a_\ell e^{-\Phi} \right) \quad (2.87)$$

where with the symbol ($'$) we indicate the derivative respect to r . In the equation (2.87), we have used the following properties of the Legendre Polynomials:

$$\partial_{\theta\theta} P_\ell + \cot \theta \partial_\theta P_\ell - \ell(\ell+1) P_\ell = 0 \quad (2.88)$$

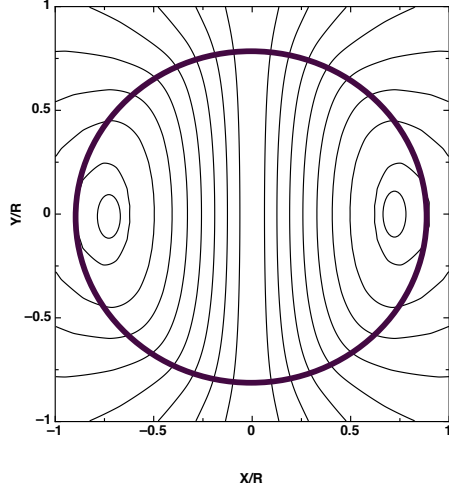


Figure 2.1: The magnetic field lines for the equilibrium stellar model with $\zeta = 0$ and equation of state APR₁₄, where the subscript 14 refers to the stellar mass. i.e. the mass of the model is $M = 1.4M_{\odot}$.

and $P_1 = \cos \theta$. Note that in the case of a dipole field (for $\ell = 1$) our equation becomes:

$$B_{\mu} = \left(0, -\frac{2 \cos \theta a_1}{r^2} e^{\Lambda}, a_1' \sin \theta e^{-\Lambda}, \sin^2 \theta \zeta a_1 e^{-\Phi} \right). \quad (2.89)$$

A plot of the magnetic field lines is shown in Figure 2.1.

To calculate the Grad-Shafranov equation, we need to calculate the ϕ component of the Maxwell equations:

$$F_{\phi}^{\mu}{}_{;\mu} = 4\pi J_{\phi}. \quad (2.90)$$

We can rewrite the first term of the (2.90) equations as:

$$\begin{aligned} F_{\phi}^{\mu}{}_{;\mu} &= (g^{\mu\delta} F_{\phi\delta})_{;\mu} = [g^{\mu\delta} (A_{\delta, \phi} - A_{\phi, \delta})]_{;\mu} \\ &= -[g^{\mu\delta} A_{\phi, \delta}]_{;\mu} = -[g^{\theta\theta} A_{\phi, \theta}]_{;\theta} - [g^{rr} A_{\phi, r}]_{;r}. \end{aligned} \quad (2.91)$$

Using (2.86), we get:

$$F_{\phi}^{\mu}{}_{;\mu} = -\frac{\sin \theta}{4\pi} \sum_{\ell} \partial_{\theta} P_{\ell} \left(e^{-2\Lambda} \partial_{rr} a_{\ell} + (\Phi_{,r} - \Lambda_{,r}) e^{-2\Lambda} \partial_r a_{\ell} - \frac{\ell(\ell+1)}{r^2} a_{\ell} \right). \quad (2.92)$$

The J_{ϕ} component of the four-current, given in equation (2.79), when it is ex-

panded in Legendre Polynomials, becomes :

$$\begin{aligned} J_\phi &= \zeta^2 \frac{e^{-2\Phi}}{4\pi} \sum_\ell a_\ell \sin \theta \partial_\theta P_\ell + (P + \rho)r^2 \sin^2 \theta \left[c_0 + c_1 \sin \theta \sum_\ell a_\ell \partial_\theta P_\ell \right] \\ &= \sum_\ell \sin \theta \left(a_\ell \zeta^2 \frac{e^{-\Phi}}{4\pi} \partial_\theta P_\ell - (P + \rho)r^2 c_0 \partial_\theta P_1 \right) + \text{terms in } c_1 \end{aligned} \quad (2.93)$$

where we set $P_1 = \cos \theta$ and $\sin \theta = -\partial_\theta P_1$.

Now we project the expression (2.93) on different Legendre Polynomials, calculating the integrals:

$$\int_0^\pi J_\phi(\theta) P_{\ell'}(\theta) \sin \theta d\theta \quad (2.94)$$

and using the orthogonality property:

$$\frac{2\ell + 1}{2} \int_0^\pi P_\ell(\theta) P_{\ell'}(\theta) \sin \theta d\theta = \delta_{\ell\ell'}. \quad (2.95)$$

The terms in c_1 couple terms with ℓ indice to terms with indices $\ell \pm 2$. We will neglect such terms because the contribution of terms with $\ell > 2$ to the magnetic field is negligible. In this way we have for $\ell = 1$:

$$e^{-2\Lambda} a_1'' + (\Phi' - \Lambda') e^{-2\Lambda} a_1' + \left(\zeta^2 e^{-2\Phi} - \frac{2}{r^2} \right) a_1 = 4\pi(\rho + P)r^2 c_0, \quad (2.96)$$

while for $\ell > 1$, the Grad-Shafranov equation gets the form:

$$e^{-2\Lambda} a_\ell'' + (\Phi' - \Lambda') e^{-2\Lambda} a_\ell' + \left(\zeta^2 e^{-2\Phi} - \frac{\ell(\ell + 1)}{r^2} \right) a_\ell = 0. \quad (2.97)$$

In the following we will consider just the $\ell = 1$ term in (2.96), because this is the one that gives the dominant contribute to the magnetic field of the star.

The equation (2.96) is a non-homogeneous, ordinary, differential equation of second order, linear in a_1 , with a source term given by $4\pi(\rho + P)r^2 c_0$. This term is linked to the J_{pol}^μ current (see equation (2.82)). For the numerical integration of the equation (2.96), we have to separate them in two differential equations of the first order in a_1 :

$$\frac{da_1}{dr} = a_1' \quad (2.98)$$

$$\frac{da_1'}{dr} = e^{2\Lambda} \left(-\zeta^2 e^{-2\Phi} + \frac{2}{r^2} \right) a_1 - 4\pi(\rho + P)r^2 c_0 e^{2\Lambda} - (\Phi' + \Lambda') a_1' \quad (2.99)$$

The next step is to assign the initial conditions and the boundary conditions on the stellar surface. On the exterior, in the vacuum, we assume the existence

of a magnetic dipolar field. The presence of a poloidal magnetic field outside the star doesn't imply the presence of currents there. Since we assume that the exterior magnetic field is just poloidal, then we must demand that the $J_\mu^{\text{force free}}$ is zero in the exterior of the star, because this current is proportional to ζ , the constant that represents the ratio between toroidal and poloidal components of the magnetic field. Setting $\zeta = 0$ implies automatically $J_\mu^{\text{force free}} = 0$. The second current J_μ^{pol} is equal to zero outside, since it is proportional to the pressure and the density of the star (that outside, in the vacuum, are vanishing)

The condition at the center of the star is:

$$a_1 \simeq \alpha_0 r^2 + \dots \quad (2.100)$$

where α_0 is an arbitrary constant and it can be found integrating the equation (2.96) and putting $\alpha_0 = 1$ and then searching for the value of α_0 that allows a_1 to match on the surface, with the analytic solution of dipole magnetic field on the exterior of the star, given by [40],[41]:

$$a_1^{\text{dip}} = -\frac{3\mu_0}{8M^3} r^2 \left[\ln\left(1 - \frac{2M}{r}\right) + \frac{2M}{r} + \frac{2M^2}{r^2} \right] \quad (2.101)$$

where μ_0 is a constant that represents the magnetic-dipole momentum of the star, M is the mass of the star. The value of μ_0 is chosen so that the magnetic field on the stellar surface is around $B = 4 \times 10^{15}$ Gauss.

Our configurations can have both a poloidal and a toroidal component, with different strength. This can be achieved by choosing different values for the constant ζ . A value of ζ different from zero means that a toroidal field is present. ζ can take any value from zero until a maximal value ζ_{max} . If ζ exceeds this maximum, then the current changes sign in some region inside the star. A change in the sign of the current could drive the magnetic field towards a catastrophic instability, although the star will remain stable. For this reason, we will analyse only models that have $\zeta \leq \zeta_{\text{max}}$. Note that the maximum value of ζ_{max} takes different values when we consider different stellar models.

Solving equation (2.96) we can find the distribution of the magnetic field in the star and, as next step, we can derive the perturbation equations for the oscillations of a star endowed with a magnetic field described by (2.96). In figure (2.2), different models of stellar equilibrium with a dipole magnetic field are plotted. The subscript in each model indicates the mass: for all the models plotted in figure (2.2) the mass is $M = 1.4 M_\odot$ and no toroidal field is present ($\zeta = 0$).

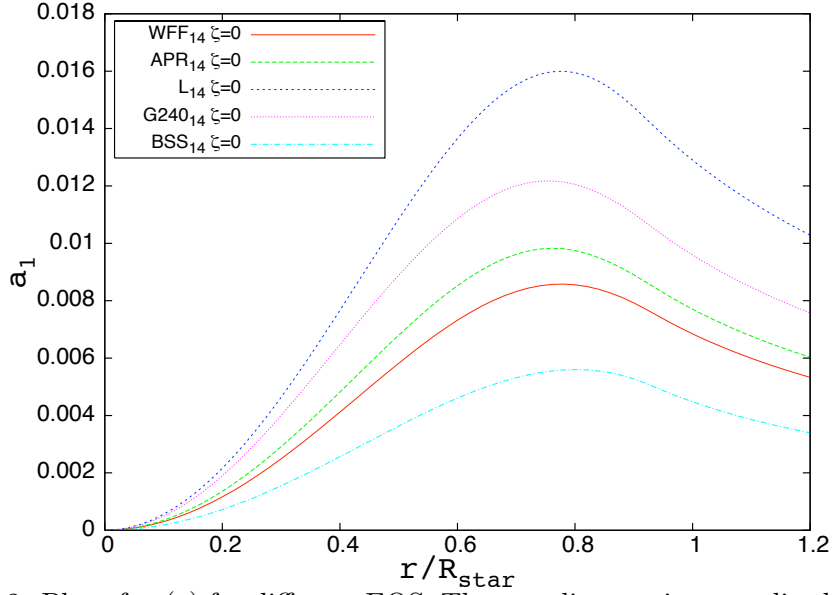


Figure 2.2: Plot of $a_1(r)$ for different EOS. The coordinate r is normalized to the stellar radius

2.4.1 Equation of state used

The description the state of the matter above the nuclear density ($\rho = 2.67 \times 10^{14} \text{ g/cm}^3$) is not an easy task. Since it is not possible to reproduce these extreme density in the laboratory, it is necessary to model the nuclear matter, and to constrain the models with observations either in the electromagnetic spectrum or in the near future in the gravitational wave spectrum. Two approaches are used:

- non relativistic nuclear many bodies theories
- relativistic mean field theory.

The model based on the WFF EOS [42] is based on the first approach and models the stellar matter as a mixture of neutrons, protons, electrons and muons in β -equilibrium. A three body potential is added to a two nucleon potential, in order to fit better the observed properties of a three nucleons bound state. The APR model [43] shares the basic properties of the WFF EOS and it is based on the two- and three- body interaction, but it uses the potential (Argonne v_{18}) and a large number of nucleon-nucleon scattering data were used in its construction. This leads to a qualitative change in the high density region of the neutron star

with respect to other models: i.e. a phase transition is allowed to occur in this region.

The APR2 [44] is an improvement of the APR1 model: it takes into account relativistic effects and the three-body potential is modified in order to better fit the experimental three-nucleon scattering data. The BSS model [45] is a modification of the APR1 model and it consists in nucleons and leptons (as for the APR1) with addition of strange baryons, as Λ^0 and Σ^- . Hyperon-nucleon interactions are taken into account while the hyperon-hyperon interactions are neglected.

The EOS L [46] is based on the relativistic mean field theory: the neutrons are assumed to interact through the two vector mesons, ω and ρ , and one scalar meson, σ . This latter interaction is completely based on relativistic mean fields, while the other two are governed by non relativistic field theory. This equation of state is particularly stiff (the stiffness is defined as the ratio between radius and mass). Also the EOS G240 is based on relativistic mean field theory and includes the full baryon octet, consisting of protons, neutrons and $\Sigma^{\pm 0}$, Ξ^{\pm} and Λ^0 particles .

3

Magnetic oscillations equation

In this chapter, we study linear perturbation of a magnetised, non-rotating neutron stars. We perturb the equilibrium model described in the previous chapter, using the so called Cowling approximation. This approximation, introduced for first by Cowling in his study on Newtonian polytropic neutron stars (see[47]), consists on neglecting the perturbation of the gravitational potential. The Cowling approximation is a quite good approximation, if the mass of the star is concentrated near the centre: in this case, density variation will not cause large variations of the gravitational field on the outer layers of the neutron star, that are the ones that influence stronger the frequency of the oscillation modes. In general relativity, the Cowling approximation leads in neglecting the metric perturbations [48] , i.e. setting $\delta g_{\mu\nu} = 0$. The quality of this approximation depends on the type of oscillations modes under consideration, as well as, on the order of the mode. The torsional oscillation modes, that we consider there, can be computed accurately, since those oscillations are of axial types and don't induce a density variation in a spherical star. Using the Cowling approximation, the number of the equations to deal is reduced considerably, because we don't have to consider the evolution in time of the metric perturbation $\delta g_{\mu\nu}$.

Let's see in more details the effect of a perturbation on a star in equilibrium.

When a perturbation is introduced on a star, it responds with oscillations of different type. A classification of those modes can be based on their parity. In fact, by decomposing them in spherical harmonics and by operating a parity

transformation $r \rightarrow -r$, we can determine if a mode transforms as $(-1)^\ell$ or as $(-1)^{\ell+1}$: in the first case the modes are called polar modes (or spheroidal modes) while in the second case they are called axial modes (or toroidal modes). Among these two kinds of oscillations, an additional distinction can be made considering what kind of force is acting in order to restore any deviation from equilibrium. For example, for a Newtonian, non-rotating star, the polar modes could be classified as:

p(ressure)–**modes**: they are high frequency modes and their restoring force is pressure. The amplitude of these modes is larger in the outer layers of the star than in the central part. The lowest *p*–mode has a frequency around 5kHz. For a fixed n (order of the mode), their frequency increases with ℓ .

g(ravity)–**modes**: for these modes, the restoring force is the gravity. Unlike the *p*–modes, the *g*–modes have larger amplitude in the centre than in the outer layers. Their frequencies are usually smaller than the *p*–modes. The *g*–modes are non radial oscillations: in fact, they are generated when a fluid element, that has moved upwards, is pushed back in its original position by the buoyancy force. In order to move vertically the fluid element has to displace the surrounding stellar matter horizontally. In this way a non radial oscillation is created in response.

f(undamental)–**mode**: it is the fundamental mode and its eigenfunction has no-radial nodes. Its frequency is around few kHz and is lower than the *p*–modes. Sometimes, it can be considered as the fundamental *p*–modes.

i(nertial)–**modes**: the restoring force of these modes is the Coriolis force: for this reason, they exists only in rotating stars. The *r*–modes are a subgroup of inertial modes and are characterized by their non-axisymmetric nature.

It is worth to mention that Robé shown in [49] that the mode that it is predominantly affected by the Cowling approximation is the *f*–mode while the *g*–modes and *p*–modes are affected only slightly.

w–**modes**: if we consider a relativistic neutron stars, a family of modes that has not Newtonian counterpart, shows up. This family of modes was first discovered by Kokkotas & Schutz [50]: they call these modes *w*–modes (gravitational ‘w’ave), because these particular modes are directly related to perturbations in the space-time while they hardly produce any significant fluid oscillations. The lowest frequency occurs at 5 kHz. These modes have been divided in many subgroups, see Kokkotas & Schmid [51] for more details.

Among the axial modes, we remember:

t(orsional)–modes: these modes imply a torsion of the crust, so no perturbation of the fluid density is involved. They are called torsional modes and their lower frequency is about few Hz.

In this thesis, we focus on the last type of axial modes: the torsional oscillation modes. Those modes are most likely to be excited by a crust fracture because they are divergence free toroidal excitation and involve just a small density fluctuation (that can be neglect), as it was already noticed in [22].

In the following, we will not consider deformation on the stellar shape due to the presence of the magnetic field, because the magnetic energy \mathcal{E}_M is many orders of magnitude smaller than the gravitational bounding energy \mathcal{E}_G :

$$\frac{\mathcal{E}_M}{\mathcal{E}_G} = \frac{B^2 R^2}{GM^2/R} \sim 10^{-4} \left(\frac{B}{10^{16}G} \right)^2 \quad (3.1)$$

3.1 Perturbation equations

For a magnetised star in equilibrium the energy-momentum tensor is given by the sum of the perfect fluid energy-momentum ($T_{\text{fluid}}^{\mu\nu}$) and the one given by the magnetic field ($T_{\text{em}}^{\mu\nu}$):

$$T_{\text{tot}}^{\mu\nu} = T_{\text{fluid}}^{\mu\nu} + T_{\text{em}}^{\mu\nu} \quad (3.2)$$

$$T_{\text{em}}^{\mu\nu} = \frac{1}{4\pi} \left[(u^\mu u^\nu + \frac{1}{2} g^{\mu\nu}) B^2 - B^\mu B^\nu \right] \quad (3.3)$$

$$T_{\text{fluid}}^{\mu\nu} = (P + \rho) u^\mu u^\nu + P g^{\mu\nu}. \quad (3.4)$$

In equation (3.3), u^μ is the four velocity that, in the not perturbed case, has only one non-zero component, u^t , and it is given by:

$$g_{\mu\nu} u^\mu u^\nu = -1 \quad \rightarrow \quad u^t = e^{-\Phi} \quad u_t = -e^\Phi \quad (3.5)$$

The energy-momentum tensor (3.2) obeys to a conservation law:

$$T_{;\nu}^{\sigma\nu} = 0 \quad (3.6)$$

The equations of the fluid's motion can be obtained by projecting equation (3.6) on the hypersurface normal to u^μ , in the following way:

$$h_\sigma^\mu T_{;\nu}^{\sigma\nu} = 0 \quad (3.7)$$

where

$$h_\mu^\nu = g_\mu^\nu + u_\mu u^\nu \quad (3.8)$$

is the projection tensor. From the equation (3.7), we obtain:

$$(\rho + P + B^2)u^\mu_{;\nu}u^\nu = -h^{\mu\nu} \left(P + \frac{1}{2}B^2 \right) + h^\mu_\sigma (B^\sigma B^\nu)_{;\nu}. \quad (3.9)$$

In order to study the torsional oscillations, we need a second equation that involves the magnetic field: the magnetic induction equation. This equation can be derived from the Maxwell equation (2.25) and it is given by:

$$(u^\mu B^\nu - u^\nu B^\mu)_{;\mu} = 0 \quad (3.10)$$

The equation (3.10) can be rewritten as:

$$B^\mu_{;\nu}u^\nu = u^\alpha B^\mu + u^\mu B_\nu + B^\alpha u_{\alpha;\beta}u^\beta u^\mu. \quad (3.11)$$

Equation (3.11) together with equation (3.9) give us a set of equations, that connect with each other the magnetic field structure and the fluid proprieties, as density and pressure. In order to study the toroidal oscillations, we have to perturb both equations (3.9) and (3.11) and find how matter embedded in a magnetic field reacts to such perturbation. We perform a linear perturbation of such equation. In a linear perturbation, each tensorial quantity $X_{\mu_1\dots}$ is indicated as:

$$X_{\mu_1\dots} = X_{\mu_1\dots} + \delta X_{\mu_1\dots} \quad (3.12)$$

where δ indicates the perturbations to the first order. All the physical quantities will be perturbed in such way, except the metric tensor $g_{\mu\nu}$, because, as we already pointed out, we work in the Cowling approximation, that means $\delta g_{\mu\nu} = 0$.

The linearized form of the equation of motion (3.9) is given by:

$$\begin{aligned} (\rho + P + B)\delta u^\mu_{;\nu}u^\nu &= -(\delta\rho + \delta P + 2B_\sigma\delta B^\sigma)u^\mu_{;\nu}u^\nu - (\rho + P + B)u^\mu_{;\nu}\delta u^\nu \\ &\quad + (u^\mu\delta u_\sigma + u_\sigma\delta u^\mu) \left[B^\mu B^\nu - g^{\sigma\nu} \left(P + \frac{1}{2}B^2 \right) \right]_{;\nu} \\ &\quad + h^\mu_{;\sigma} \left[B^\sigma\delta B^\nu + \delta B^\sigma B^\nu - g^{\sigma\nu}(\delta P + B_\alpha B^\alpha) \right]_{;\nu} \\ &\quad - h^\mu_\sigma\delta T^{\sigma\nu(s)}_{;\nu} \end{aligned} \quad (3.13)$$

where $T^{\mu\nu(s)}$ is the linearized shear stress tensor. The shear tensor is related to the linearized shear tensor $\delta S_{\mu\nu}$ through (see [52]):

$$\delta T^{\sigma\nu(s)} = -2\mu\delta S^{\mu\nu} \quad (3.14)$$

where μ is the shear modulus. The linearized form of equation (3.11) is instead (see [24]) given by:

$$\begin{aligned} \delta B^{\mu}_{;\nu} u^{\nu} = & B^{\mu}_{;\nu} \delta u^{\nu} + h^{\mu\alpha} u_{\alpha;\sigma} \delta B^{\sigma} + h^{\mu\alpha} \delta u_{\alpha;\sigma} B^{\sigma} \\ & + u^{\mu} \delta u^{\alpha} B^{\sigma} u_{\alpha;\sigma} + u^{\mu} B^{\alpha} (\delta u_{\alpha;\sigma} u^{\sigma} + u_{\alpha;\sigma} \delta u^{\sigma}) + \\ & (B^{\alpha} \delta u^{\mu} + \delta B^{\alpha} u^{\mu}) u_{\alpha\sigma} u^{\sigma} + \delta u^{\sigma}_{;\sigma} B^{\mu} + u^{\sigma}_{;\sigma} \delta B^{\mu} \end{aligned} \quad (3.15)$$

where we used $u^{\alpha} \delta u_{\alpha;\beta} = -\delta u^{\alpha} u_{\alpha;\beta}$. Equations (3.13) and (3.15) can be simplified even further since we are considering axial-type perturbations, i.e. perturbations that don't involve density variation and we are neglecting the presence of meridional currents (that can be present when a toroidal field is present, see [53]). In this special case, we can set:

$$\delta \rho = 0, \quad \delta P = 0 \quad (3.16)$$

$$\delta u^t = 0, \quad \delta u^r = 0, \quad \delta u^{\theta} = 0. \quad (3.17)$$

The only perturbation on the fluid's velocity is then given by δu^{ϕ} . A perturbation on the fluid velocity means that a fluid element is displaced from its original position: we indicate such angular and radial displacement of the stellar matter as $\mathcal{Y}(r, \theta)$, following the formalism of [24]. The link between the perturbation of the azimuthal velocity δu^{ϕ} and the stellar displacement, is given by:

$$\delta u^{\phi} = e^{-\Phi} \partial_t \mathcal{Y}(t, r, \theta) \quad (3.18)$$

where with ∂_t we indicate the partial derivative respect to the time.

Our aim is to obtain a unique equation for the time-space evolution of the quantity $\mathcal{Y}(r, \theta)$ by using the linearized induction equations (3.15) and the linearized equations of motion (3.13). In order to proceed, we have, then, to get an explicit expression for all the quantities included in this two expressions, like, for example the stress energy tensor $T^{\mu\nu(s)}$, present in equation (3.13), and the perturbed magnetic field δB^{μ} .

We begin by deriving the explicit form of the stress energy tensor $T^{\mu\nu(s)}$, present in equation (3.13), for our model. The stress energy tensor $T^{\mu\nu(s)}$ is related to the shear tensor $S^{\mu\nu}$ by the equation (3.14). Then we need to find the components of the shear tensor $S^{\mu\nu}$, in order to define the stress energy tensor $T^{\mu\nu(s)}$.

First we consider that in a comoving frame, the components of $S_{\alpha\beta}$ are purely spatial, i.e.:

$$S_{00} = 0, \quad S_{i0} = 0, \quad S_{0i} = 0. \quad (3.19)$$

CHAPTER 3. MAGNETIC OSCILLATIONS EQUATION

In addition, we should take into account the stress tensor $S_{\alpha\beta}$ is traceless:

$$S_{ii} = 0. \quad (3.20)$$

The remaining components of $S_{\mu\nu}$ can be calculated, using the rate of shear $\sigma_{\alpha\beta}$, defined as:

$$\sigma_{\alpha\beta} = \frac{1}{2}(u_{\alpha;\mu}h_{\beta}^{\mu} + u_{\mu;\alpha}h_{\alpha}^{\mu}) - \frac{1}{3}h_{\alpha\beta}u^{\mu}{}_{;\mu}. \quad (3.21)$$

In fact, the rate of shear $\sigma_{\alpha\beta}$ is linked to the shear tensor $S_{\alpha\beta}$ by the relation:

$$\sigma_{\alpha\beta} = \mathcal{L}_u S_{\alpha\beta} \quad (3.22)$$

where \mathcal{L} is the Lie derivative of the shear tensor along a world line. The equation (3.22) can be written as

$$\sigma_{\alpha\beta} = u^{\mu}{}_{;\alpha}S_{\mu\beta} + u^{\mu}{}_{;\beta}S_{\mu\alpha} + u^{\mu}S_{\alpha\beta}{}_{;\mu}. \quad (3.23)$$

Keeping only the linear terms, the equation (3.23) reduces to:

$$\sigma_{\alpha\beta} = e^{-\phi}S_{\alpha\beta,t} \quad (3.24)$$

from which we find easily:

$$S_{\alpha\beta,t} = \sigma_{\alpha\beta}e^{\phi}. \quad (3.25)$$

Our aim is to find an explicit expression for the perturbed stress tensor $\delta S_{\alpha\beta}$ present in equation (3.14): for this reason we perturb equation (3.25) and find:

$$\delta S_{\alpha\beta,t} = \delta\sigma_{\alpha\beta}e^{\phi} \quad (3.26)$$

The perturbed terms of the rate of shear $\sigma_{\alpha\beta}$ can be derived from equation (3.21). In the Cowling approximation and linear regime, the only non-trivial components of the perturbed equation (3.21) are:

$$\delta\sigma_{r\phi} = \frac{1}{2}r^2e^{-\Phi}\mathcal{Y}_{,tr}\sin^2\theta \text{ and } \delta\sigma_{\theta\phi} = \frac{1}{2}r^2e^{-\Phi}\mathcal{Y}_{,t\theta}\sin^2\theta. \quad (3.27)$$

Substituting the results (3.27) in equation (3.26) and by integrating in time, we find:

$$\delta S_{r\phi} = \frac{1}{2}r^2\mathcal{Y}_{,r}\sin^2\theta \text{ and } \delta S_{\theta\phi} = \frac{1}{2}r^2\mathcal{Y}_{,\theta}\sin^2\theta \quad (3.28)$$

Substituting the equation (3.28) in equation (3.14), we get finally:

$$\delta T_{r\phi}^{(s)} = -\mu r^2\mathcal{Y}_{,r}\sin^2\theta \quad (3.29)$$

$$\delta T_{\theta\phi}^{(s)} = -\mu r^2 \mathcal{Y}_{,\theta} \sin^2 \theta \quad (3.30)$$

The next step is to derive an explicit expression for the perturbed magnetic field δB^μ , Using the linearized induction equations (3.15), together with the relations (3.16) - (3.18), we obtain the first time derivative of the quantity δB_μ :

$$\delta B^t_{,t} = e^{-\Phi} B^\phi \delta u_{\phi,t}, \quad (3.31)$$

$$\delta B^r_{,t} = e^{-\Phi} B^r_{,\phi} \delta u^\phi, \quad (3.32)$$

$$\delta B^\theta_{,t} = e^{-\Phi} B^\theta_{,\phi} \delta u^\phi, \quad (3.33)$$

$$\delta B^\phi_{,t} = e^\Phi \left[(\Phi_{,r} B^r - B^\phi_{,\phi}) \delta u^\phi + B^r \delta u^\phi_{,r} + B^\theta \delta u^\phi_{,\theta} \right]. \quad (3.34)$$

Because the perturbed four velocity δu_ϕ depends on the time, (through the time derivative of the stellar displacement $\mathcal{Y}(r, \theta)$, see equation (3.18)), we can then integrate equations (3.31)-(3.34) in time and obtain an expression for δB^μ . thus, we finally get:

$$\delta B^t = e^{-2\Phi} B^\phi \mathcal{Y}(r, \theta), \quad (3.35)$$

$$\delta B^r = e^{-2\Phi} B^r_{,\phi} \mathcal{Y}(r, \theta), \quad (3.36)$$

$$\delta B^\theta = e^{-2\Phi} B^\theta_{,\phi} \mathcal{Y}(r, \theta), \quad (3.37)$$

$$\delta B^\phi = \left[(\Phi_{,r} B^r - B^\phi_{,\phi}) \mathcal{Y}(r, \theta) + B^r \partial_r \mathcal{Y}(r, \theta) + B^\theta \partial_\theta \mathcal{Y}(r, \theta) \right]. \quad (3.38)$$

The next step is to substitute in the linearized equations of motion (3.13), the first time derivative of δB^μ , obtained in equations (3.35)-(3.36), and the expressions of the stress energy tensor (3.29) and (3.30). We get a unique equation given by:

$$\begin{aligned} & -[16\pi^2(\rho + P) + B^2 - (B^\phi r \sin \theta)^2] \mathcal{Y}_{,tt} = (B^\theta)^2 \mathcal{Y}_{,\theta\theta} + 2B^r B^\theta \mathcal{Y}_{,\theta r} + (B^r)^2 \mathcal{Y}_{,rr} \\ & + \left[2 \cot \theta B^r B^\theta + \left(\Phi_{,r} + \frac{2}{r} \right) (B^r)^2 + B^r B^r_{,r} + B^\theta B^r_{,\theta} \right] \mathcal{Y}_{,r} \\ & + \left[2 \cot \theta (B^\theta)^2 + \left(\Phi_{,r} + \frac{2}{r} \right) B^r B^\theta + B^r B^\theta_{,r} + B^\theta B^\theta_{,\theta} \right] \mathcal{Y}_{,\theta} \\ & + e^{-2\Lambda} \mu \mathcal{Y}_{,rr} + \left[\left(\frac{4}{r} + \Phi_{,r} - \Lambda_{,r} \right) \mu + \mu_{,r} \right] e^{-2\Lambda} \mathcal{Y}_{,r} - \frac{\mu}{r^2} \mathcal{Y}_{,\theta\theta} \\ & + 3 \cot^2 \theta \mu \mathcal{Y}_{,\theta} \end{aligned} \quad (3.39)$$

CHAPTER 3. MAGNETIC OSCILLATIONS EQUATION

Since we study just axisymmetric perturbations, all physical quantities are independent from ϕ , thus the derivatives with respect to ϕ are all equal to zero.

The equation (3.39) is a second order partial differential equation in time and space. It can be rewritten also as:

$$A_{tt} \frac{\partial^2 \mathcal{Y}}{\partial t^2} = A_{20} \frac{\partial^2 \mathcal{Y}}{\partial r^2} + A_{11} \frac{\partial^2 \mathcal{Y}}{\partial r \partial \theta} + A_{02} \frac{\partial^2 \mathcal{Y}}{\partial \theta^2} + A_{10} \frac{\partial \mathcal{Y}}{\partial r} + A_{01} \frac{\partial \mathcal{Y}}{\partial \theta} \quad (3.40)$$

All the coefficients $A_{tt}, A_{20}, A_{11}, A_{02}, A_{10}$ and A_{01} depend on the coordinates r and θ but not on time. They have the following form:

$$A_{tt} = \left[\rho + \rho + \frac{a_1^2}{\pi r^4} \cos^2 \theta + \frac{a_1'^2}{4\pi r^4} e^{-2\Lambda} \sin^2 \theta \right] e^{-2(\Phi-\Lambda)}, \quad (3.41)$$

$$A_{20} = \frac{a_1^2}{\pi r^4} \cos^2 \theta + \mu, \quad (3.42)$$

$$A_{11} = -\frac{a_1 a_1'}{\pi r^4} \cos \theta \sin \theta, \quad (3.43)$$

$$A_{02} = \frac{a_1'^2}{4\pi r^4} \sin^2 \theta + \frac{\mu}{r^2} e^{2\Lambda}, \quad (3.44)$$

$$A_{10} = (\Phi' - \Lambda') \frac{a_1^2}{\pi r^4} \cos^2 \theta \quad (3.45)$$

$$+ \frac{a_1 a_1'}{2\pi r^4} \sin^2 \theta + \left[\mu' + \mu \left(\frac{4}{r} - \Lambda' + \Phi' \right) \right],$$

$$A_{01} = \left[\frac{a_1}{\pi r^4} \left(2\pi j_1 - \frac{a_1}{r^2} \right) e^{2\Lambda} \quad (3.46)$$

$$+ 3 \frac{a_1'^2}{4\pi r^4} \right] \sin \theta \cos \theta + \frac{3}{r^2} \mu \cot \theta e^{2\Lambda},$$

where we make use of the explicit form of the magnetic field B^μ given in equation (2.89). We recall that $a_1(r)$ and $j_1(r)$ are the radial components of, respectively, the electromagnetic four-potential and the four-current. In the above equations, the prime indicates the derivative with respect the radius.

The equation (3.40) must be solved with the appropriate boundary conditions. Those condition are given by (see [29]):

- regularity at the center: $\mathcal{Y} = 0$ for $r = 0$,
- no traction on the surface: $\mathcal{Y}_{,r} = 0$ at $r = R$,
- axisymmetry at $\theta = 0$: $\mathcal{Y}_{,\theta} = 0$,

-
- equatorial plane symmetry $\mathcal{Y} = 0$ for $\ell = 3$ initial data at $\theta = \pi/2$,
 - for $\ell = 2$ initial data: $\mathcal{Y}_{,\theta} = 0$ at $\theta = \pi/2$.

3.1.1 Crustal fields vs global fields

Equation (3.40) was first derived by Sotani et al. in [24]. In this paper, the authors simplify that equation, using an expansion in Legendre Polynomials and neglecting the higher order coupling terms induced by the magnetic field, i.e the terms with harmonics indices $\ell \pm 2$. In this way, they obtain an one dimensional equation that they study extensively for each value of ℓ and for different overtones. They used a variety of samples of different stellar models, varying the EOS, the mass, the density and the crust thickness of the star. They find that the torsional stellar oscillations are influenced by the presence of a dipole magnetic field greater than $B = 10^{15}\text{G}$. In another paper [29], the same authors implement the equation (3.40) without operating an expansion in Legendre Polynomials but instead using a two-dimensional simulation. They find that the oscillation spectrum is continuum, according to the suggestion by Levin [28]. However, in both the papers [24] and [29], the only configuration of magnetic field used was a dipole magnetic field that permeates all the star.

In an extension of these papers, [32], we implement the equation (3.40) for different configurations of the magnetic field and confront our results with the observed data, in order to check if it was possible to disentangle among different configurations of magnetic field, looking for the one that better fit the observed data. In [32], then, we investigated two different configurations of the magnetic field: a magnetic field, with both a poloidal and a toroidal components, that permeates all the star (we will call it ‘global’ field, see left panel of Figure 3.1), and a magnetic field, also with both poloidal and toroidal components, that its confined just in the crust (we will call this configuration ‘crustal’ field, see right panel of Figure 3.1). The choice of these two particular configurations is motivated by some observational suggestions by Aguilera et al.[54] and by Braithwaite & Spruit [55]. In both the papers, the magnetic field evolution is studied in detail. In [55], the authors study the evolution of the magnetic field, with particularly attention to its stability. They found that a magnetic field with both poloidal and toroidal components doesn’t fall in an unstable configuration. Aguilera et al.[54], instead, study the impact on the thermal evolution of the stellar surface of a magnetic field confined in the crust, with both a toroidal and a poloidal component. Their aim is to explain the observed thermal spectra of magnetars, with particular attention to the sensitively hot spots observed on the

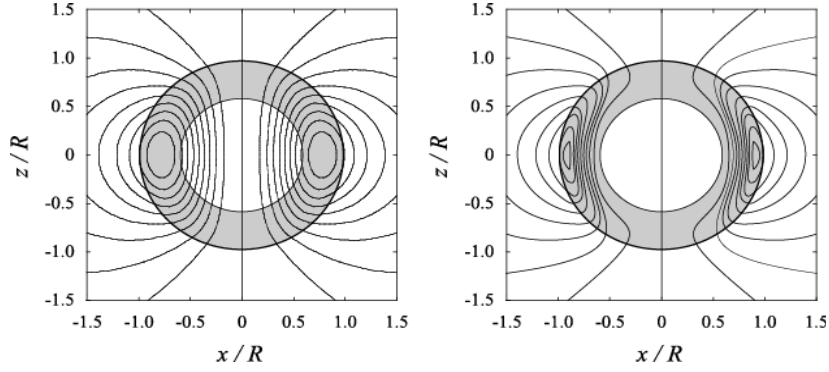


Figure 3.1: *Left panel*: Global magnetic field. *Right panel*: crustal magnetic field

surface of highly magnetised neutron stars: these spots are surface region that are hotter than their surrounding area. They could be heated by the magnetic field, as it evolves and decades, accumulating a lot of its energy in some preferred area, that the authors show to be the polar caps for a dipole magnetic field and the equator for a toroidal magnetic field. For these reasons we choose to investigate both the ‘global’ field and ‘crustal’ field. Note that, in the latter case, the core of the star is a superconductor of type I: this type of superconductors expels completely the magnetic field from its interior via Meissner effect, so no residual magnetic field, neither toroidal neither poloidal, is left there. In this way, the oscillations are confined inside the crust, and the equation (3.40) must be implemented just there.

To stabilise the equation (3.40) an artificial viscosity (implemented as a four derivative term) is needed to be added in the code. The reason for the needing of such artificial viscosity will be explained in the next section. Observing the Figure 3.1, it is evident that in the case of the crustal magnetic field, the magnetic field lines are denser than in the global field case. In fact, while in the ‘global’ field case the magnetic field can permeate all the star, in the ‘crustal’ field the magnetic field lines are confined in a layer of few kilometres (the crust): in this latter configuration is then obvious to expect denser magnetic field lines for the same magnetic field strength on the pole.

The absence of magnetic fields inside the core implies that no Alfvén modes are present in the core. So the lowest mode that it is found, is the crustal mode for $\ell = 2$. The fundamental crustal mode is inversely proportional to the radius of the star, as was found by Schumaker & Thorne [52], and its expression is given by:

$$f_{\ell}^{\text{crust}} = \sqrt{\ell(\ell + 1)} \frac{v_s}{2\pi R} \quad (3.47)$$

where R is the radius inside where the magnetic field is confined and v_s is the shear velocity, that it is considered constant at the crust density and can be set as $v_s = 10^8$ cm/s. The relativistic form of equation (3.48) was found by Samuelsson & Andersson [23] and has the form:

$$f_\ell^{\text{crust}} = \sqrt{(\ell + 2)(\ell - 1)} \frac{v_s}{2\pi R} \quad (3.48)$$

In the case of the crustal field, R is really thin, just 1 Km, and so the fundamental crustal frequency will increase considerably. In fact, its value was found to be around 40Hz for a magnetic field $B = 8 \times 10^{14}$ Gauss, see Figure 3.2, where a 2D simulation study (as the one performed in [29]), represented by the dot, is compared to a truncated calculation, obtained by expanding the equation (3.40) in Legendre Polynomials and truncating it, excluding the $(\ell \pm 2)$ coupling (see [24] for more details). In Figure 3.2, the frequencies are plotted against the magnetic field strength: it is evident that for a magnetic field $B/B_\mu \simeq 0.04$ (where $B_\mu = 4 \times 10^{15}$ Gauss) the lower torsional frequency starts to increase rapidly. For the lower limit of the magnetic field in SGR1806-20 and SGR 1900+14 (respectively $B = 8 \times 10^{14}$ G and $B = 4 \times 10^{14}$ G, as it is represented by the vertical lines), the lower crustal frequency is around 30Hz or even higher in the case of SGR 1806-20. This means that a magnetic field confined in the crust cannot explain the lower frequencies observed in SGRs, that are at 18Hz, 26Hz and 29Hz.

Since the first frequency observed in both SGR 1806-20 and SGR 1900+14 is below 20Hz, crustal fields cannot explain the observed data. Our results agree with the suggestions made by Glampedakis et al. [25] and by Levin [27], for the need of global modes in explaining magnetars QPOs.

For this reason, in the following, we will consider just global fields.

3.2 A new transformation of coordinates

The equation (3.40) was already studied in [24]. We found that such equation cannot be evolved in a stable way for a long time and so they needed to add an artificial fourth order dissipation term in order to avoid the numerical instability. The origin of this instability is due to a singular mathematical behaviour of the equation (3.40). To show this, we neglect, as first approximation, the first derivatives in the direction of r and θ in the equation (3.40). Then only the coefficients A_{20} , A_{11} and A_{02} remain. A calculation of the determinant D of the principal part of the equation (3.40) leads to:

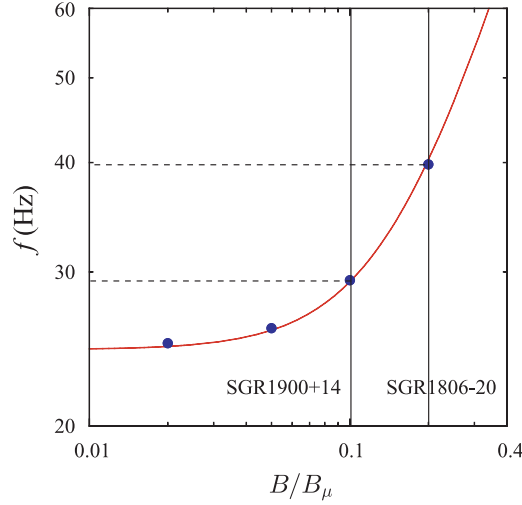


Figure 3.2: The torsional mode oscillations as a function of the strength of the magnetic field. The dots correspond to the results of a 2D simulations while the continuous line is the result of a truncate calculation on which the equation (3.40) was expanded in Legendre Polynomials and the $(\ell \pm 2)$ coupling is neglected. The two vertical lines correspond to the estimated lower limit of magnetic field for SGR 1900+14 and SGR 1806-20 (respectively $B = 4 \times 10^{14}$ G and $B = 8 \times 10^{14}$ G).

$$\begin{aligned}
 D &\equiv A_{20}A_{02} - \left(\frac{A_{11}}{2}\right)^2 \\
 &= \frac{a_1^2 a_1'^2}{4\pi^2 r^8} \cos^2 \theta \sin^2 \theta - \frac{a_1^2 a_1'^2}{4\pi^2 r^8} \cos^2 \theta \sin^2 \theta = 0.
 \end{aligned} \tag{3.49}$$

Hence the equation is parabolic in every point of its domain and therefore does not describe propagation of 2D waves.

To avoid this pathological behaviour, we introduce a new coordinate system given by the transformation

$$X = \sqrt{a_1} \sin \theta \quad Y = \sqrt{a_1} \cos \theta. \tag{3.50}$$

This new coordinates system is a kind of Cartesian coordinate system where, instead of the radial coordinate r , we use the radial component of the magnetic

field, $a_1(r)$. The behavior of a_1 inside the star is determined via the equation (2.96). On the surface, we require the continuity of a_1 with the dipole solution outside given in equation (2.101).

Using the new coordinates (3.50), the equation (3.40) is transformed in:

$$A_{tt} \frac{\partial^2 \mathcal{Y}}{\partial t^2} = \bar{A}_{20} \frac{\partial^2 \mathcal{Y}}{\partial X^2} + \bar{A}_{11} \frac{\partial^2 \mathcal{Y}}{\partial Y \partial X} + \bar{A}_{02} \frac{\partial^2 \mathcal{Y}}{\partial Y^2} + \bar{A}_{01} \frac{\partial \mathcal{Y}}{\partial Y} + \bar{A}_{10} \frac{\partial \mathcal{Y}}{\partial X}, \quad (3.51)$$

where

$$\bar{A}_{02} = \frac{1}{4\pi r^4} a_1 a_1'^2 + \mu \pi r^2 \left(\frac{a_1'^2}{4a_1} \cos^2 \theta + a_1 e^\Lambda \sin^2 \theta \right) \quad (3.52)$$

$$\bar{A}_{20} = \mu \pi r^4 \left(\frac{a_1'^2}{4a_1} \sin^2 \theta + \frac{a_1 e^\Lambda \cos^2 \theta}{r^2} \right) \quad (3.53)$$

$$\bar{A}_{11} = \mu \pi r^4 \left(\frac{a_1'^2}{2a_1} - 2 \frac{a_1 e^\Lambda}{r^2} \right) \sin \theta \cos \theta \quad (3.54)$$

$$\bar{A}_{01} = \frac{X}{2\pi r^4} a_1 \left(\frac{2}{r^2} a_1 e^{2\Lambda} - 4\pi j_1 e^{2\Lambda} - \frac{a_1'^2}{2} \right) \quad (3.55)$$

$$+ \mu' \frac{a_1'^2}{2\sqrt{a_1}} \quad (3.56)$$

$$+ \frac{\mu \pi r^4}{\sqrt{a_1}} \left(\frac{a_1'^2}{a_1} - 2 \frac{a_1}{r} - \frac{a_1 e^\Lambda}{r^2} - 2\pi J_1 \right) \cos \theta \quad (3.57)$$

$$\bar{A}_{10} = \left[\frac{\mu}{\sqrt{a_1}} \left(-\frac{a_1'^2}{4a_1} + 2 \frac{a_1'}{r} - 2\pi J_1 \right) \sin \theta \right. \quad (3.58)$$

$$\left. - 3\mu \sqrt{a_1} e^\Lambda \frac{\cos \theta}{r^2} + \mu' \frac{a_1'^2}{2\sqrt{a_1}} \cos \theta \right] \pi r^4 \quad (3.59)$$

The equation (3.51) doesn't show a pathological behaviour and can be evolved in a stable way for long time with the appropriate boundary conditions, listed at the end of section (3.1).

In the (X,Y) coordinates those conditions translate to:

- regularity at the center: $\mathcal{Y}(X, Y) = 0$ for $X = 0$ and $Y = 0$,
- no traction on the surface for the open lines:

$$\left[X \frac{\partial \mathcal{Y}}{\partial X} + Y \frac{\partial \mathcal{Y}}{\partial Y} \right] = 0; \quad (3.60)$$

- axisymmetry at $X = 0$:

$$Y \frac{\partial \mathcal{Y}}{\partial X} = 0; \quad (3.61)$$

- equatorial plane symmetry for $\ell = 3$ initial data at $Y = 0$:

$$Y \frac{\partial \mathcal{Y}}{\partial X} = 0; \quad (3.62)$$

- equatorial plane symmetry for $\ell = 2$ initial data: $\mathcal{Y}(X, Y) = 0$ at $Y = 0$.

An important task, that we will discuss in the next chapters, is what is the condition to require at the crust-core interface. This condition depends strongly on the structure of stellar model we consider: a fluid star, without crust, will require just the continuity of the stellar displacement \mathcal{Y} on the crust-core interface, while the presence of a solid crust will require that the radial derivative of the stellar displacement must be continuous, leading to a coupling between crust and core. In the next two chapters, we will study both configurations.

3.2.1 Open and close magnetic field lines

The construction of the grid in the new (X, Y) coordinates needs special attention. The function a_1 has a maximum inside the star (see Figure 2.2) and the position of this maximum inside the star depends on the strength and the topology of the magnetic field. A strong magnetic field, as well as a toroidal field added to the standard poloidal field, pushes the maximum near the surface of the star. The position of $a_{1 \max}$ determines also the presence or not of the closed magnetic field lines confined inside the star: if $a_{1 \max}$ is really near the surface, then we will not have any closed magnetic field lines, i.e. magnetic field lines that confine themselves in the interior of the star forming close loops, and never reaching the surface (see Figure 2.1). For this reason, they are subject to different boundary conditions than the open magnetic field lines, that instead reach the surface and match with the dipole magnetic field outside the star. This difference leads to a different behaviour of the oscillations of open and close magnetic lines, as it will be shown later. We note also that closed and the open magnetic lines don't interact with each other. For this reason, in our code, we split the problem into two parts, one for the closed and one for the open magnetic field lines. For the open magnetic field lines, the perturbation function $\mathcal{Y}(X, Y)$ is evolved until some points X_{\max} and Y_{\max} that correspond to the maximum of $a_{1 \max}$ i.e we work on the part A of Figure 3.3. Then the evolution continues, in the part A' of Figure 3.3, from the points X_{\max} and Y_{\max} and ends at the points X_{surf} and Y_{surf} that

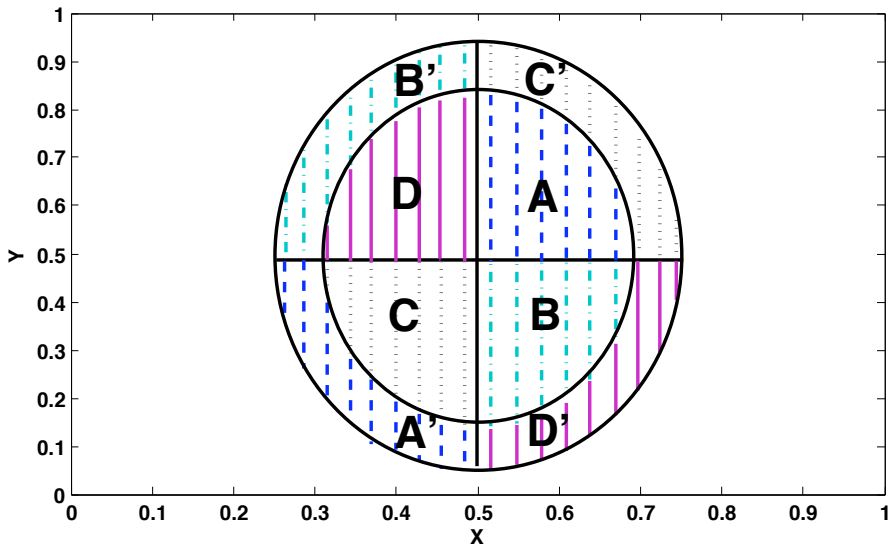


Figure 3.3: Plot of the magnetic field lines in the (X, Y) coordinates. Note that, after the point $X(a_{1 \max})$ and $Y(a_{1 \max})$ lines of the same color continue in different quadrants: for example, the lines of the domain A continue to the domain A' .

correspond to the surface of the star. Note that in this second part we have to use the transformation

$$X = -\sqrt{a_1} \sin \theta \quad Y = -\sqrt{a_1} \cos \theta \quad (3.63)$$

due to the sign change of the derivative of a_1 .

In a similar fashion for the closed magnetic lines, we evolve $\mathcal{Y}(X, Y)$ up to X_{\max} and Y_{\max} , but then the simulation doesn't end on the surface but at X_{eq} and Y_{eq} , that correspond to points on the equator, since this type of magnetic field lines do not reach the surface but instead close themselves on the equator.

From a technical point of view, the transformation that we have just described “*open*” the field lines: when the field lines reach the point where the function a_1 has a maximum, the transformation (3.63) must be used. We evolve the oscillation of the part before X_{\max} and Y_{\max} and the part after these points as two separate problems. Then, we match them in each time step via the bound-

CHAPTER 3. MAGNETIC OSCILLATIONS EQUATION

ary conditions. This procedure will be explained later. Figure 3.3 may help in understanding the procedure followed in solving this problem.

4

Global torsional oscillations

In this chapter, we study in the (X, Y) coordinates the linear equation derived in chapter 3 for a non-rotating relativistic neutron star, endowed within a strong magnetic field. For example, at the surface we set $B_{\text{surf}} = 4 \times 10^{15}$ Gauss. We study two types of magnetic field: a purely poloidal magnetic field (where the constant ζ in equation (2.96) is set to zero) and a mixed configuration, where both poloidal and toroidal magnetic field are present.

The star is assumed to be composed by a normal fluid, and we don't take into account the presence of a crust. We don't include superfluidity, as first approximation, although it is thought that superfluidity could influence neutron star oscillations [56]. It is, in any case, a hard task to predict and model how a strong magnetic field influences the microscopic property of neutron star matter. For this reason, we will concentrate on the macroscopic effects that a strong magnetic field produce, studying carefully the QPOs introduced by the presence of a magnetic field.

We relate our results with the present observed data for QPOs in SGR 1806-20 and SGR 1900+14.

4.1 Equation for the fluid star

For a star mode out of a fluid, without crust, since the shear viscosity μ is vanishing, the coefficients A_{20} , A_{11} and A_{10} are equal to zero (see equations (3.42), (3.43) and (3.45)). The equation (3.51) is then reduce to a 1+1 time evolution equation, given by

$$A_{tt} \frac{\partial^2 \mathcal{Y}}{\partial t^2} = \tilde{A}_{02} \frac{\partial^2 \mathcal{Y}}{\partial Y^2} + \tilde{A}_{01} \frac{\partial \mathcal{Y}}{\partial Y}, \quad (4.1)$$

where

$$\tilde{A}_{02} = \frac{1}{4\pi r^4} a_1 a_1'^2 \quad (4.2)$$

$$\tilde{A}_{01} = \frac{X}{2\pi r^4} a_1 \left(\frac{2}{r^2} a_1 e^{2\Lambda} - 4\pi j_1 e^{2\Lambda} - \frac{a_1'^2}{2} \right). \quad (4.3)$$

This equation describes waves propagating along the Y direction and it reminds waves propagating on the strings of a musical instrument, e.g. a piano. When we switch the sign of our coordinates after the maximum of a_1 (see equation (3.63)), the continuity of the function must be required:

$$\mathcal{Y}'_+ = \mathcal{Y}'_- \quad (4.4)$$

which in the (X, Y) coordinates, translates in:

$$\left[X \frac{\partial \mathcal{Y}}{\partial X} + Y \frac{\partial \mathcal{Y}}{\partial Y} \right]_- = \left[X \frac{\partial \mathcal{Y}}{\partial X} + Y \frac{\partial \mathcal{Y}}{\partial Y} \right]_+. \quad (4.5)$$

4.1.1 Crank-Nicholson scheme

We evolve equation (4.1) by using an explicit Crank-Nicholson scheme. In general, the Crank-Nicholson scheme is an implicit scheme that ensures accuracy but not speed. Its explicit variation can be implemented easily and guarantees second order accuracy both in space and in time. Actually, in ([57]), the author demonstrates that such a scheme exhibits an oscillatory convergence, becoming stable after exactly two iterations. Performing additional iterations, it does not improve neither the convergence or the accuracy. Since the scheme converges with only two iterations, the computation time is considerably reduced. To show this advantage, we consider a simple wave equation:

$$\frac{\partial u}{\partial t} = \frac{\partial u}{\partial x}. \quad (4.6)$$

Using a first-order accurate differencing forward in time and centered in space scheme, we get:

$$\frac{u_j^{n+1} - u_j^n}{\Delta t} = \frac{u_{j+1}^n - u_{j-1}^n}{2\Delta x}. \quad (4.7)$$

This scheme is known to be unstable. It is possible to make the system stable, by using an intermediate variable \tilde{u} and calculating:

$$\frac{\tilde{u}_j^{n+1} - u_j^n}{\Delta t} = \frac{u_{j+1}^n - u_{j-1}^n}{2\Delta x}. \quad (4.8)$$

Then, by averaging we get:

$$\bar{u}_j^{n+1/2} = \frac{1}{2}(\tilde{u}_j^{n+1} + u_j^n). \quad (4.9)$$

The second iteration is performed, following the step (4.8) and (4.9), but for $\bar{u}_j^{n+1/2}$, i.e. :

$$\frac{\tilde{u}_j^{n+1} - u_j^n}{\Delta t} = \frac{\bar{u}_{j+1}^{n+1/2} - \bar{u}_{j-1}^{n+1/2}}{2\Delta x} \quad (4.10)$$

and

$$\bar{u}_j^{n+1/2} = \frac{1}{2}(\tilde{u}_j^{n+1} + u_j^n) \quad (4.11)$$

Using \bar{u} in the right side of equation (4.7), we finally get:

$$\frac{u_j^{n+1} - u_j^n}{\Delta t} = \frac{\bar{u}_{j+1}^{n+1/2} - \bar{u}_{j-1}^{n+1/2}}{2\Delta x}. \quad (4.12)$$

The stability of this procedure can be studied by putting:

$$u_j^n = \xi^n e^{ikj\Delta x} \quad (4.13)$$

where ξ is the amplification factor given by:

$$\xi = 1 + 2i\beta \quad (4.14)$$

with $\beta = [\Delta t/(2\Delta x)](\sin k\Delta x)$. The amplification factor is given by:

$${}^{(0)}\xi = 1 + 2i\beta \quad (4.15)$$

$${}^{(1)}\xi = 1 + 2i\beta - 2\beta^2 \quad (4.16)$$

$${}^{(2)}\xi = 1 + 2i\beta - 2\beta^2 - 2i\beta^3 \quad (4.17)$$

$${}^{(3)}\xi = 1 + 2\iota\beta - 2\beta^2 - 2\iota\beta^3 + 2\beta^4 \quad (4.18)$$

and so on. To check the stability, one must calculate the behaviour of the square modulus of the amplification factor $|\xi^2|$ for each of the equations above. It results that equations (4.15) and (4.18) are unstable while equations (4.16) and (4.17) are stable if $\beta^2 \leq 1$. This means that for each wave numbers k , we must have $\Delta t \leq 2\Delta x$. In order to study the convenience of the scheme, we must analyse its accuracy and its convergence. While the amplification factor does converge to 1 as the number of iterations increases, the convergence is not monotonic but has an oscillatory behaviour, i.e. it oscillates below and above 1 during the iterations. All the case where the amplification factor takes values above 1 are unstable. On the contrary, the accuracy of the scheme is determined by its truncation error. This error is of the second order in Δt and Δx from the first iteration on. This means that doing more iterations changes the oscillatory behaviour but not the accuracy of the scheme. Since the scheme converges after the first two iterations, there are no advantages to perform more than two iterations.

4.2 Numerical implementation

We consider first a fluid star with a purely dipole magnetic field both inside and outside the star. The magnetic field strength is set to $B_{\text{surf}} = 4 \times 10^{15}$ Gauss on the stellar pole.

We construct a numerical equidistant grid 90×90 in the (X, Y) coordinates, setting $X_{\text{max}} = \sqrt{a_{1 \text{ max}}} \sin \theta$ and $Y_{\text{max}} = \sqrt{a_{1 \text{ max}}} \cos \theta$ and varying θ from 0 to $\pi/2$. The structure of our grid is displayed in the first quadrant of Figure 3.3. Note that each ‘magnetic string’ in the first quadrant continues in the third one. For example, a ‘magnetic string’ in quadrant A will continue in quadrant A_1 , due to the change of sign in the radial component of the magnetic field a_1 derivative. We evolve in time these two parts like two separate problems, and link them in every time step, requiring the continuity of the function \mathcal{Y} and its derivative \mathcal{Y}' . We let an open magnetic field line to interact with the two nearest open magnetic field lines on the stellar surface, as required by the boundary condition (3.60). On the contrary, we don’t let open and closed magnetic field lines to interact to each other, because the closed magnetic lines don’t reach the surface and so they cannot connect with the open magnetic lines. For our evolution, we use an iterative Crank-Nicholson scheme ([57]), as explained in section 4.1.1.

Using this scheme, we evolve the perturbations for more than 1s. In order to check the stability of the system, we performed even evolutions for 2s and

found that our scheme was still stable. As results of the time evolution, we obtain for each ‘magnetic string’ a value of the first time derivative of the stellar displacement \mathcal{Y} . We compute the FFT of this value on various ‘strings’ and find that each ‘string’ corresponds to a different frequency. We compare these frequencies with the ones present in literature.

In [29], the authors find a family of upper frequencies near the magnetic axis for $\theta = 0$, corresponding to points along the Y-axis in our coordinates, and a family of lower frequencies for $\theta = \pi/2$, corresponding to points along the X-axis in our coordinates. They identify the fundamental frequency peaks of the two families of QPOs with the edges or turning points of the Alfvén continua suggested by [28]. These two frequencies were named fundamental lower L_0 , for $\theta = \pi/2$, and fundamental upper U_0 , for $\theta = 0$ QPOs. The overtones are indicated by L_n and U_n . In the following, we adopt these symbolism when we refer to the oscillations of the open field lines, while we call the frequencies of the close field lines C_n .

Our results confirm partially the results of [29] but add also some new features. For open lines, a family of upper frequencies appears near the Y-axis while a family of lower frequencies appears near the last open magnetic field line, just at the edge with the region of close lines.

This can be explained by the fact that the ‘strings’ near the Y-axis correspond to stronger magnetic field on average because in the (r, θ) coordinates they correspond to denser field lines, see Figure 2.1.

In fact, the frequency of the Alfvén oscillations is proportional to the strength of the magnetic field:

$$f = \frac{v_A}{L} = \frac{B}{\sqrt{4\pi\rho}} \frac{1}{L} \quad (4.19)$$

where $v_A = B/\sqrt{4\pi\rho}$ is the Alfvén velocity and L is the length on which the perturbation propagates. Since the magnetic field B is stronger near the magnetic axis, we expect that these frequencies are the upper ones. In addition, we find that, for all the ‘magnetic strings’, the upper frequencies are multiples of the fundamental frequency both in the case of L_n and in the case of U_n (see Figure 4.1). However, we find a different multiplicity respect on the one found in [29], depending if we consider even $\ell = 2$ or odd $\ell = 3$ initial data. This is new results was also confirmed in [58]. We obtain such relations between fundamental frequency and overtones:

$$f_{L_n^{\text{even}}} \simeq (2n + 1)f_{L_0} \quad (4.20)$$

$$f_{U_n^{\text{even}}} \simeq (2n + 1)f_{U_0} \quad (4.21)$$

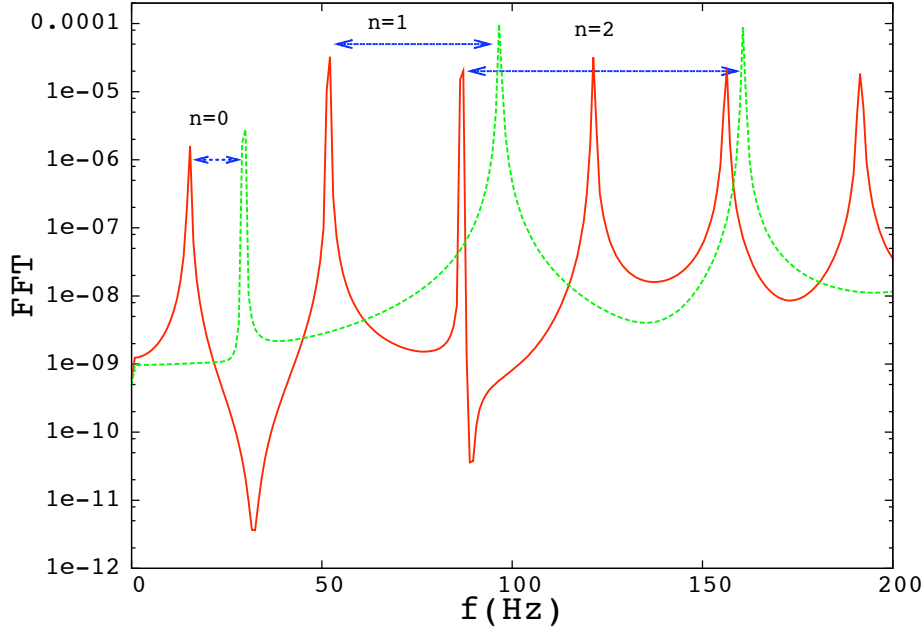


Figure 4.1: The FFT of a point near the Y-axis (green/dashed line) and near the critical point (red/continuous line) for open lines and even parity ($\ell = 2$). The stellar model is WFF_{14} .

$$f_{L_n^{\text{odd}}} \simeq (n+1)f_{L_0} \quad (4.22)$$

$$f_{U_n^{\text{odd}}} \simeq (n+1)f_{U_0} \quad (4.23)$$

where the superscripts *even* and *odd* indicate results derived for even ($\ell = 2$) and odd ($\ell = 3$) parity initial data and boundary conditions on the equator. The different scaling shown in the relations (4.20) - (4.21) and (4.22)-(4.23) is due to the different boundary conditions used for odd and even values of ℓ . The problem can be understood by looking at a simple problem like the one of two strings of finite length connected by another spring. If the two strings are coupled together at just one of their ends while the others are kept fixed, like in the case of even parity, where the ‘magnetic strings’ are coupled just near the surface and are fixed at the equator, then we obtain the relations (4.20) and (4.21). This type of configuration was analyzed in [50], in order to explain the w-modes of neutron stars. Actually, the analytic derivation of the relations (4.20) and (4.21)

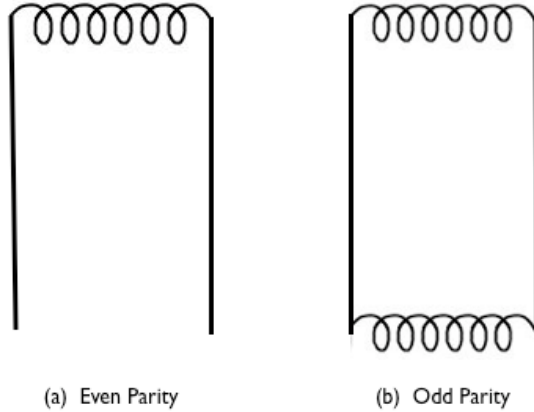


Figure 4.2: A schematic representation of the coupling between two adjacent magnetic ‘strings’ in the case of: (a) even parity condition at the equator, (b) odd parity condition at the equator.

can be found there. If instead the two strings are coupled in both ends (like in the case of odd parity) then the relations (4.22) - (4.23) follow. See Figure (4.2) for a schematic representation of the two types of coupling.

The frequencies of the closed magnetic field lines show a different behaviour: the upper and lower frequencies are scaling as (see also Figure 4.3):

$$f_{C_n} \simeq (n + 1)f_{C_0} \tag{4.24}$$

The difference between the relations (4.20) and (4.24) is due to the different boundary conditions: the closed lines never reach the surface. They actually begin from the equator where they also close. This means that they admit the same boundary condition at both their ends which resembles the toy problem of a string that oscillates with both ends fixed, that gives the $n + 1$ behaviour, as in the case odd values of ℓ for the open field lines. The frequencies that we find for close lines initially decrease up to a minimum and then increase. This behaviour results from two factors. First, from the fact that closes lines are shorter than the open lines (decreasing the length L in equation (4.19) a maximum frequency is reached), and, second, from the fact that the magnetic field becomes somehow locally weaker as we move off the axis (decreasing the magnetic field B in equation (4.19) a minimum frequency is reached). Our results are summarised in Table 4.1.

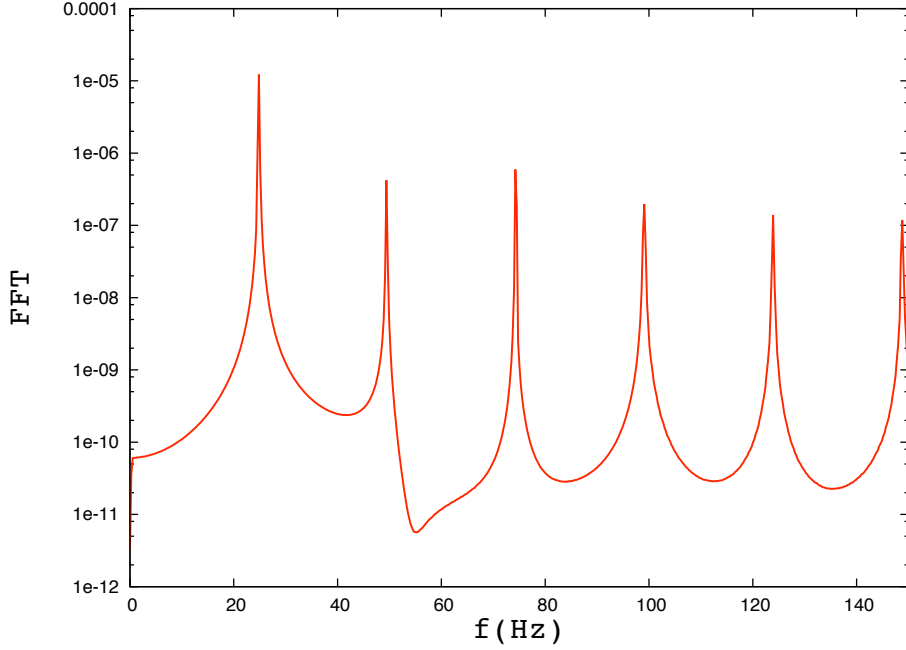


Figure 4.3: The FFT of a closed line near the critical point for the stellar equilibrium model WFF_{14} . It is worth noticing the spacing of the peaks in accordance to (4.24)

4.3 The effect of the toroidal field on the spectrum

We now study how the presence of a mixed field, both toroidal and poloidal, affects the spectrum of oscillations. According to equation (2.87) the toroidal magnetic field will be given by:

$$B_\phi = -\zeta e^{-\phi} a_1 \sin \theta , \quad (4.25)$$

where ζ is a constant only depending on the ratio between the toroidal and poloidal magnetic fields. By increasing or decreasing ζ , we can influence the strength of the toroidal magnetic field. So ζ can be interpreted as a parameter that describes the strength of the toroidal magnetic field with respect to the poloidal field, see [53] for details. The presence of a toroidal field modifies equation (2.96), by adding an extra term $\zeta^2 e^{-2\phi} a_1$ (see [32]). Thus, the Grad-

Table 4.1: Frequencies of Alfvén QPOs for representative sample of equilibrium models, constructed for different EOS and fixed magnetic field strength $B = 4 \times 10^{15}$ Gauss. The frequencies are computed for points near the critical point (L_n) and near the Y-axis (U_n) for open lines (both for even and odd parity) and for the close line (C_n).

Model	M/R	n	$f_{L_n^{\text{odd}}}(Hz)$	$f_{L_n^{\text{even}}}(Hz)$	$f_{U_n^{\text{odd}}}(Hz)$	$f_{U_n^{\text{even}}}(Hz)$	$f_{C_n}(Hz)$
WFF_{14}	0.189	0	23.00	46.56	28.05	58.90	23.56
		1	69.55	93.11	84.15	118.4	47.68
		2	116.1	139.1	144.3	178.5	70.11
WFF_{18}	0.264	0	13.46	27.48	16.27	33.09	14.02
		1	39.82	54.41	48.24	66.75	28.05
		2	67.31	81.89	80.21	99.84	42.06
APR_{14}	0.178	0	23.01	47.06	28.24	61.18	24.04
		1	70.60	95.17	86.28	121.8	74.78
		2	117.1	142.2	144.3	182.5	180.0
APR_{20}	0.269	0	12.53	25.06	15.25	31.60	13.07
		1	37.59	50.09	44.12	61.56	25.60
		2	62.10	74.63	74.63	92.61	38.13
L_{20}	0.198	0	13.10	27.83	16.78	35.61	13.52
		1	40.11	55.66	51.16	70.40	27.85
		2	68.35	83.50	85.54	105.6	41.34

Shafranov becomes:

$$a_1'' e^{-2\Lambda} + (\Phi + \Lambda)' e^{-2\Lambda} a_1' + \left(\zeta^2 e^{-2\Phi} - \frac{2}{r^2} \right) a_1 = -4\pi j_1 . \quad (4.26)$$

Even if a toroidal field is present, the magnetic field on the surface is always set to $B_{\text{surf}} = 4 \times 10^{15}$ Gauss. In fact, making this assumption, the toroidal and poloidal magnetic field adjust themselves inside the star, contributing both to the energetic magnetic balance: a presence of the toroidal field implies a decrease of the poloidal field energy, and such decrease is governed by the strength of the constant ζ in the equation (4.26): if ζ takes high values, then the poloidal magnetic field decreases significantly and the toroidal field contribute is significant

in the intensity of the surface magnetic field.

The influence of the toroidal fields on the evolution equation (4.1) is included implicitly in a_1'' . By solving equation (2.96) for a_1'' and subsequently substituting into equation (4.1), the toroidal magnetic field appears in the 1+1 equation (4.1) through the parameter ζ in the term:

$$\tilde{A}_{01} = \frac{X}{2} a_1 \left(\frac{2e^{2\Lambda} a_1}{r^2} - \zeta^2 a_1 e^{-2\Phi} - \frac{a_1'^2}{2} - 4\pi j_1 \right). \quad (4.27)$$

This means that the toroidal field affects the local propagation speed of the Alfvén modes.

The toroidal field has also another important effect in our problem: it pushes the position of $a_{1 \max}$ outwards and contributes to the stability of the magnetic field in the star. In Figure 4.4, we plot the function a_1 for the EOS WFF₁₄ and for different values of the parameter ζ . It is clear that when ζ increases, i.e., the strength of the toroidal magnetic field increases, then $a_{1 \max}$ is pushed closer to the surface.

Because our coordinates depend on the position and strength of $a_{1 \max}$, it is natural to expect changes in the oscillation spectrum due to the presence of the toroidal component of the magnetic field. We find that the Alfvén frequencies for both open and closed field lines are lower compared to the case in which only a dipole field was present, see Table 4.2, especially for the close magnetic ‘strings’. This can be explained by the presence of a toroidal magnetic field, which means that the point where the magnetic field line converges, moves outwards, hence the ‘magnetic strings’ becomes longer. Since the frequency is inversely proportional to the length of the ‘strings’, as the length increases, the frequency decreases see equation (4.19).

4.4 Identification of the QPOs frequencies

Strohmayer and Watts [21] have performed a timing analysis of the SGR 1806-20 and the SGR 1900+14. This study shows the appearance of several QPOs in the tail of these events. In particular, for SGR 1806-20, the identified frequencies are 18, 26, 30, 92, 150, 625 and 1840 Hz while for SGR 1900+14 the frequencies are 28, 53, 84 and 155 Hz.

Using the relations (4.22) and (4.23), we can easily show that for SGR 1900+14, if we consider $f_{U_0^{\text{odd}}} = 28\text{Hz}$, then we can identify $f_{U_1^{\text{odd}}} = 56\text{Hz}$, and $f_{U_2^{\text{odd}}} \simeq 84\text{Hz}$. In a similar way for SGR 1806-20, we have $f_{L_0^{\text{even}}} = 18\text{Hz}$ and

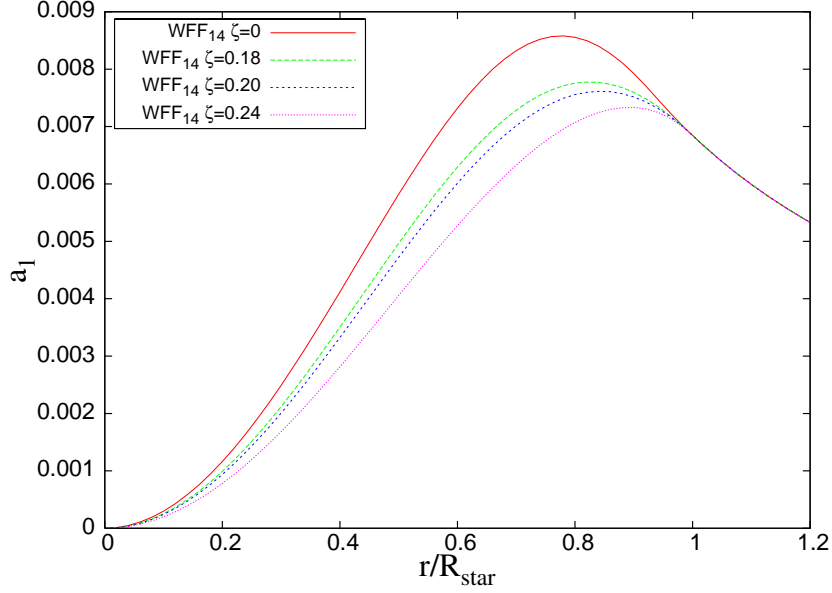


Figure 4.4: The function a_1 in function of the normalized coordinates r/R for an equilibrium model constructed with the equation of state WFF and a mass $M = 1.4M_\odot$. Different curves represent different value of the parameter ζ , i.e. different strength of the toroidal magnetic field.

$f_{L_0^{\text{odd}}} = 30\text{Hz}$, and consequently $f_{L_2^{\text{even}}} \simeq 92\text{Hz}$ (or $f_{L_2^{\text{odd}}} \simeq 92$), $f_{L_4^{\text{even}}} \simeq 150\text{Hz}$ (or $f_{L_4^{\text{odd}}} \simeq 150$). If we look at our results in the Tables 4.1 and 4.2, we can identify the QPOs in SGR 1900+14 with the lower frequencies for odd parity of a model with equation of state WFF and a mass around $1.8M_\odot$. For the QPOs from SGR 1806-20, we can fit the observative data by a model with equation of state APR, mass around $1.4M_\odot$ and a toroidal field a little stronger than the poloidal one ($\zeta = 0.18$).

Based on these results, it is clear that the presence of a toroidal field allows us to explain most of the lower frequencies. We argue that also a quadrupole field or other more complicated mixed magnetic field configuration, will lower

CHAPTER 4. GLOBAL TORSIONAL OSCILLATIONS

Table 4.2: Frequencies of Alfvén QPOs and their ratios for different stellar model with a toroidal component of the magnetic field and a surface magnetic field $B = 4 \times 10^{15}$ Gauss. For open magnetic ‘string’ the frequencies are taken for points near the critical point (L_n) and near the Y-axis (U_n), both for even and odd parity. We also give the value of the frequencies for the lower close magnetic ‘string’ (C_n).

Model	ζ (km^{-1})	n	$f_{L_n^{\text{odd}}}$ (Hz)	$f_{L_n^{\text{even}}}$ (Hz)	$f_{U_n^{\text{odd}}}$ (Hz)	$f_{U_n^{\text{even}}}$ (Hz)	f_{C_n} (Hz)
<i>WFF</i> ₁₄	0.24	0	15.15	30.30	16.24	33.94	15.76
		1	46.06	61.20	50.91	66.66	31.15
		2	75.75	90.90	81.20	99.99	79.38
<i>APR</i> ₁₄	0.18	0	18.95	38.46	22.85	49.6	19.51
		1	56.83	76.91	69.67	98.65	39.01
		2	95.30	114.8	117.0	147.7	57.96
<i>APR</i> ₁₄	0.20	0	16.21	32.42	19.35	41.84	16.73
		1	48.11	64.84	59.05	83.67	33.47
		2	64.84	97.79	99.88	125.5	51.25
<i>L</i> ₁₄	0.20	0	11.47	22.93	13.92	29.90	11.88
		1	34.40	45.46	42.18	58.57	23.75
		2	56.52	68.39	70.05	88.46	35.63

the frequencies, as the toroidal one does: that is due to the position of $a_{1 \max}$ that will be pushed outwards. In this case, as we already pointed out, the part with the closed lines occupy a smaller area in the star. One may ask how the presence of the closed lines can be detected, since they don’t reach the surface of the star and so they are not connected with the magnetosphere. As shown in some recent works [59], [60], the presence of closed lines could originate anisotropy in the surface temperature, heating the equator more than the stellar poles, and producing in this way a strong signature on the thermal spectrum, that could be easily detected by satellites as ROSAT or CHANDRA.

Even if the presence of a toroidal field can explain many of the lower frequencies, there are still some frequencies that we cannot explain, like for example the 26 Hz frequency in SGR 1806-20. This frequency is most probably associated with a pure crustal oscillation and since in our model we don’t consider the

presence of the crust, we cannot find it. This calls for the inclusion of the crust in our calculation in order to incorporate the effect of the crust and its coupling with the core, as it was already pointed out in [25], [28] and [26].

In the next chapter we will show that a model with a fluid core and a solid crust, coupling to each others through the appropriate boundary conditions, can explain all the observed frequencies. In addition, in this new model, interesting new features in the spectrum are emerging.

5

Coupled crust-core magneto-oscillations

The crust of a neutron star has a complex structure, not yet completely understood (see [61] and references in there). Especially, at the boundary with the core, the structure of the crust is still subject to hypothesis. The most credible one is that a solid lattice structure, although not perfectly crystalline, is formed by an array of positively charged nuclei. Those nuclei can become really heavy with the increasing density towards the core, until they touch each other and the crystalline structure dissolves in an uniform structure, called ‘nuclear pasta’ that can take different shapes: road-like (‘spaghetti’ pasta) or even slab-like (‘lasagna’ pasta) are formed when the density is extremely high, at the boundary between the crust and the core [62].

Going towards the surface of the star, the density decreases until a point where the neutrons form a fluid Fermi sea. Above the neutron density drip, at $\rho_{\text{drip}} \simeq 4.6 \times 10^{11} \text{ g cm}^{-3}$, a Fermi sea of relativistic electrons is responsible for the crustal pressure.

All those components, present in usual neutron stars, are deeply modified by the presence of a magnetic field, for details see [63]. Although it is difficult to understand completely what is going on for matter embedded in a strong magnetic field, and many questions are still without answers, it is clear that the crust is subject to a big stress produced by the magnetic pressure that could also break it. The magnetic pressure is increased during the evolution of the magnetic field: while the magnetic field evolves, in fact, magnetic stress can be built up,

CHAPTER 5. COUPLED CRUST-CORE MAGNETO-OSCILLATIONS

through a diffusion of the magnetic field and the consequent instability of this latter.

There are essentially two ways in which the magnetic field can diffuse: by ambipolar diffusion in the liquid core and by Hall drift in the solid crust (see [64]). The ambipolar diffusion is a drift of the magnetic field and the charged particles relative to the neutrons. Due to the presence of ambipolar diffusion, the magnetic energy decreases and the magnetic field decays. For strong magnetic field, $B > 10^{14}$ Gauss, the ambipolar decay time is $\tau_{\text{amb}} \simeq 10^3 - 10^4$ years, in agreement with the present estimates of the magnetar age.

The Hall drift is a drift of the magnetic fluxes respect to the currents constituted by the electrons. The Hall effect is not acting to dissipate magnetic field: during the Hall drift, the magnetic energy is conserved. To explain this, in [65] it was shown how the Hall drift creates small scale magnetic field, using the energy of the large scale magnetic field: in this way, the magnetic energy is never completely lost. In addition, those small scale magnetic fields could generate also current sheets, if the star is stratified. Both ambipolar and Hall drift build up a magnetic stress respectively on the interface crust-core and on the upper part of the crust, just near the surface. The effects of this stress can be dramatically when the magnetic field is so strong as in magnetars, leading to the crust's breaking.

In fact, the soft gamma repeaters are strongly connected to the stress that the magnetic pressure applies to the crust. It is thought that the breaking of the crust could release an energy as big as the one releases by a giant flare in a SGR. This energy and the subsequent stress $S(B)$ can be calculated, using the magnetic pressure [13]:

$$S(B) \simeq \frac{B^2}{8\pi} = 7 \times 10^{29} \left(\frac{B}{4 \times 10^{15}} \right)^2 g \text{ cm}^{-1} \text{ s}^{-2}. \quad (5.1)$$

The maximal stress that the crust can bear before yielding is:

$$S_{\text{max}} = \frac{l}{R} \mu \theta_{\text{max}} \sim 3 \times 10^{26} \left(\frac{\theta_{\text{max}}}{10^{-2}} \right) \left(\frac{l}{10^5 \text{ cm}} \right) g \text{ cm}^{-1} \text{ s}^{-2} \quad (5.2)$$

where $l \sim 10^5$ cm is the thickness of the crust, μ is the shear modulus that can be calculated from the shear velocity v_s [52]:

$$v_s = 10^8 \left(\frac{\mu}{\rho} \right)^{1/2} \text{ cm s}^{-1}. \quad (5.3)$$

In equation (5.1) and in equation (5.2), θ is a dimensionless parameter that measures the change in length per unit of length under tension or compression.

This parameter is poorly known, it is possible to put some constraints on it, so that the value of θ are estimated to be:

$$10^{-5} \lesssim \theta \lesssim 10^{-2} \quad (5.4)$$

where the minimum value θ_{\min} can be obtained from experiments in laboratory on stress of Coulomb lattices, while the maximum value θ_{\max} can be inferred by Vela glitches. Recently, in a paper by Horowitz & Kadau [66], a dynamical simulation of maximal strength that could be sustained by a Coulomb lattice, finds out that the lattice seems to be more resistant as thought before and that θ_{\max} could be reach also $\theta_{\max} = 10^{-1}$. However, even if we use this value in expression (5.2), we have always (for a magnetic field as strong as the one present in magnetars):

$$S(B) > S_{\max} \quad (5.5)$$

this means that the crust will always break up by such a strong magnetic field. As it was also shown in [6], a magnetic field $B = 10^{13}$ Gauss like the ones in the ordinary pulsars, cannot break the crust. The energy releases by crust breaking from the magnetic field is comparable with the one released in the main peak in the SGR:

$$E_{\text{break}} \simeq lR^2 \mu \theta_{\max} \simeq 10^{39} \left(\frac{\theta_{\max}}{10^{-3}} \right) \left(\frac{\Delta\theta}{10^{-4}} \right) \left(\frac{l}{10^5 \text{ cm}} \right) \text{erg} \quad (5.6)$$

where $\Delta\theta$ is the crust motion around an angle θ .

From those considerations, it appears to be really important to include a solid crust to explain the observed QPOs in SGRs. In the following sections, we investigate the impact of a solid crust on QPOs frequencies and we show, that a model with a solid crust and a fluid core, could explain all the observed data in SGRs tail.

5.1 Model

We model the star as a fluid core enclosed in a solid crust. We used two representative EOS for the fluid core and match them at the interface between crust and core with an equation of state for the crust derived by Negele & Vautherin (in the following NV, see [67] for more details). We choose the NV equation of state for the crust because it describes a thicker crust: this give as the opportunity to use a wider grid for our simulation and so to study in details the phenomena that happen in the crust. The thickness of the solid crust depends on the equation of

CHAPTER 5. COUPLED CRUST-CORE MAGNETO-OSCILLATIONS

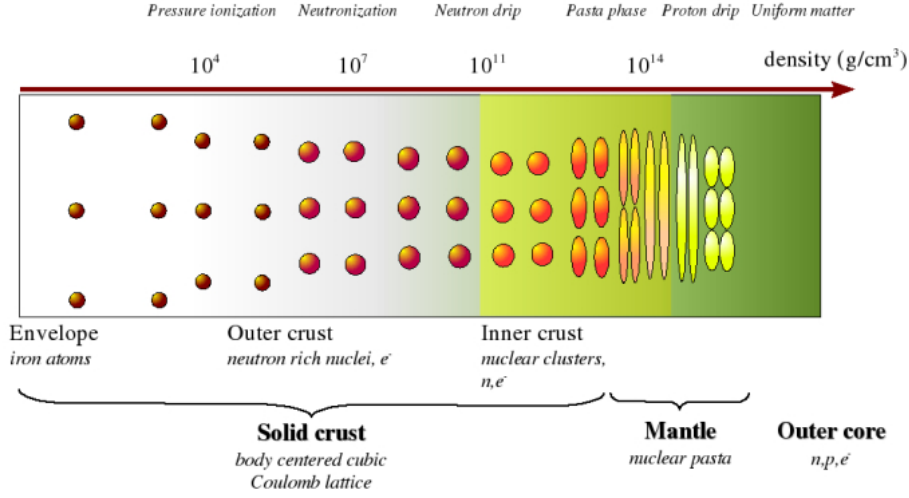


Figure 5.1: A schematic representation of the structure of the crust of a neutron star (Credit: Université of Libre de Bruxells).

state that we use, but in all the models, the relative thickness $\Delta r/R$ is less than 1%. We construct a numerical equidistant grid 90×90 in the (X, Y) coordinates, setting $X_{\max} = \sqrt{a_{1 \max}} \sin \theta$ and $Y_{\max} = \sqrt{a_{1 \max}} \cos \theta$ and varying θ from 0 and $\pi/2$. The bottom limit of the crust (that we identify with $X_{\text{crust}}, Y_{\text{crust}}$) is taken at $\rho = 2.4 \times 10^{14} \text{ g/cm}^3$, according to the value predicted by NV.

First, we evolve the one-dimensional equation (4.1) through all the core, until the points $(X_{\text{crust}}, Y_{\text{crust}})$ that correspond to the bottom of the crust. We have to pay a special attention when the perturbation crosses the maximum of a_1 , ($X_{\max} = \sqrt{a_{1 \max}} \sin \theta$, $Y_{\max} = \sqrt{a_{1 \max}} \cos \theta$): at this point the sign in the first derivative of a_1 changes and then from here until the surface we have to use the transformation of coordinate (3.63) instead of (3.50). Apart from this device, the perturbation evolves on each magnetic “strings” independently from the others: no matching among them is present beside the one on the interface between crust and core. In this way no information is exchanged among the strings, that then will still conserve their own frequency, which is different for each string, as we will explain later.

In the crust until the surface (i.e. from the points $(X_{\text{crust}}, Y_{\text{crust}})$ to the points $(X_{\text{surf}}, Y_{\text{surf}})$), the equation to use is (3.40): the problem becomes then two dimensional, and each string is linked to the nearest strings in both the Y direction and in the X direction, forming a kind of membrane. The strings

oscillate then together: the frequency on one string is not independent from the presence of the other strings as in the case treated in the previous chapter. We need an extra boundary condition on the base of the fluid-core interface: this condition in (r, θ) coordinates is given by (see [24] and [25]):

$$\mathcal{Y}_{,r(-)} = \left[1 + \frac{(2\ell - 1)(2\ell + 3)}{3(\ell^2 + \ell - 1)} \frac{v_s^2}{v_A^2} \right] \mathcal{Y}_{,r(+)} \quad (5.7)$$

where v_A and v_s are defined respectively in equation (4.19) and equation (5.3). In the (X, Y) coordinates the condition above becomes:

$$\left[X \frac{\partial \mathcal{Y}}{\partial X} + Y \frac{\partial \mathcal{Y}}{\partial Y} \right]_{(-)} = \left[1 + \frac{(2\ell - 1)(2\ell + 3)}{3(\ell^2 + \ell - 1)} \frac{v_s^2}{v_A^2} \right] \left[X \frac{\partial \mathcal{Y}}{\partial X} + Y \frac{\partial \mathcal{Y}}{\partial Y} \right]_{(+)} \quad (5.8)$$

We tested the stability of the code by performing a quite long simulations lasting 2 seconds. We found that the code didn't show an exponential growth or any other form of numerical instability.

5.2 Results

We study models with different masses and radius and we find that the observed data can be reproduced for stellar model with mass of $M = 1.4 M_\odot$. The radius varies from $R = 10.9$ km (for the model WFF) to $R = 11.9$ km (for the model APR). The magnetic field on the surface is set to $B = 4 \times 10^{15}$ Gauss. We analyse the results that we get from our code, finding the frequencies through a Fourier Transform and reconstructing the eigenfunctions of these frequencies in order to explore what parts of the star are excited most and to find out if the specific frequency set the whole star in oscillation (discrete mode) or if it is part of a continuum. The eigenfunctions are reconstructed using the eigenfunctions recycling program already used in [68] (see there for more details).

The frequencies that we find must be compared with the observed data and with our precedent model, presented in chapter 4.

In the previous chapter, where we studied the oscillations of a fluid star model without crust, we discovered that the axisymmetric torsional oscillations formed a continuous spectrum. Now, we find that although the core still maintains this behaviour, i.e. the oscillations form a continua, the oscillations associated with the crust show a discrete spectrum as was found in [24]. In addition to the

CHAPTER 5. COUPLED CRUST-CORE MAGNETO-OSCILLATIONS

discrete crust frequencies and to the continuum spectrum of the core, we find a new family of discrete modes: we labelled those modes ‘discrete Alfvén modes’, because, although they have a discrete spectrum, they scale with the magnetic field, in the same way as the Alfvén continua do.

The continuous spectrum is emerging for magnetic fields stronger than $B = 10^{14}$ Gauss. To verify this, we perform simulation with weaker and stronger magnetic field than $B = 4 \times 10^{15}$ Gauss. We find that an increase of the magnetic field generates a wider continua, i.e. the edge of the continua are moving far away from each other. On the contrary, a decrease in the strength of the magnetic field leads to weaker oscillations in the continua, up to a point where the continuum disappears and only the crust frequencies do show up (the critical transition value is around $B = 10^{14}$ Gauss, see next section for more details). Changing the strength of the magnetic field is also changing the ratio among the crustal frequencies. It was noted by Schumacker & Thorne [52] and McDermott et al. [69], that the fundamental crustal frequencies f_0^{crust} and the overtones f_ℓ^{crust} are linked by the following relation:

$$f_{\ell+1}^{\text{crust}} = \sqrt{\frac{\ell+1}{\ell}} f_\ell^{\text{crust}} \quad \text{for } n = 0 \quad (5.9)$$

$$f_n^{\text{crust}} = n f_0^{\text{crust}} \quad \text{for } n \gtrsim 1 \quad (5.10)$$

Those results are confirmed by Sotani et al. [24]. We verify these relations in presence of a low magnetic field $B = 10^{13}$ Gauss, but as the magnetic field increases, the effect of the continua begins to become important. Initially, it affects the scaling in relation (5.9) for intermediate magnetic field strengths, but as the strength of the magnetic field increases, the continuum totally absorb some of crustal frequency. This is the case when the magnetic field strength is $B > 4 \times 10^{15}$ Gauss. For a magnetic field $B = 4 \times 10^{15}$ Gauss, that we use in most of our calculations in this thesis, the crust frequencies behave as:

$$f_\ell^{\text{crust}} = (\ell - 1) f_{\ell=2}^{\text{crust}} \quad \text{for } \ell > 2 \quad (5.11)$$

see the continua line in Figure 5.2 and Figure 5.3. We stress that the transition from the relation (5.9) to (5.11) is not sudden but smooth, with the spacing of the different frequencies becoming wider as the magnetic field becomes stronger. This will be discussed in more details in the next section.

Another important issue is the comparison of our data with the timing analysis of the SGR 1806-20 and SGR 1900+14 calculated in [70]. In this paper, the authors identified several QPOs, of different duration, in the tail of the two events. In particular, for the more recent event, SGR 1806-20, the identified frequencies are 18, 26, 30, 92, 150, 625 and 1840 Hz while for the SGR 1900+14

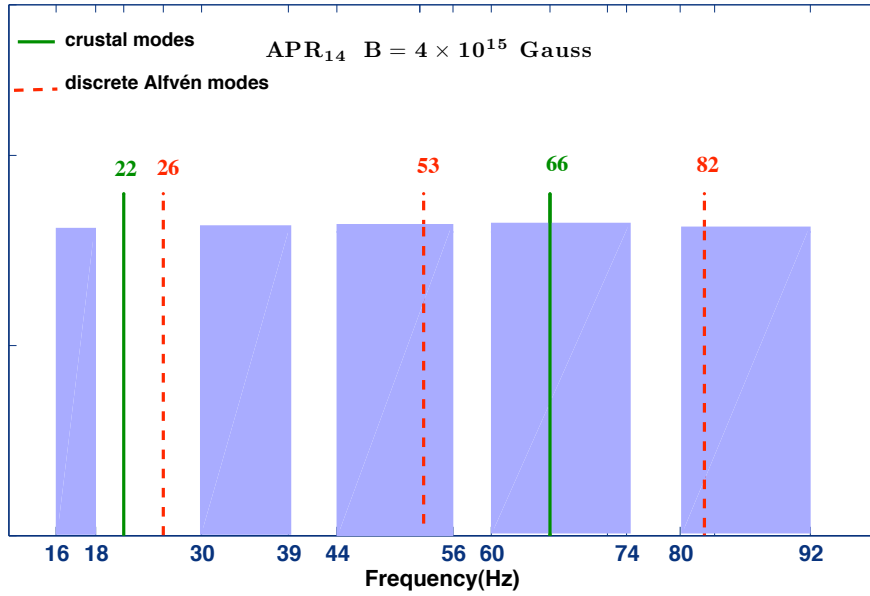


Figure 5.2: Identification of the frequencies of SGR 1806-20(16Hz, 18Hz, 26Hz, 30Hz, 36Hz, 92Hz), using the stellar model APR with mass $M = 1.4M_{\odot}$

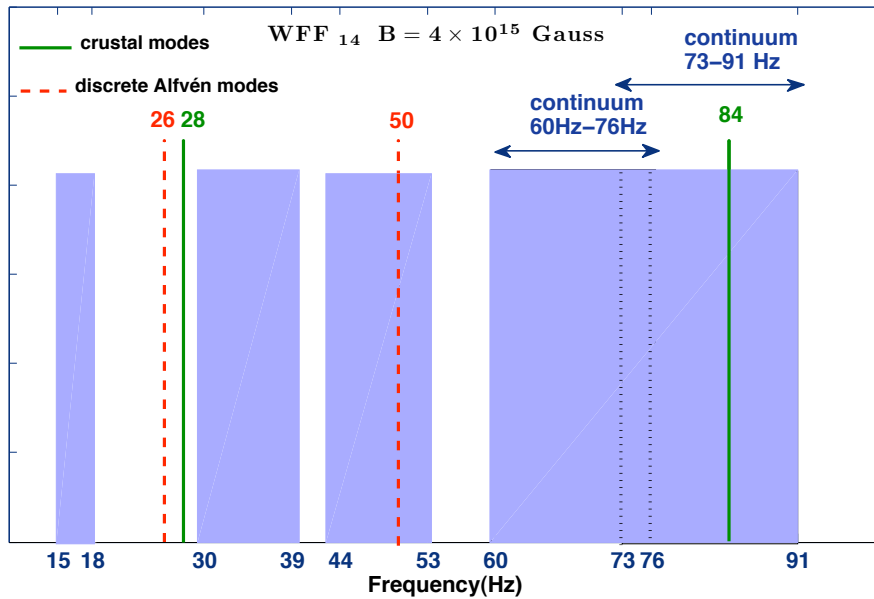


Figure 5.3: Identification of the frequencies of SGR 1900+14, using the stellar model WFF with mass $M = 1.4M_{\odot}$. The ‘discrete Alfvén frequencies’ (22Hz, 55Hz, 83Hz) could be identified with the observed frequencies of SGR 1900+14.

CHAPTER 5. COUPLED CRUST-CORE MAGNETO-OSCILLATIONS

they found the following frequencies: 28, 53, 84 and 155 Hz. A more recent, yet unpublished study by Hambaran et al. [71], based on predictions by Colaiuda et al. [72], confirms, by using a different analysis technique, the earlier results by Strohmayer & Watts and reveals, in addition, at least three new frequencies for the SGR 1806-20 these are 16.88, 21.36 and 36.84 Hz.

All the previous model, that studied the QPOs in magnetars, have difficulties to explain the lower frequencies, narrow spacing among those frequencies. For this reason, it was really difficult to explain the triad 18Hz-26Hz-30Hz and if we consider also the new frequencies found in [71], then it is really a hard task to explain them via crust oscillations alone or via the Alfvén continua in the core [72, 58]. In fact, as we have shown in chapter 4, a stellar model constituted by a fluid core, without a solid crust, cannot explain the lower frequencies. This observation lead to the conclusion that the coupling between crust and core is the only way for explaining all the observed data. Here we show that such hypothesis is true and that our model with a consistent coupling between solid crust and fluid core, can not only explain the observed data but also can predict non-observed ones.

We will focus on the lower frequencies since the higher ones could be explained easily, and not in a unique way, as multiples of the lower ones.

In Figure 5.2 for the model APR₁₄ and Figure 5.3 for the model WFF₁₄, we show the range of the continua (light blue bars) as well as the discrete crust (continue blue line) and ‘discrete Alfvén’ frequencies (dotted red line), a new type of frequencies that are not present in absence of crust (see previous chapter). In the following sections, we will analyse the characteristics of all those three types of frequencies.

5.2.1 The continua

The continua is a feature of the fluid core, and their presence is expected from our study described in the previous chapter. However, the presence of a crust and the coupling between crust and core at the interface influences the continuous spectrum, not only in the values of the frequencies but also in some of their features. It is evident that the continua present gap in its structure, as it was recently pointed out in [35] where the authors use a toy model with coupled oscillators. In addition, the upper frequencies are not evidently located near the magnetic axis, as in the case of a totally fluid star (see for example the bottom plot in Figure 5.6). Despite those differences, the frequencies of the continua show still a relation between upper and lower frequencies, as the ones in equations (4.20-4.23): if we consider $f_{L_0} = 16\text{Hz}$ and $f_{U_0} = 18\text{Hz}$ respectively as fundamental

lower and upper frequencies, then the others frequencies can be explained as their multiples. In fact, the edges of the second continuum (presented in Figure 5.5) are roughly following the equations (4.22) and (4.23), for $n = 1$. The third continua (see Figure 5.6) is generated from the $f_{L_0} = 16\text{Hz}$ and $f_{U_0} = 18\text{Hz}$ by the equations (4.20) and (4.21), for $n = 1$. Note that, while the crust frequencies are multiple of the fundamental frequency with a multiplicity given by ℓ , the multiplicity of the continua is given by n .

A few words about the features of the continua. It can be seen from Figure 5.4 and Figure 5.5, that the edges of different continua present the same features: the 16 Hz and the 30Hz frequencies, respectively the lower edge of the first and second continua (see upper plot in both Figure 5.4 and Figure 5.5), are located closer to the beginning of the closed lines, i.e. the magnetic field lines that close inside the star, not reaching the surface and obviously not matching the exterior magnetic field. The 18Hz and the 39Hz, set respectively the upper edge of the first and second continua (see bottom plot in both Figure 5.4 and Figure 5.5), seem to excite large amplitude motion towards the center, with branches near the magnetic axis.

The form of the eigenfunctions changes at higher frequencies: in fact, they show a more complicated structure, given by the presence of more nodes of the eigenfunctions inside the star, with the increase of n (for the core) or ℓ (for the crust). The higher family of QPOs is not anymore strictly located near the magnetic axis as in the case of a pure fluid star, but the f_{U_0} frequencies occupy the central-inner part of the core and part of the crust, demonstrating how the crust-core coupling changes dramatically the features of the continua.

The gaps in the continua, suggested by van Hooven and Levin [35], are present in both the models that we analyse, but while in the APR₁₄ model we can observe gaps also at relatively high frequencies, in the WFF₁₄ model the third and the fourth continua merge and the gap disappears (see Figure 5.2 and Figure 5.3). We can then conclude that the presence of the gaps in the continuum spectrum is more a characteristic of the model than a sign of the crust-core coupling.

Regarding the close magnetic fields line, that are located in the outer region of the star, beginning at $(x = 0.8, y = 0.0)$ and ending at $(x = R, y = 0.5)$, one can barely see some kind of structure: this is because, the amplitude of the perturbation brought by the closed magnetic field lines is orders of magnitude lower than the open ones in the core and in the crust, when they are bot excited with the same initial perturbation (as we did).

CHAPTER 5. COUPLED CRUST-CORE MAGNETO-OSCILLATIONS

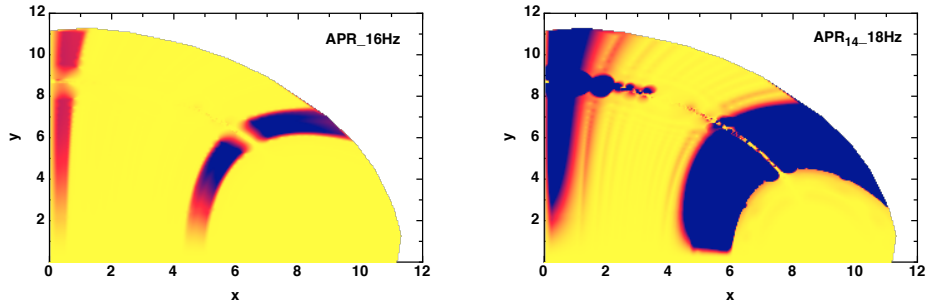


Figure 5.4: Oscillation patterns (eigenfunction) of the edges of the first continua for the model APR_{14} (better fit for the SGR 1806-20): the yellow part corresponds to the not perturbed part of the star, while the blue and the red parts represent respectively an intense and a medium perturbation in the star.

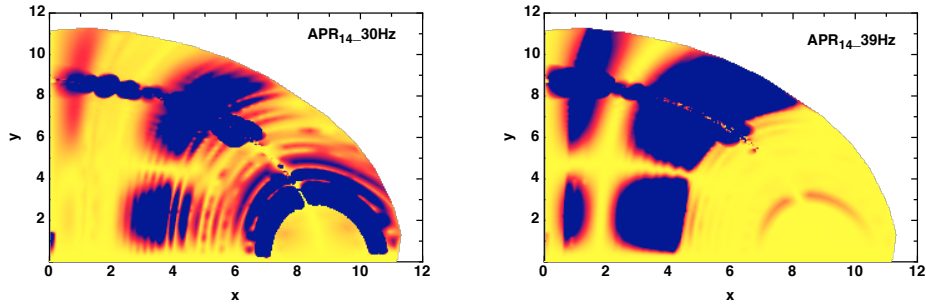


Figure 5.5: Oscillation patterns (eigenfunction) of the edges of the second continua for the model APR_{14} (better fit for the SGR 1806-20).

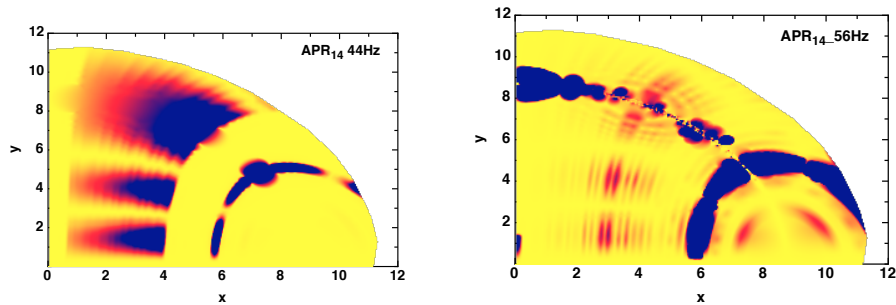


Figure 5.6: Oscillation patterns (eigenfunction) of the edges of the third continua for the model APR_{14} (better fit for the SGR 1806-20).

5.2.2 The crust frequencies

The crust frequencies are known to have a discrete nature. In [24], the authors calculate the crustal frequencies for a non-magnetized model and then show through a 2d-simulation how the presence of a magnetic field is influencing those results. They find that the magnetic field begins to have a significant effect on the frequencies, only if it is stronger than $B_{\text{cri}} \gtrsim 10^{14}$ Gauss. Otherwise its effect is negligible. In our model, choosing a magnetic field lower than B_{cri} and imposing a non-traction condition at the interface between crust and core (cancelling in such a way the coupling effect between them), we recover the results in [24], with an accuracy of about 1%. However, the presence of a fluid core permeating by a magnetic field of the same strength of the one in the crust and the coupling between crust and core, change this picture. The crust frequencies are strongly damped and transfer a significant part of their initial oscillations energy to the core, driving it to oscillate even if no initial perturbation is present there. This means that the crust frequencies are not strictly confined in the crust but they propagate their energy also in the core as can be seen from Figure 5.11 and Figure 5.14. Note that, analysing different FFT on points in the crust, we can confirm the discrete nature of these frequencies. The transfer of the energy of a crust oscillation is even worst if the crust frequency is embedded in the continua: in this case, the oscillation energy of the crust is transferred in the continuous spectrum mainly the edges of the continua as we will explain in details in the next section.

5.2.3 Discrete Alfvén modes

We identify the eigenfunctions represented in Figure 5.12a and Figure 5.12b as ‘discrete Alfvén’ modes. Those modes appear just when a coupling between crust and core is present: in fact, we don’t find them when the star is constituted by a pure fluid. The presence of discrete Alfvén modes was also noted in [35], where the authors find some discrete modes near the edges of the continua. Also In our case, the location of those discrete Alfvén modes is near the edges of the continua, except the fundamental one that is always located a little more far away from the edge of the first nearest continua. The eigenfunctions of those frequencies are similar to the one in the crust (see Figure 5.12a and Figure 5.12b for an example of discrete Alfvén modes and Figure 5.14 for an example of crust frequencies). Despite to this similarity and of their discrete nature, those modes scale with the magnetic field, getting lower or higher, depending of the magnetic field is increased or decreased, as it can be seen in Figure 5.9 and Figure 5.10, where we plot the results of our simulations for a magnetic field’s strength respectively

CHAPTER 5. COUPLED CRUST-CORE MAGNETO-OSCILLATIONS

of $B = 2 \times 10^{15}$ Gauss and $B = 4.25 \times 10^{15}$ Gauss. This behaviour reveals the Alfvén nature of those modes. In fact, the frequencies of those modes change according to:

$$f = \frac{v_A}{L} \quad \text{where} \quad v_A = \frac{B}{\sqrt{4\pi\rho}} \quad (5.12)$$

where L is the distance that the wave ‘travels’, v_A is the Alfvén velocity, B is the magnetic field that permeates the star and ρ is the density of the star. Figure 5.10 and Figure 5.9 show how this prediction is true for the ‘discrete Alfvén frequency’ (the pointed red line moves with increasing or decreasing of the strength of the magnetic field, as predicted by equation (5.12)).

Finally, the scaling of these modes follows the scaling observed in the continua i.e.

$$f_n^{(D)} \approx (n + 1)f_0^{(D)}. \quad (5.13)$$

5.3 From discrete crustal modes to a continuum spectrum

As test run for our model, we reproduce the results derived in [24] for pure crust oscillations. In this paper, the authors studied the torsional oscillations of both a non magnetised and a magnetised star. They also consider, as a first approximation, the no-traction condition in the core-crust interface, i.e. instead of the condition (5.7), they require that \mathcal{Y} must be continuous through the interface i.e. $\mathcal{Y}'_{(+)} = \mathcal{Y}'_{(-)}$.

Here, we cannot set the magnetic field equal to zero since our coordinate system (X, Y) is based on the strength of the magnetic field i.e. on $a_1(r)$. However, as it was already been shown in [24], the influence of the magnetic field on the frequencies becomes important only if $B > 10^{15}$ Gauss, thus we can choose a very low magnetic field for magnetars, e.g. $B = 10^{14}$ Gauss, and perform test runs in order to compare our results with the ones in [24]. Using this magnetic field and the no-traction condition on the interface, we find the results reported in [24]. This test verified that the code could reproduce the previous results for the torsional oscillations of the crust (see Figure 5.7).

In a similar way we could isolate the continuum spectrum as it has been found in [72] and try to check if we can reproduce these results by varying the strength of the magnetic field. In fact, we expect that from sufficiently strong magnetic field, the effect of the crust can be neglected since the continua assumes the predominant role, being based on the magnetic field’s strength. In addition, at the interface, the formula (5.8) is reduced to the formula (3.61), since the second

term at the right side of the equation (5.8), tends to zero for high magnetic field, since the Alfvén velocity v_A increases, while the shear velocity is not affected. We find that for a magnetic field $B > 10^{16}$ Gauss, the results for a purely fluid star, as the one of the previous section, are reproduced.

From those two simulations, it is clear that the crust frequencies are the ones whose nature and spectral properties are changing the most, due to the presence of the magnetic field. In fact, it is known (see [52]), that crustal frequencies can be estimated quite well from the following relation:

$$f_\ell^{\text{crust}} = \sqrt{\ell(\ell+1)} - 2 \frac{v_s}{2\pi R} \quad \text{for } n = 0 \quad (5.14)$$

where v_s is shear velocity, that we set $v_s = 10^8 \text{ cm s}^{-1}$ and R is the stellar radius, while for the higher harmonics, we got:

$$f_n^{\text{crust}} = n f_0 \quad \text{for } n \geq 0. \quad (5.15)$$

However, we observe this behaviour only for very low magnetic field (see Figure 5.7), while for stronger magnetic fields, the crust frequencies do not scale anymore in this way. Already in the simulation with $B = 4 \times 10^{15}$ Gauss, the frequencies, that we can associate with the crust, follow a law different than (5.14), given by:

$$f_\ell^{\text{crust}} = (\ell - 1) f_{\ell=2}^{\text{crust}} \quad \text{for } \ell > 2 \quad (5.16)$$

where we assume $f_{\ell=2}^{\text{crust}} = 22 \text{ Hz}$. We want then to understand, when the transition between the law (5.14) and the law (5.16) takes place. For this reason, we perform several runs with intermediate strengths of the magnetic field, i.e. we let the magnetic field vary between the value $B = 10^{14}$ Gauss and $B = 4 \times 10^{15}$ Gauss.

We start with a magnetic field $B = 6 \times 10^{14}$ Gauss. For such magnetic field, although the continua is still not too strong, the crustal frequencies begin to deviate from the law (5.14), see Figure 5.7, while some frequencies disappear, as for example, does the 30Hz frequency. When we increase the magnetic field to $B = 2 \times 10^{15}$ Gauss, the continua begins to dominate and it is evident that due to their presence, we observe those dramatic change in the behaviour of the crust frequencies. In fact, as it can be seen from Figure 5.9, every second crustal frequency is lost, probably absorbed in the continua.

In order to understand how a crustal frequency could be absorbed by the continua, we perform a run with a magnetic field strength $B = 4.25 \times 10^{15}$ Gauss (see Figure 5.10). We choose this value, because we want to construct a model, where the 66 Hz crustal frequency is not embedded in the continua, as it is for

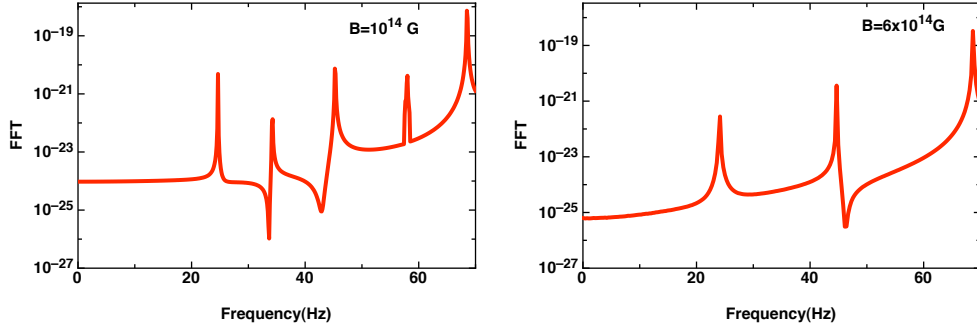


Figure 5.7: Discrete QPOs in the presence of weak magnetic fields. *Left Panel:* the magnetic field strength is $B = 10^{14}$ Gauss. *Right Panel:* the magnetic field strength is $B = 6 \times 10^{14}$ Gauss.

Note that, the plot on the left is scaling according to equation (5.14), while in the one on the right, the frequencies scale according to the relation (5.16). In addition, it is possible to observe the disappearance of some of the frequencies, comparing the left panel to the right one.

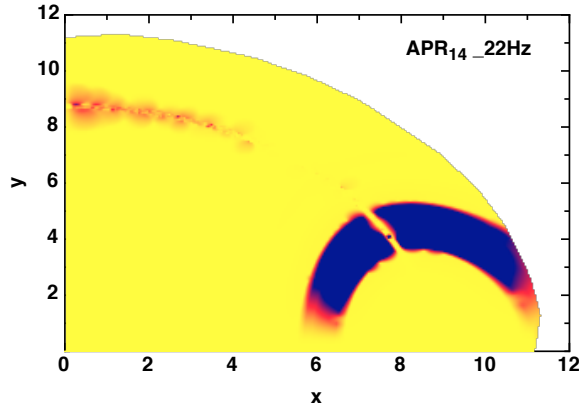


Figure 5.8: The oscillation pattern (eigenfunction) for the $\ell = 2$ ‘crustal’ frequency of 22Hz. The model is the APR_{14} with a magnetic field $B = 4 \times 10^{15}$ G.

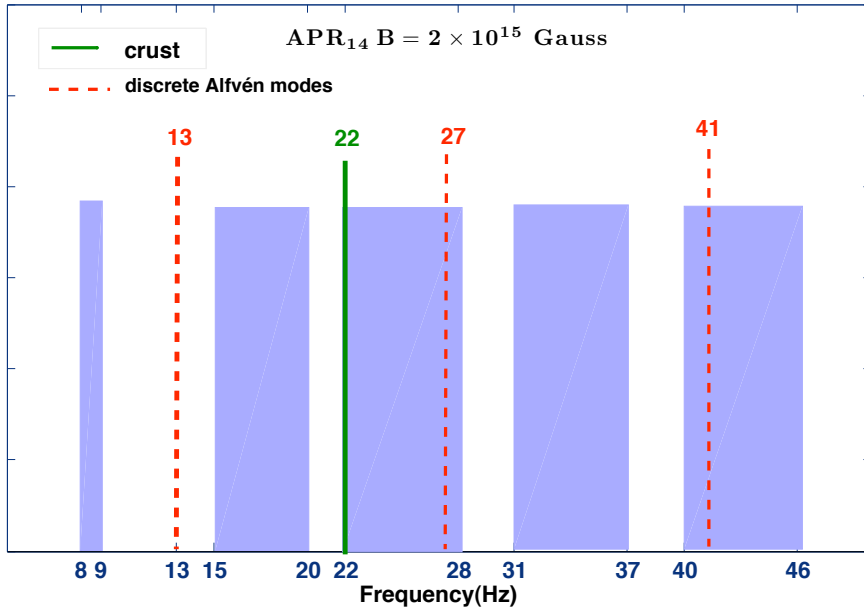


Figure 5.9: QPOs frequencies for a magnetic field strength $B = 2 \times 10^{15}$ Gauss and the APR₁₄ stellar model.

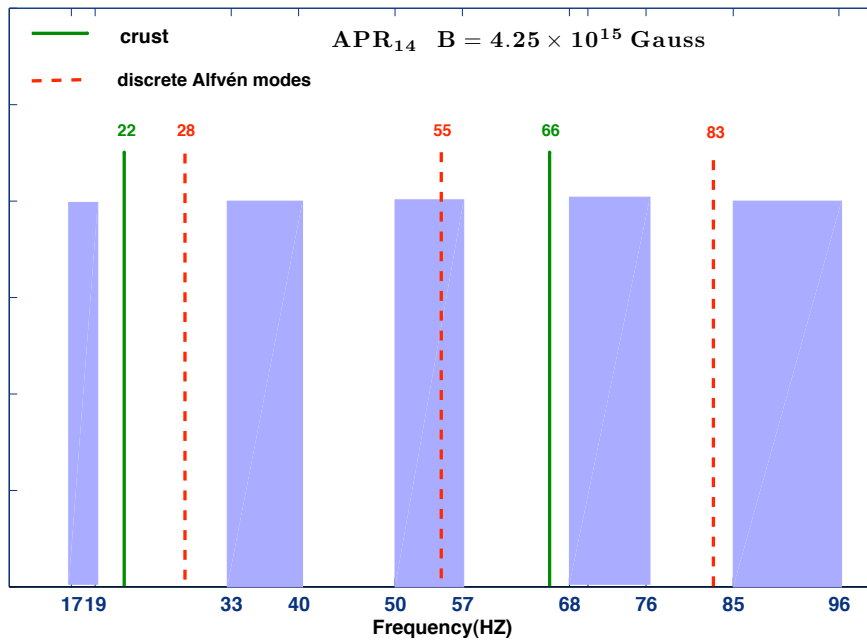


Figure 5.10: QPOs frequencies for the APR₁₄ stellar model with a magnetic field strength $B = 4.25 \times 10^{15}$ Gauss.

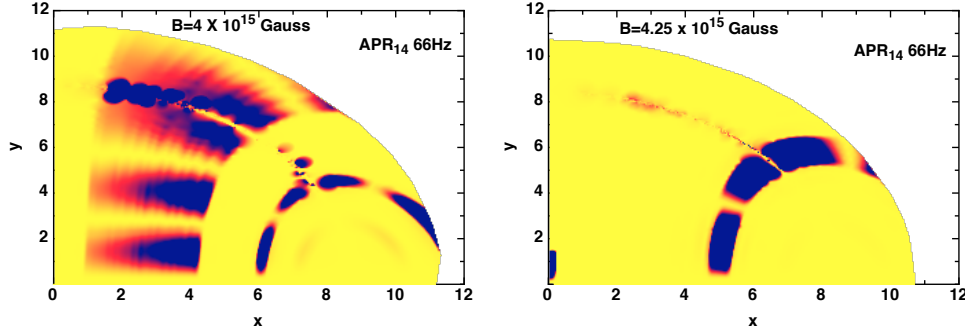


Figure 5.11: The oscillation patterns (eigenfunctions) for the 66Hz ‘crustal’ frequency for the stellar model APR_{14} . *Left Panel:* For a magnetic field strength $B = 4 \times 10^{15}$ Gauss, the 66Hz is located in the fourth continua and its eigenfunction has the same feature of one of the third continuum (see left panel in Figure 5.6). *Right Panel:* When the magnetic field strength is $B = 4.25 \times 10^{15}$ Gauss, the 66Hz frequency is located outside the continua and it looks like the fundamental 22Hz ‘crustal’ frequency (see Figure 5.8), with an additional node, since the 66Hz frequency represents the $\ell = 3$ ‘crustal’ frequency.

$B = 4 \times 10^{15}$ Gauss, see Figure 5.2. The structure of the eigenfunction of the 66Hz frequency when it is embedded in the continua and when it is outside of the continua are reported respectively, in the left and right panel of Figure 5.11. In the first case, the eigenfunction trace the structure of the continua that hosts the crustal frequency, while in the second case, the eigenfunction of the crustal frequency resemble the one of the first crust frequency, the 22Hz plotted in Figure 5.8, but with one more node, since the 66Hz frequency corresponds to the first high ℓ that we find in our simulation. In addition, we find that, when the crust frequency is embedded in the continua, a big part of its energy is transferred during the time evolution in favour of the edges of the continua that hosts it. On the contrary, in the case where the crustal frequency is outside, the continua we cannot observe such behaviour. The evidence of such loss is given by the amplitudes of the FFT peaks, that change, showing a decreasing, when they are calculated at the beginning and at the end of our simulation.

Finally, we made some additional numerical tests, in order to understand how an initial perturbation propagates in the crust and in the core. We set

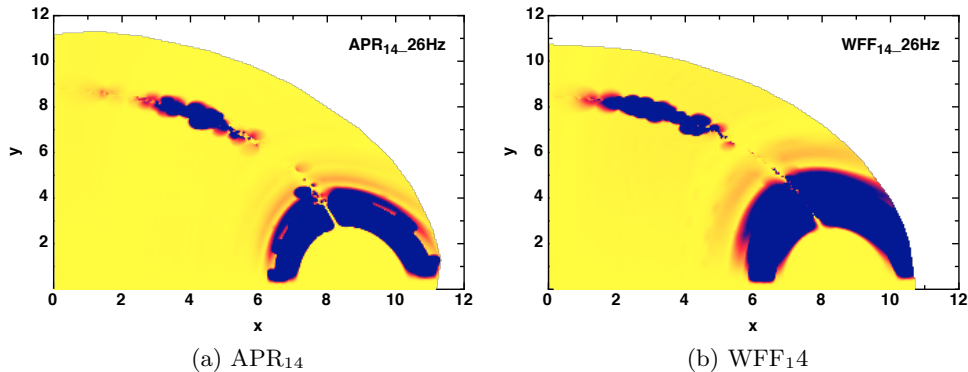


Figure 5.12: Typical eigenfunction (oscillation patterns) of the fundamental ‘discrete Alfvén modes’, for both the models under discussion with magnetic field strength $B = 4 \times 10^{15}$ Gauss.

initial data in order to excite only the crust and to study the diffusion of the initial energy in the system. We assume two different observers inside the star, one in the core and one in the crust. We then calculate the FFT for them at the beginning and at the end of our simulation. We compare their amplitude and we find that the energy quickly flows from the crust towards the core exciting the Alfvén continua. The inverse mechanism did not show the same efficiency i.e. oscillations initiated only in the core find it very hard to propagate into the crust. The conclusion of this test is in agreement with earlier suggestions given in [25] that when the magnetic field permeates the whole the star, the perturbations cannot be confined in the crust.

5.4 Identification of the QPOs observed

As we already pointed out, our model with the coupling between crust and core can satisfactorily explain all the QPOs observed, both in the SGR 1806-20 and SGR 1900+14. We start with the identification of the QPOs detected in the SGR 1806-20, taking into account both the study in [70] and [71]. For this SGR, we find that the model that better fits the observed frequencies is the stellar model APR, with mass $M = 1.4M_{\odot}$, radius $R = 11.57\text{km}$ and crust thickness $\Delta r/R = 0.099$.

The lower QPOs, the 16 Hz, found by [71] and the 18 Hz frequency discovered

CHAPTER 5. COUPLED CRUST-CORE MAGNETO-OSCILLATIONS

by [70], are the first edge of the continua: they are then core frequencies (see Figure 5.4). The 22Hz is a crust frequency, since we observed it as a discrete frequency in the crust. The 26Hz is part of the new family of discrete frequencies that we find (see section 5.2.3 and Figure 5.12a): the discrete Alfvén frequencies. The 29Hz frequency is the lower edge of the second continua (see Figure 5.5) while the 92 Hz can be a high frequency belonging to upper edge of the fifth continua. The higher frequencies can all be explained as multiples of the lower ones following the relations (4.20)-(4.21).

For the SGR 1900+14, few QPOs were identified. This paucity of observations makes difficult to constrain univocally the equation of state of this magnetar. For this reason, two stellar models could explain satisfactory the observed frequencies: the APR model with mass $M = 1.4M_{\odot}$, radius $R = 11.57\text{km}$, crust thickness $\Delta r/R = 0.099$ and magnetic field strength $B = 4.25 \times 10^{15}$ Gauss (see Figure 5.10) and the WFF model, with mass $M = 1.4M_{\odot}$, radius $R = 10.91\text{km}$ and crust thickness $\Delta r/R = 0.085$. The value of the magnetic field $B = 4 \times 10^{15}$ Gauss, see Figure 5.3.

When the APR₁₄ model is used, then the 28Hz, 54Hz and the 84Hz can be all identified with the discrete Alfvén modes. Contrary, using the WFF₁₄ model, the frequencies can be identified both with global modes both with crustal modes. In particular, the 28 Hz frequencies is a crust frequencies (see Figure 5.14) while the 53 Hz frequency can be identify as an upper edge of the continua (see Figure 5.14). Also the 84 Hz is a crust frequency, owing consequently a discrete nature (see Figure 5.14). Note that the model APR (Figure 5.2) shows gaps in the continuum spectrum, according to [35], while in the model WFF (Figure 5.3) there is no gap between the fourth and the fifth continua. This is a propriety of the model WFF, and it was already noted in the case of a purely fluid star (see Table (4.1)).

5.4.1 Time intervals of the detected QPOs

In the study of QPOs, another important issue is their time intervals. Understanding which QPOs are excited first means also to be able to follow the perturbation propagates inside the star. In table (5.1), the QPOs observed for the SGR 1806-20 both by [21] and by [71] are listed. We can see that some QPOs last longer than others: in particular the 17.9Hz and the 25.7Hz set up quite early (just 60 seconds after the giant burst) and last for more than 100 seconds. Their structure inside the star (see respectively the second plot in Figure 5.4 and the plot in Figure 5.12a) presents some similarities respectively with the others frequencies in the continua and with the crust frequencies. The 18Hz eigenfunction

is located mainly inside the star, near the magnetic axis, with a branch localized near the last open line extending through all the star. The 16Hz, that sets up some seconds after the end of the 18Hz oscillations, is quite similar to the structure of the eigenfunction of this latter frequency, with a lesser strong oscillations near the magnetic axis and near the last open line. It seems that the perturbation first present in the 18Hz is passed to the 16Hz, with some loss of energy. The same behaviour can be seen also in the WFF model, for the 15Hz and the 18Hz frequencies (see Figure 5.13)).

Also the 21.36 Hz lasts less than 10 seconds: its behaviour could seem a little more tricky because it is located mainly near the last open magnetic lines (see Figure 5.8), contradicting our hypothesis that the propagation is spreading through out the star and it is moving towards the magnetic axis when the frequency increases. However, the 22Hz frequency is a crust frequency: we know from our simulation that crust frequencies tend to transfer their energy quickly to the core. This could explain why the 22Hz frequency has a so low energy-perturbation pattern. The same behaviour is seen in the 26Hz frequency (see Figure 5.12a), a discrete Alfvén mode: its pattern is really similar to the 22Hz frequency and it sets up early in time, ending just 14 seconds before the beginning of the 22Hz oscillation. It is quite possible that those two frequencies are related, with the 22Hz carrying on the perturbation of the 26Hz.

The remaining frequencies are most likely connected to each other: this could be seen also from the similar time intervals, that indicate an energy passing throughout the star.

Table 5.1: The frequency of the detected QPOs and their duration (in seconds). The data are from [21] and [71].

$f_{QPO}(Hz)$	Time intervals of detected QPOs (s)
16.88	259.4-267.4
17.9	60-230
21.36	244.3-251.9
25.7	60-230
29.0	190-260
36.84	183.8-191.2
59.04	146.0-176.2
61.26	251.9-395.6
116.27	168.7-198.9

CHAPTER 5. COUPLED CRUST-CORE MAGNETO-OSCILLATIONS

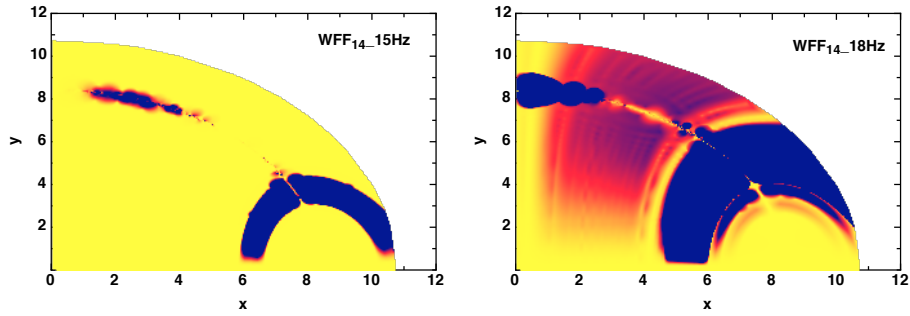


Figure 5.13: Oscillation patterns (eigenfunction) of the edges of the first continua for the model WFF_{14} (better fit for the SGR 1900+14).

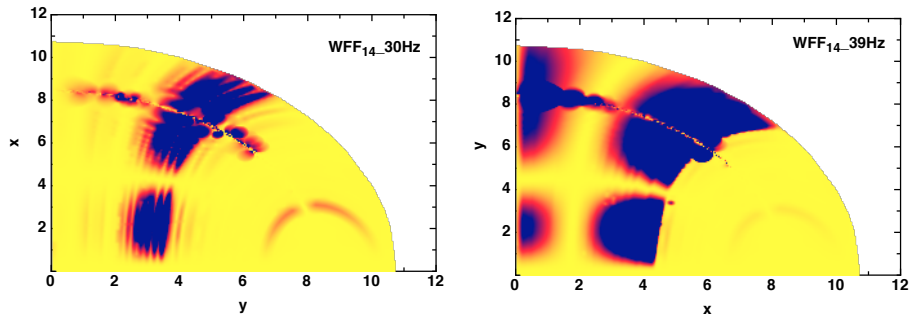


Figure 5.14: Oscillation patterns (eigenfunction) of the edges of the second continua for the model WFF_{14} (better fit for the SGR 1900+14).

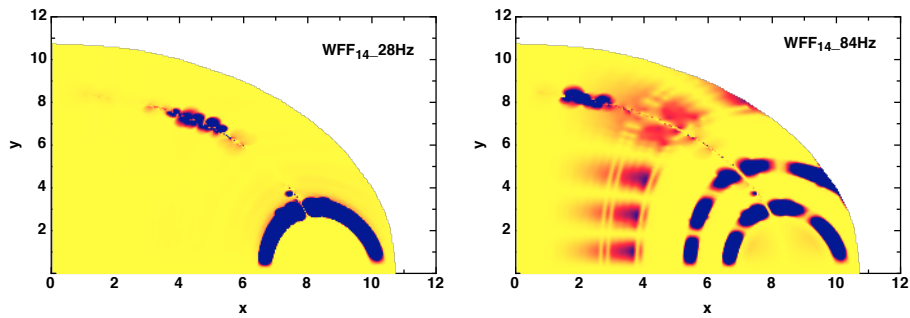


Figure 5.15: Oscillation patterns (eigenfunctions) of two “crust” modes for the model WFF_{14} (better fit for the SGR 1900+14).

6

Summary

In this thesis, we investigated the torsional oscillations of spherically symmetric, non-rotating, relativistic neutron stars, with large magnetic field $B \simeq 10^{14} - 10^{16}$. Such magnetic field strengths make the star a magnetar, a word coined to indicate a Magne(tic) (S)tar, with a very huge magnetic field compared to the one of the ordinary neutron star, $B \lesssim 10^{13}$ Gauss.

In Chapter 1, we give a brief introduction to magnetar observations and to their properties.

In Chapter 2 we derived the equilibrium configuration for a non-rotating, relativistic, spherically symmetric neutron star from Einstein's equations. A stationary magnetic field with both poloidal and toroidal components was added to the equilibrium configuration. Using Euler's equation and Maxwell's equations we could derive the Grad-Shafranov equation, that describes how the magnetic field distributes in the star. Outside the star, we assumed a dipole magnetic field that matches on the stellar surface to the interior magnetic field.

In Chapter 3, we worked out a linearized formulation of oscillations for torsional modes, i.e. non-radial modes that do not involve density perturbation. The coupling of the torsional oscillations to spacetime perturbations is weak and since the evolution of both the fluid and the spacetime is quite cumbersome, we chose to work in the Cowling approximation, i.e. to neglect the evolution of the spacetime. In this way, the treatment of the problem becomes significantly simple, without any serious compromises on the actual physics problem. In addition, we

did not take into account the deformation of the shape of the star by the presence of the magnetic field because the magnetic energy is many orders of magnitude smaller than the bounding energy. By using those approximations, we derived an unique 1+2 time-evolution equation that describes torsional oscillations of a magnetised star. This equation shows a parabolic behaviour in every point of its domain that leads to an instability during time evolutions. To stabilise the equation, the introduction of an artificial viscosity was necessary. This artificial viscosity appears in the equation as a fourth-order derivative and could distort the final results. In order to avoid it, we introduced a new coordinate transformation based on the magnetic field strength. The effect of this transformation on the the magnetic field lines is to make them straight, so that they appear similar to ‘strings’ coupled only at the surface. The perturbation then evolve along these magnetic field ‘strings’ and the 1+2 evolution equation is reduced to a 1+1 evolution equation (along the time and one space direction). At the end of Chapter 3, we described the boundary conditions required for the solution of the new 1+1 evolution equation.

In Chapter 4, we studied the 1+1 time evolution equation found previously in Chapter 3 for a star composed solely of a perfect fluid without the presence of a crust. We showed that, in this case, the problem is reduced to an evolution of the perturbation along the magnetic ‘strings’, where every magnetic ‘string’ does not communicate with the others (except for a weak coupling at the surface), due to the 1+1 nature of the equation. We noted that not all the magnetic ‘strings’ behave in the same way: in fact, we have two types of magnetic strings, the ‘closed’ and the ‘open’ magnetic ones. The first group comes from the stretching of the ‘closed’ magnetic lines i.e. the magnetic lines that close themselves inside the star and do not reach the surface. They, then, do not communicate at all with each other and are totally separated from the open magnetic ‘strings’. Those latter are created by the open magnetic field lines, that reach the surface and match the dipole magnetic field outside the star. Then, there is a weak coupling of the ‘strings’ on the surface, where there is a weak transfer of energy between the ‘strings’ due to the boundary condition that is implemented there, i.e the traction should vanish. We discovered that the oscillations spectrum forms a continuum, delimited by two edges that we identified with two different families of QPOs: an ‘upper family’ with higher frequencies located near the magnetic axis and a ‘lower family’ (with lower frequencies) located near the last open magnetic ‘string’. We showed that the frequencies found explain most of the observed QPOs but not all. In particular it is difficult to explain the spacing of the lower QPOs.

In Chapter 5, we investigated a more complex model, analysing the torsional

oscillations of a star with a fluid core and a solid crust. We found out that, while in the fluid core the problem is still a 1+1 evolution equation, in the crust the problem becomes a 1+2 evolution equation due to the presence of a non-vanishing shear modulus. The scheme to evolve is then still formed by single magnetic ‘strings’ in the core but in the crust the magnetic ‘strings’ are linked together to form a membrane. We coupled the single magnetic strings in the core with the membrane in the solid crust by appropriate boundary conditions on the interface, which corresponds to the base of the crust. We found that the spectrum of the core oscillations still forms continua but the presence of the crust adds new discrete frequencies, which seems to be fossils of the pure crust oscillations when the magnetic field is weak or absent. In addition, we found a new family of modes that behave as Alfvén modes but have a discrete character. We called those modes ‘discrete Alfvén modes’. Finally, we analysed how the core and the crust interact with each other and found that a considerable amount of energy is passed from the crust to the core, especially when crust modes are embedded in the continua. In addition, we performed several tests with different strength of the magnetic field, to study its influence on the oscillation spectrum. We found that for a magnetic field around $B = 10^{14}\text{G}$ the crustal frequencies discovered by Sotani et al. [24] appear, while as the magnetic field increases the continua appear, together with the discrete Alfvén modes. For a magnetic field strength $B > 10^{16}\text{G}$, the continuous spectrum dominates and absorbs the crustal frequencies.

To conclude, we showed that a star model with fluid core and solid crust, could explain all the observed QPOs frequencies, including the lower ones. In this way we proposed that specific magnetar models can uniquely explain the observed QPOs. This can be an alternative way for constraining neutron star parameters, as mass, radius, equation of state and magnetic field strength.

In future, it will be interesting to include in our model, the magnetosphere that it is known to play a major role in the observed magnetar emission and also to simulate the sequence of events, i.e how the various QPOs are excited one after the other, and to find out why some of them last for very long and others for considerably shorter time intervals. Finally it will be of great importance the study of the influence of the superfluidity in our results.

Acknowledgements

I would like to thank my supervisor Kostas Kokkotas for all his help and all the time that he spent with me discussing and improving this thesis. I am also grateful to Prof. Horst Beyer for providing a helpful mathematical transformation for our work, and to Dr. Hajime Sotani for useful discussions. Many thanks also to Dr. Paul Lasky and Dr. Kostas Glampedakis for their carefully reading of my thesis and for their suggestions which improved it considerably.

I would like to acknowledge my family, especially my parents, the friends that I have made in Tübingen and the ones that I left in Rome and that, although the great distance, always supported me during those years.

And, of course, I would like to thank Erich without whose love and encouragement I would never have finished this work.



Bibliography

- [1] W. Baade and F. Zwicky. Remarks on Super-Novae and Cosmic Rays. *Physical Review*, 46:76–77, July 1934.
- [2] A. Hewish, S. J. Bell, J. D. H. Pilkington, P. F. Scott, and R. A. Collins. Observation of a Rapidly Pulsating Radio Source. *Nature*, 217:709–713, February 1968.
- [3] F. Pacini. Energy Emission from a Neutron Star. *Nature*, 216:567–568, November 1967.
- [4] T. Gold. Rotating Neutron Stars as the Origin of the Pulsating Radio Sources. *Nature*, 218:731–732, May 1968.
- [5] J. P. Ostriker and J. E. Gunn. On the Nature of Pulsars. I. Theory. *ApJ*, 157:1395–+, September 1969.
- [6] C. Thompson and R. C. Duncan. The soft gamma repeaters as very strongly magnetized neutron stars - I. Radiative mechanism for outbursts. *MNRAS*, 275:255–300, July 1995.
- [7] R. C. Duncan. Triggers of magnetar outbursts. In P. Höflich, P. Kumar, & J. C. Wheeler, editor, *Cosmic explosions in three dimensions*, pages 285–+, 2004.
- [8] C. Thompson, M. Lyutikov, and S. R. Kulkarni. Electrodynamics of Magnetars: Implications for the Persistent X-Ray Emission and Spin-down of the Soft Gamma Repeater and Anomalous X-Ray Pulsars. *ApJ*, 574:332–355, July 2002.
- [9] M. A. McLaughlin, A. G. Lyne, D. R. Lorimer, M. Kramer, A. J. Faulkner, R. N. Manchester, J. M. Cordes, F. Camilo, A. Possenti, I. H. Stairs, G. Hobbs, N. D’Amico, M. Burgay, and J. T. O’Brien. Transient radio bursts from rotating neutron stars. *Nature*, 439:817–820, February 2006.

BIBLIOGRAPHY

- [10] K. Hurley, T. Cline, E. Mazets, S. Barthelmy, P. Butterworth, F. Marshall, D. Palmer, R. Aptekar, S. Golenetskii, V. Il'Inskii, D. Frederiks, J. McTier-nan, R. Gold, and J. Trombka. A giant periodic flare from the soft γ -ray repeater SGR1900+14. *Nature*, 397:41–43, January 1999.
- [11] C. Kouveliotou, S. Dieters, T. Strohmayer, J. van Paradijs, G. J. Fishman, C. A. Meegan, K. Hurley, J. Kommers, I. Smith, D. Frail, and T. Murakami. An X-ray pulsar with a superstrong magnetic field in the soft γ -ray repeater SGR1806 - 20. *Nature*, 393:235–237, May 1998.
- [12] Y. E. Nakagawa, T. Sakamoto, G. Sato, N. Gehrels, K. Hurley, and D. M. Palmer. The Swift Discovery of X-Ray Afterglows Accompanying Short Bursts from SGR 1900+14. *ApJ*, 681:L89–L92, July 2008.
- [13] R. Ruderman. Neutron star crustal plate tectonics. II - Evolution of radio pulsar magnetic fields. III - Cracking, glitches, and gamma-ray bursts. *ApJ*, 382:576–593, December 1991.
- [14] D. Page and S. Reddy. Dense Matter in Compact Stars: Theoretical Developments and Observational Constraints. *Annual Review of Nuclear and Particle Science*, 56:327–374, November 2006.
- [15] R. C. Duncan and C. Thompson. Formation of very strongly magnetized neutron stars - Implications for gamma-ray bursts. *ApJ*, 392:L9–L13, June 1992.
- [16] J. Braithwaite and H. C. Spruit. A fossil origin for the magnetic field in A stars and white dwarfs. *Nature*, 431:819–821, October 2004.
- [17] L. Ferrario and D. Wickramasinghe. Modelling of isolated radio pulsars and magnetars on the fossil field hypothesis. *MNRAS*, 367:1323–1328, April 2006.
- [18] A. Heger, S. E. Woosley, and H. C. Spruit. Presupernova Evolution of Differentially Rotating Massive Stars Including Magnetic Fields. *ApJ*, 626:350–363, June 2005.
- [19] B. W. Ritchie, J. S. Clark, I. Negueruela, and N. Langer. A VLT/FLAMES survey for massive binaries in Westerlund 1. II. Dynamical constraints on magnetar progenitor masses from the eclipsing binary W13. *A&A*, 520:A48+, September 2010.
- [20] R. Perna, J. S. Heyl, L. E. Hernquist, A. M. Juett, and D. Chakrabarty. Anomalous X-Ray Pulsars and Soft Gamma-Ray Repeaters: Spectral Fits and the Magnetar Model. *ApJ*, 557:18–23, August 2001.

-
- [21] T. E. Strohmayer and A. L. Watts. Fast X-ray Oscillations during the 1998 Magnetar Flare from SGR 1900+14: Evidence for Neutron Star Vibrations. In *Bulletin of the American Astronomical Society*, volume 37 of *Bulletin of the American Astronomical Society*, pages 1497–+, December 2005.
- [22] R. C. Duncan. Magnetar Models for Soft Gamma Repeaters and Anomalous X-ray Pulsars. In *Bulletin of the American Astronomical Society*, volume 30 of *Bulletin of the American Astronomical Society*, pages 1332–+, December 1998.
- [23] L. Samuelsson and N. Andersson. Neutron star asteroseismology. Axial crust oscillations in the Cowling approximation. *MNRAS*, 374:256–268, January 2007.
- [24] H. Sotani, K. D. Kokkotas, and N. Stergioulas. Torsional oscillations of relativistic stars with dipole magnetic fields. *MNRAS*, 375:261–277, February 2007.
- [25] K. Glampedakis, L. Samuelsson, and N. Andersson. Elastic or magnetic? A toy model for global magnetar oscillations with implications for quasi-periodic oscillations during flares. *MNRAS*, 371:L74–L77, September 2006.
- [26] U. Lee. Core-Crust Interaction of Toroidal Modes of Magnetized Neutron Stars. In R. J. Stancliffe, G. Houdek, R. G. Martin, & C. A. Tout, editor, *Unsolved Problems in Stellar Physics: A Conference in Honor of Douglas Gough*, volume 948 of *American Institute of Physics Conference Series*, pages 263–270, November 2007.
- [27] Y. Levin. QPOs during magnetar flares are not driven by mechanical normal modes of the crust. *MNRAS*, 368:L35–L38, May 2006.
- [28] Y. Levin. On the theory of magnetar QPOs. *MNRAS*, 377:159–167, May 2007.
- [29] H. Sotani, K. D. Kokkotas, and N. Stergioulas. Alfvén quasi-periodic oscillations in magnetars. *MNRAS*, 385:L5–L9, March 2008.
- [30] H. Sotani and K. D. Kokkotas. Alfvén polar oscillations of relativistic stars. *MNRAS*, 395:1163–1172, May 2009.
- [31] S. K. Lander and D. I. Jones. Oscillations and instabilities in neutron stars with poloidal magnetic fields. *ArXiv e-prints*, October 2010.

BIBLIOGRAPHY

- [32] H. Sotani, A. Colaiuda, and K. D. Kokkotas. Constraints on the magnetic field geometry of magnetars. *MNRAS*, 385:2161–2165, April 2008.
- [33] M. van Hoven and Y. Levin. Hydromagnetic waves in a superfluid neutron star with strong vortex pinning. *MNRAS*, 391:283–289, November 2008.
- [34] M. Gabler, P. Cerdá-Durán, J. A. Font, E. Müller, and N. Stergioulas. Magneto-elastic oscillations of relativistic stars. *ArXiv e-prints 1007.0856G*, July 2010.
- [35] M. van Hoven and Y. Levin. Magnetar Oscillations I: strongly coupled dynamics of the crust and the core. *ArXiv e-prints 1006.0348V*, June 2010.
- [36] J. R. Oppenheimer and G. M. Volkoff. On Massive Neutron Cores. *Physical Review*, 55:374–381, February 1939.
- [37] K. Ioka and M. Sasaki. Relativistic Stars with Poloidal and Toroidal Magnetic Fields and Meridional Flow. *ApJ*, 600:296–316, January 2004.
- [38] V. D. Shafranov. Plasma Equilibrium in a Magnetic Field. *Reviews of Plasma Physics*, 2:103–+, 1966.
- [39] H. Grad and H. Rubin. Hydromagnetic Equilibria and Force-Free Fields. *Proceedings of the 2nd UN Conf. on the Peaceful Uses of Atomic Energy*, 31:190, 1958.
- [40] I. Wasserman and S. L. Shapiro. Masses, radii, and magnetic fields of pulsating X-ray sources - Is the 'standard' model self-consistent. *ApJ*, 265:1036–1046, February 1983.
- [41] J. A. Petterson. Magnetic field of a current loop around a Schwarzschild black hole. *Phys. Rev. D*, 10:3166–3170, November 1974.
- [42] R. B. Wiringa, V. Fiks, and A. Fabrocini. Equation of state for dense nucleon matter. *Phys. Rev. C*, 38:1010–1037, August 1988.
- [43] A. Akmal and V. R. Pandharipande. Spin-isospin structure and pion condensation in nucleon matter. *Phys. Rev. C*, 56:2261–2279, October 1997.
- [44] A. Akmal, V. R. Pandharipande, and D. G. Ravenhall. Equation of state of nucleon matter and neutron star structure. *Phys. Rev. C*, 58:1804–1828, September 1998.

-
- [45] M. Baldo, G. F. Burgio, and H. - . Schulze. Strange hadronic stellar matter within the Brueckner-Bethe-Goldstone theory. *ArXiv Nuclear Theory e-prints*, June 2000.
- [46] V. R. Pandharipande, D. Pines, and R. A. Smith. Neutron star structure: theory, observation, and speculation. *ApJ*, 208:550–566, September 1976.
- [47] T. G. Cowling. The non-radial oscillations of polytropic stars. *MNRAS*, 101:367–+, 1941.
- [48] P. N. McDermott, H. M. van Horn, and J. F. Scholl. Nonradial g-mode oscillations of warm neutron stars. *ApJ*, 268:837–848, May 1983.
- [49] H. Robe. Les oscillations non radiales des polytropes. *Annales d’Astrophysique*, 31:475–+, February 1968.
- [50] K. D. Kokkotas and B. F. Schutz. Normal modes of a model radiating system. *General Relativity and Gravitation*, 18:913–921, September 1986.
- [51] K. Kokkotas and B. Schmidt. Quasi-Normal Modes of Stars and Black Holes. *Living Reviews in Relativity*, 2:2–+, September 1999.
- [52] B. L. Schumaker and K. S. Thorne. Torsional oscillations of neutron stars. *MNRAS*, 203:457–489, May 1983.
- [53] A. Colaiuda, V. Ferrari, L. Gualtieri, and J. A. Pons. Relativistic models of magnetars: structure and deformations. *MNRAS*, 385:2080–2096, April 2008.
- [54] D. N. Aguilera, J. A. Pons, and J. A. Miralles. The Impact of Magnetic Field on the Thermal Evolution of Neutron Stars. *ApJ*, 673:L167–L170, February 2008.
- [55] J. Braithwaite and H. C. Spruit. Evolution of the magnetic field in magnetars. *A&A*, 450:1097–1106, May 2006.
- [56] N. Andersson, G. L. Comer, and D. Langlois. Oscillations of general relativistic superfluid neutron stars. *Phys. Rev. D*, 66(10):104002–+, November 2002.
- [57] S. A. Teukolsky. Stability of the iterated Crank-Nicholson method in numerical relativity. *Phys. Rev. D*, 61(8):087501–+, April 2000.
- [58] P. Cerdá-Durán, N. Stergioulas, and J. A. Font. Alfvén QPOs in magnetars in the anelastic approximation. *MNRAS*, 397:1607–1620, August 2009.

BIBLIOGRAPHY

- [59] J. A. Pons, J. A. Miralles, and U. Geppert. Magneto-thermal evolution of neutron stars. *A&A*, 496:207–216, March 2009.
- [60] V. Suleimanov, V. Hambaryan, A. Y. Potekhin, G. G. Pavlov, M. van Adelsberg, R. Neuhaeuser, and K. Werner. Absorption Features in Spectra of Magnetized Neutron Stars. *ArXiv e-prints 1010.0125*, October 2010.
- [61] N. Chamel and P. Haensel. Physics of Neutron Star Crusts. *Living Reviews in Relativity*, 11:10–+, December 2008.
- [62] C. J. Horowitz and D. K. Berry. Shear viscosity and thermal conductivity of nuclear “pasta”. *Phys. Rev. C*, 78(3):035806–+, September 2008.
- [63] A. K. Harding and D. Lai. Physics of strongly magnetized neutron stars. *Reports on Progress in Physics*, 69:2631–2708, September 2006.
- [64] P. Goldreich and A. Reisenegger. Magnetic field decay in isolated neutron stars. *ApJ*, 395:250–258, August 1992.
- [65] J. A. Pons and U. Geppert. Magnetic field dissipation in neutron star crusts: from magnetars to isolated neutron stars. *A&A*, 470:303–315, July 2007.
- [66] C. J. Horowitz and K. Kadau. Breaking Strain of Neutron Star Crust and Gravitational Waves. *Physical Review Letters*, 102(19):191102–+, May 2009.
- [67] J. W. Negele and D. Vautherin. Neutron star matter at sub-nuclear densities. *Nuclear Physics A*, 207:298–320, June 1973.
- [68] E. Gaertig and K. D. Kokkotas. Relativistic g-modes in rapidly rotating neutron stars. *Phys. Rev. D*, 80(6):064026–+, September 2009.
- [69] P. N. McDermott, H. M. van Horn, and C. J. Hansen. Nonradial oscillations of neutron stars. *ApJ*, 325:725–748, February 1988.
- [70] A. L. Watts and T. E. Strohmayer. Detection with RHESSI of High-Frequency X-Ray Oscillations in the Tail of the 2004 Hyperflare from SGR 1806-20. *ApJ*, 637:L117–L120, February 2006.
- [71] V. Hambaran, R. Neuhaeuser, and K. D. Kokkotas. . *Preprint*, 2010.
- [72] A. Colaiuda, H. Beyer, and K. D. Kokkotas. On the quasi-periodic oscillations in magnetars. *MNRAS*, 396:1441–1448, July 2009.

Deutsche Zusammenfassung

Der Untersuchung stark magnetisierter Neutronensterne wurde in den letzten zehn Jahren, nicht zuletzt durch Satellitenbeobachtungen, große Aufmerksamkeit zuteil. Für gewöhnlich unterscheidet man bei diesen kompakten Objekten zwischen sogenannten AXPs (Anomalous X-ray Pulsars) und SGRs (Soft Gamma Repeater). Die Winkelgeschwindigkeit von AXPs ist in einem engen Bereich konzentriert ($P \simeq 5 - 12$ secs); außerdem sind sie starke Röntgenstrahlungsquellen ($L \simeq 10^{36} - 10^{44}$ erg/s). SGRs zeigen aperiodisch Ausbrüche von Gamma- und Röntgenstrahlung die im Maximum Werte von $L \simeq 10^{46}$ erg/s erreichen kann. Diese große Leuchtkraft wird durch eine entsprechende Freisetzung von Energie erzeugt, die ihren Ursprung jedoch nicht in der Umwandlung von Rotationsenergie haben kann. Im Gegensatz dazu kann ein genügend starkes Magnetfeld ($B > 10^{14}$ Gauss) sehr wohl als Energiereservoir für diese Ereignisse dienen. Es ist in der Tat so, daß ein derartiges Magnetfeld einen immensen Druck auf die Neutronensternkruste ausüben kann und diese zu guter Letzt brechen kann. Dieses Brechen der Kruste, gefolgt von einer Neuordnung des Magnetfeldes kann die gewaltigen Energiemengen liefern, die in SGRs beobachtet werden. Zusätzlich liefert dieser Mechanismus auch eine Erklärung für die Variationen der Leuchtkraft von SGRs einige Sekunden nach dem Ausbruch. Eine sorgfältige Analyse des Signals zeigt quasi-periodische Oszillationen (QPOs) mit Frequenzen von einigen Hz bis in den kHz-Bereich. Wir haben dazu ein Erklärungsmodell vorgeschlagen, das die QPOs mit Torsionsschwingungen von sogenannten Alfvén-Moden, Schwingungen des Magnetfeldes, erklärt.

In dieser Doktorarbeit konstruieren wir Gleichgewichtsmodelle nichtrotierender, stark magnetisierter relativistischer Neutronensterne mit flüssigem Kern und dünner äußerer Kruste. Wir leiten in linearer Näherung die Störungsgleichungen für diese Magnetar-Modelle her und implementieren diese anschliessend in einem Computerprogramm. Damit untersuchen wir schließlich die möglichen Schwingungsformen für verschiedene Magnetfeldkonfigurationen und -stärken. Wir vergleichen auch die numerisch gefundenen Frequenzen mit aktuellen Beobachtungen in SGRs und zeigen, dass ein bestimmtes Magnetar-Modell, also die Wahl einer Zustandsgleichung für das flüssige Innere und der festen Kruste zusammen mit einer Magnetfeldkonfiguration, alle beobachteten Frequenzen erklären kann. Dadurch sind wir in der Lage, wichtige Kenngrößen der Magnetare, also etwa Masse, Radius und Magnetfeldstärke, einzugrenzen.

Curriculum Vitae

Persönliche Angaben

Name Antonella Colaiuda
Familienstand ledig
Staatsangehörigkeit italienisch
Geburtsdatum 28.01.1983
Geburtsort Rom, Italien

Schulbildung

1988 - 1993 Städtische Gemeinschaftsgrundschule 'Marco Polo' Rom
1993 - 1996 Städtische Mittelschule 'Giovanni Toniolo' Rom
1996 - 2001 Städtisches Gymnasium 'Liceo Classico Benedetto da Norcia' Rom
Abitur Juli 2001, Note: 100/100

Wissenschaftlicher Werdegang

2001 - 2004 Studium der Physik an der 'La Sapienza' Universität Rom , Diplom
Oktober 2004, Note 110/110 cum laude
2004 - 2006 Master an der 'La Sapienza' Universität Rom, Diplom Oktober 2007,
Note 110/110 cum laude
2007 - 2010 Anfertigung der vorliegenden Dissertation *Magnetised neutron stars* am
Institut für Astronomie und Astrophysik der Universität Tübingen unter
Anleitung von Prof. Dr. K. Kokkotas

Veröffentlichungen

A. Colaiuda, V. Ferrari, L. Gualtieri, J. Pons
Relativistic models of magnetars: structure and deformations,
MNRAS Vol. 385,2080 2008

H. Sotani, A. Colaiuda & K. Kokkotas
Constraints on the magnetic field geometry in magnetars,
MNRAS Vol. 385,2161 2008

A. Colaiuda, H. Beyer & K. Kokkotas
On the quasi-periodic oscillations in magnetars,
MNRAS Vol. 396,1441 2009

A. Colaiuda & K. Kokkotas
Magnetars oscillations in the presence of a crust,
Accepted for publication in MNRAS

Akademische Lehrer

G. Bachlet, A. Capone, R. Capuzzo Dolcetta, P. De Bernardis, D. Fargion, V. Ferrari, P. Giannone, M. Lusignoli, G. Martinelli, E. Massaro, F. Melchiorri, M. Merafina, G. Moreno, F. Ricci, D. Trevese.